MULTIAXIAL COMPRESSIVE STRESS STATES WITHIN A CONCRETE ONSHORE WIND TURBINE FOUNDATION

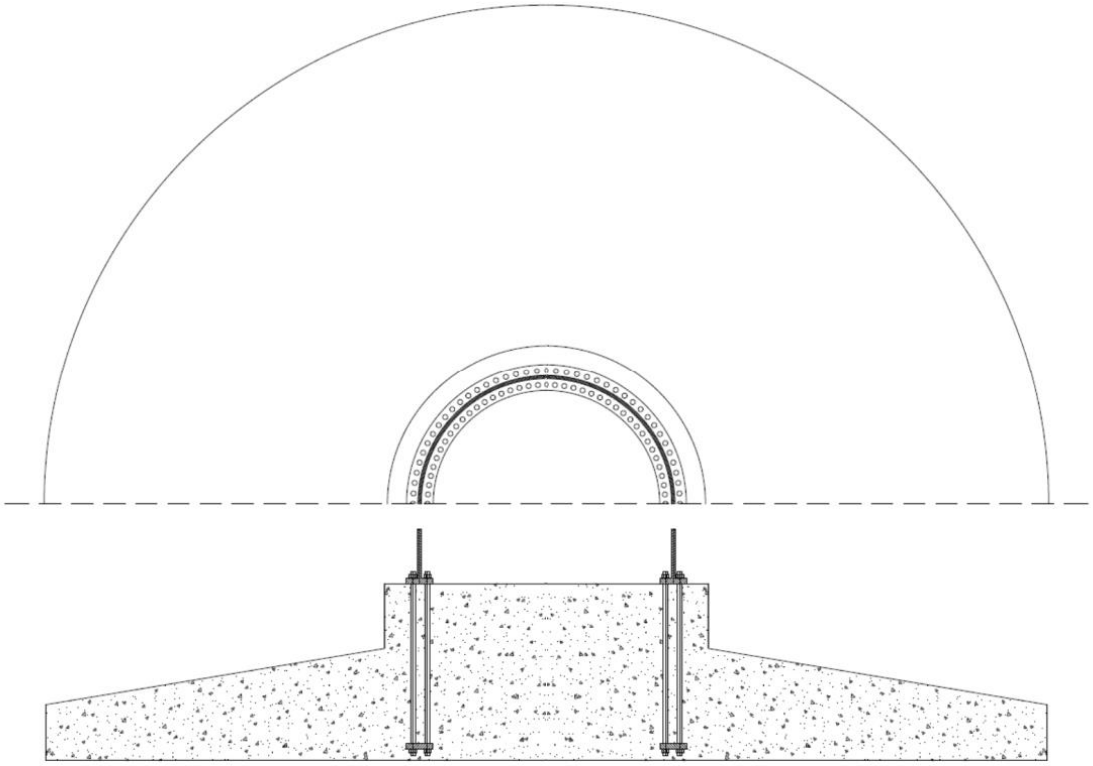

A three dimensional non-linear finite element analysis of the concrete surrounding the anchor cage

Jelle de Groot
Delft University of Technology

November 2022

Thesis committee:	Prof.dr.ir. M.A.N Hendriks	TU Delft, chair
	Dr.ir. E.O.L. Lantsoght	TU Delft
	Ir. P.A. Korswagen	TU Delft
	Ir. E. Brok	ABT, supervisor

SUMMARY / ABSTRACT

With the rising demand for renewable energy sources the amount of wind turbines which are built on land are growing rapidly. Because of the repetitive nature of the foundation small design improvements can add up to large savings in material usage and building cost. The most critical part of the foundation is the connection between the metal mast and the concrete foundation. This connection is made by implementing an anchor cage. The application of an anchor cage results in complex multiaxial stresses in the surrounding area. Confinement plays a large role in the compressive strength of the concrete subjected to the partially loaded area created by the anchor flange. The main goal of this thesis is investigating the best way of modelling the concrete surrounding the anchor cage at confinement levels being present in the wind turbine foundation.

This is done by investigating the theory regarding confinement and the effects of it. But also the way this is captured by analytical models. To make a comparison between DIANA and the analytical models the present stress situation in the wind turbine foundation is analysed. Looking at the stress distribution and the confinement levels. Next a comparison of the ideal case of confinement is made. This is later expanded to a larger scale model, to compare the effects of confinement.
The confinement present will enhance the concrete strength and strain properties. The concrete specimen can resist larger loads and reacts more ductile. These properties are captured in analytical confinement models, these are compared to the way DIANA approaches confinement.
The anchor rods between the anchor flanges are prestressed, this prestressing results in a permanent stress situation. Within this stress situation there is a small part beneath the anchor flange subjected to confinement. With increasing pressure, originating from the moment load which results from the wind on the tower and it's blades, the confined area increases to the top half of the foundation. With significant confinement in the pedestal.
Comparing the DIANA compressive behaviour models with the analytical confinement models and experimental data within a one element model. It is seen that compressive behaviour models do react on the confinement. Although they show a lower peak strength than the analytical models. A larger difference is noted in the underestimation of the peak strain. This difference in outcomes is the result of the different approaches between DIANA and the analytical models. As well as some assumptions that DIANA makes concerning the strength and strain increase factor. The Parabolic compressive curve is most suitable for modelling the confinement in this ideal case.
A case study is conducted to further investigate how the confinement is represented in a total non-linear model. Modelling the top part of the foundation and checking the effect that confinement has on this model. For this model the prestressing of the anchor rods is increased until failure. Without confinement the concrete elements directly beneath the anchor flange fail in compression. Running the model with confinement it is noticed that the underlying weaker concrete is failing in compression first. This is the result of the confinement being present surrounding the anchor flange. The model with confinement is also able to resist a 30% larger load than the model without confinement.
The parabolic compression curve is the most suitable curve currently available inside the strain based crack model for modelling the effects of confinement. Overall DIANA is able to capture the effects of confinement well enough to see the positive effects in the case study. Due to limitations in the analyses performed and in their interpretations, it is not possible to give an unequivocal answer on the effect of confinement within the foundation of the wind turbine.

CONTENTS

1 INTRODUCTION 1
1.1 BACKGROUND 1
1.2 ONSHORE WIND TURBINE FOUNDATION 1
1.2.1 The foundation slab 1
1.2.2 The anchor cage 2
1.2.3 Forces surrounding the anchor cage 3
1.3 OBJECTIVE 3
1.4 SCOPE 3
1.5 RESEARCH QUESTION 4
1.6 OUTLINE 4
2 LITERATURE REVIEW 5
2.1 WHAT IS CONFINEMENT 5
2.2 MULTIAXIAL COMPRESSIVE STRESS STATES 5
2.2.1 Multiaxial compressive stresses test setup 5
2.2.2 Influence on strength 6
2.2.3 Stress-displacement curves 8
2.3 ORIGIN OF CONFINEMENT 9
2.3.1 Active confinement 9
2.3.2 Passive confinement 9
2.3.3 Confinement in the wind turbine foundation 9
2.4 ANALYTICAL CONFINEMENT MODELS 9
2.4.1 Peak conditions 10
2.4.2 Curve description 10
2.5 CONCRETE UNDER CONCENTRATED LOADS 13
2.6 DIANA FEA APPROACH TO CONFINEMENT 14
2.6.1 DIANA's compressive models 14
2.6.2 Hsieh-Ting-Chen four-parameter failure surface 17
3 LINEAR ELASTIC STRESS SITUATION 18
3.1 DIMENSIONS, PROPERTIES AND LOADS SURROUNDING THE ANCHOR CAGE 18
3.1.1 Dimensions and properties of the concrete body 18
3.1.2 Dimensions of the anchor cage 19
3.1.3 Loads on the anchor cage 21
3.2 STRESSES DIRECTLY BELOW TOP ANCHOR FLANGE 22
3.3 STRESS DEVELOPMENT IN THE CONCRETE 23
3.3.1 Axisymmetric model description 23
3.3.2 DIANA 3D model description 23
3.3.3 Pre-tensioning stresses 24
3.3.4 Overturning moment 25
3.3.5 Combined action prestressing and overturning moment 26
3.3.6 Overall occurring confinement 26
3.3.7 Significance of confinement 27
4 COMPARISON OF IDEAL CONFINEMENT CASE 28
4.1 COMPARING DIANA COMPRESSIVE CURVES, ANALYTICAL MODELS AND EXPERIMENTAL VALUES 28
4.1.1 Analytical models 28
4.1.2 DIANA compressive curves 29
4.1.3 Experimental values 30
4.1.4 Results 31
4.1.5 Comments and remarks 36

4.1.6 Concluding *37*
5 CONFINEMENT WITHIN THE CASE STUDY **38**
5.1 AXISYMMETRIC TOP MODEL 38
5.2 COMPARING TOP MODEL WITH TOTAL AXISYMMETRIC MODEL 40
5.3 EFFECT OF CONFINEMENT ON THE TOP MODEL 42
5.4 CONFINEMENT WITHIN THE TOP MODEL 45
6 CONCLUSION **46**
6.1 CONCLUSION 46
6.2 RECOMMENDATIONS FOR FUTURE WORK 47
7 REFERENCES **48**
8 APPENDICES **50**
1. ASSUMPTION BEDDING CONSTANT, KC **51**
2. SCIA ENGINEERING RAPPORT **52**
3. DATABASE ACTIVELY CONFINED CONCRETE **53**

LIST OF TABLES

TABLE 2-1: ANALYTICAL MODELS PEAK STRESS AND PEAK STRAIN 10
TABLE 3-1: CONCRETE STRENGTH 19
TABLE 3-2: LOADS ON THE FOUNDATION 21
TABLE 3-3: SCIA RESULTS 22
TABLE 4-1: PARAMETERS FOR DIANA MODEL USED FOR COMPRESSIVE BEHAVIOUR COMPARISON 29
TABLE 4-2: EXPERIMENTAL VALUES 31
TABLE 5-1: NON-LINEAR ANALYSIS PARAMETER FOR THE TOP MODEL 39

List of Figures

Figure 1-1: Cross section foundation slab 2
Figure 1-2a: Placement anchor cage; b: Impression anchor cage 2
Figure 1-3: Stress state between anchor flanges 3
Figure 1-4: Flowchart thesis layout 4
Figure 2-1: Plane stress (biaxial) strength envelope (Van Geel 1998) 6
Figure 2-2: Cross section of triaxial strength envelope in τ0-σ0 plane (Podgorski 1985) 7
Figure 2-3: Stress-displacement curves in triaxial compression tests (Van Geel 1998) 8
Figure 2-4: Axial displacement verses mean 'volumetric displacement' in triaxial tests on normal strength concrete (Van Geel 1998) 8
Figure 2-5: Confined compressive curve (modified from Lim and Ozbakkaloglu 2014) 10
Figure 2-6: Flow of stresses in concrete member under localized force: a Stress trajectories; b: Stress distribution (Wichers 2013) 13
Figure 2-7: Compressive curves DIANA 14
Figure 2-8: Failure surface (Hsieh et al 1981) 17
Figure 3-1: Top view wind turbine foundation 18
Figure 3-2: Cross section wind turbine foundation 19
Figure 3-3: Anchor cage 19
Figure 3-4: Top flange dimensions 20
Figure 3-5: Anchor rod dimensions 20
Figure 3-6: Bottom flange dimensions 20
Figure 3-7: Forces on foundation 21
Figure 3-8: Description x and Φ 22
Figure 3-9: The axisymmetric model 23
Figure 3-10: The 3D model 23
Figure 3-11: Pre-tensioning stresses in the concrete over the height; Syy, Szz, Sxx from left to right 24
Figure 3-12: Schematic view of the moment load on 3D model 25
Figure 3-13: Moment stresses in the concrete over the height; Syy, Szz, Sxx from left to right 25
Figure 3-14: Stresses resulting from moment and prestressing in the concrete over the height; Syy, Szz, Sxx from left to right 26
Figure 3-15: Unity check over height of the foundation 27
Figure 4-1: DIANA model 29
Figure 4-2: Strength enhancement ratio from experimental database 30
Figure 4-3: Strain enhancement ratio from experimental database 30
Figure 4-4: Comparison at 0.0 confinement; top, Total curves; middle, Top of the curves; bottom, Peak of the curves 32
Figure 4-5: Comparison at 1.0 confinement; top, Total curves; middle, Top of the curves: bottom, Peak of the curves 33
Figure 4-6: Comparison at 5.0 confinement; top, Total curves; middle, Top of the curves: bottom, Peak of the curves 34
Figure 4-7: Comparison at 10.0 confinement; top, Total curves; middle, Top of the curves: bottom, Peak of the curves 35
Figure 4-8: Compare of compressive behaviour models with different levels of confinement 36
Figure 5-1: Location and dimensions of axisymmetric top model 38
Figure 5-2: Axisymmetric top model 39
Figure 5-3: Comparison principal stresses of linear axisymmetric model, linear 3D model and the axisymmetric top model 40
Figure 5-4: Comparison principal stress (S1), Left total axisymmetric model, Right axisymmetric top model 40
Figure 5-5: Comparison principal stress (S2), Left total axisymmetric model, Right axisymmetric top model 41

FIGURE 5-6: COMPARISON PRINCIPAL STRESS (S3), LEFT TOTAL AXISYMMETRIC MODEL, RIGHT AXISYMMETRIC TOP MODEL 41
FIGURE 5-7: TOP MODEL WITHOUT CONFINEMENT, LOAD STEP 28 42
FIGURE 5-8: TOP MODEL WITH CONFINEMENT, LOAD STEP 28 42
FIGURE 5-9: TOP MODEL WITH CONFINEMENT, LOAD STEP 36 43
FIGURE 5-10: TOP MODEL PRINCIPAL STRESS S1 43
FIGURE 5-11: TOP MODEL CRACK FORMATION 43
FIGURE 5-12: INDICATION OF ELEMENT FOR EXTRACTING LOAD DISPLACEMENT DIAGRAM 44
FIGURE 5-13: LOAD DISPLACEMENT GRAPH OF TOP MODEL 44

1 INTRODUCTION

1.1 Background

Over the last decades the awareness for global warming has increased. Also the last IPCC report has left a critical side note by numerous governments. The continuous rise CO2 levels are an universal problem. The CO2 released by means of energy generation has to be reduced. An alternative for burning fossil fuels is the application of renewable energy. The utilisation of wind energy is expanding. As the demand for renewable energy is ever more growing, so are the wind turbines at sea and on land. The rotor blades are getting bigger and more efficient, which leads to larger tower structures. With the larger structures the forces acting on the tower and the blades are also scaling up. Because of the increased applications of onshore wind turbines, it occurs more often that the soil properties are less favourable. The larger forces and less favourable conditions are the cause of the increasing dimensions of the foundation. By the increased implementation and the repetitive nature of these growing foundations, large savings can be achieved by improving the design.

1.2 Onshore wind turbine foundation

The onshore wind turbine foundation consists of three main parts. The concrete body, the anchor cage and the reinforcements. The concrete body and the reinforcements work together distributing the loads to the supporting soil and or piles. The anchor cage serves as the connection between the foundation and the tower of the wind turbine.

1.2.1 The foundation slab

The three bladed horizontal axis wind turbine design is one of the most common used for onshore wind turbines. At the bottom of the tower there is a large concrete slab to cope with the large particularly bending moment originating from the wind. This concrete slab is the foundation of the wind turbine and ensures the connection with the ground. Depending on the soil conditions there are in general three types of slab foundations: a gravity foundation, a piled foundation and a rock anchored foundation. The working of a gravity slab is already in the name, the slab is designed in a way that the gravity is working against the large overturning moment. A piled foundation slab is held in place by one or two circles of piles. This foundation type is used where the soil properties are not sufficient to bare the loads. A rock anchored foundation is only applicable on places where hard bed rock is available. In the Netherlands this bed rock is almost non-existing and the soil properties are generally

poor, so the piled foundation is mainly applied. The selection of the foundation slab design is highly dependent on the soil conditions, but also on the size of the tower and the blades. With a larger tower, the blades will reach higher altitudes. The wind at higher altitudes is less obstructed and generally stronger. If the blades become longer, the area over which the wind is captured grows exponentially. So the larger the tower and the blades become, the higher the efficiency of the wind turbine. But with the increasing dimensions of the wind turbines the forces are also getting larger, resulting in the need for bigger foundation slabs. Most of the foundation slabs are circular in form, this is because of the changing wind directions. The foundation has to be evenly strong in every direction, working against the overturing moment. An additional factor is that the formwork does not need to be heavily supported. It holds itself upright because of the circular form which will result in tension forces in the formwork.

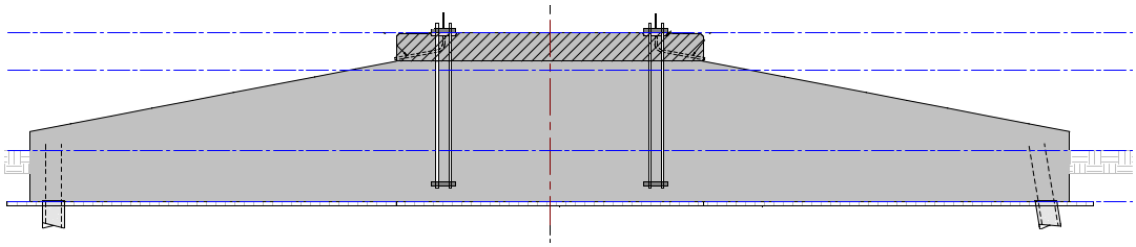

Figure 1-1: Cross section foundation slab

The foundation slab has a large circular shape resting on piles or the soil beneath it. A cross section is displayed in Figure 1-1. In most cases the foundation is composed of two parts: the main body and the pedestal. The main body is often tapered to the middle of the foundation and the pedestal is poured on top. Between the anchor flanges and the pedestal a small grout layer is applied to ensure a seamless fit for the force introduction.

1.2.2 The anchor cage

The forces acting on the tower need to be transferred to the foundation slab. For this connection generally two designs are applied: a steel insert ring or an anchor cage. Figure 1-2a is displaying the placement of the anchor cage. The steel insert ring is embedded in the foundation slab and the tower is connected to the solid steel ring by an elevated flange. With the anchor cage design the bottom flange of the cage and the rods are embedded in the foundation, the top flange is left sticking out. The bottom tower flange is connected to the anchor rods. These rods are getting prestressed ensuring the connection between the tower and the foundation slab. The bolts are pulling the bottom flange and the top flange together, prestressing the concrete in between. This ensures a robust system which distributes the forces over the area of the flanges. The anchor cage design is contemporary more used over the steel insert ring design. The anchor cage is displayed in Figure 1-2b.

Figure 1-2a: Placement anchor cage; b: Impression anchor cage

1.2.3 Forces surrounding the anchor cage

Looking at a concrete cube directly below the top anchor flange, this cube will have three orthogonal axes. This imaginary cube is displayed in Figure 1-3. If the axis directions are taken as the principal directions, the stresses will develop in the three main directions. In the y-direction the cube is compressed by the prestressing force. In the x-direction the cube is compressed by the partially loaded area, as well as the surrounding concrete. The third direction, the tangential direction, is referred to as the z-direction. This direction is compressed by the surrounding concrete. The concrete pushes on itself in circumferential direction. The compression from al the different directions creates a multiaxial compressed stress state.
The overturning moment will push on one side of the anchor flange and pull on the other side. This will increase the compression in y-direction at the top side on one end. At the other end the tension force on the top flange will be transported by the anchor rods to the bottom flange. The concrete cube directly above the bottom flange will be in the same compressive stress state.

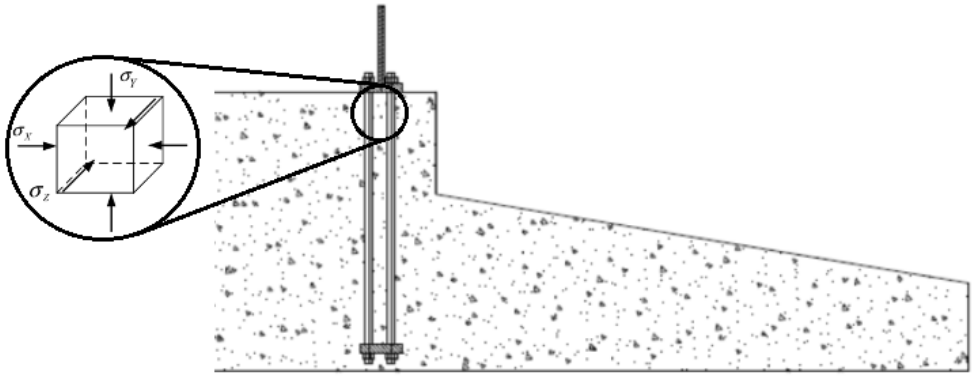

Figure 1-3: Stress state between anchor flanges

1.3 Objective

The main goal of this thesis will be investigating the best suited compressive curve inside the strain based crack model for modelling the confined concrete surrounding the anchor cage. Comparing it with analytical confinement models and experimental peak values. This will be accomplished by taking the occurring compressive stresses surrounding the anchor cage and finding the best modelling strategy within DIANA, comparing the different compressive behaviour models with analytical models and experimental results. Thereafter the confinement within a non-linear case study is analysed.

1.4 Scope

The focus of the project will be directed to concrete onshore wind turbine foundations, in particular to the centre of the foundation. In the centre the force introduction will take place from the tower into the foundation slab by means of the anchor cage. The anchor cage will be situated in the middle of the foundation slab. The emphasis will lay on the concrete surrounding the anchor cage flanges, in particular the concrete in multiaxial compression. Looking at the concrete confined by the loads and the shape of the foundation. DIANA will be the finite element program that is used to make the analysis and within the non linear analysis the total strain based crack model is used. Only the already programmed options in the program are investigated. Making use of the compressive models which can be run with basic available data of the concrete, without the need for special tests to determine specific properties of the concrete mixture. The main focus will be the ultimate limit state design of concrete surrounding the anchor cage in the foundation.

1.5 Research question

The research question is defined as:
What is the best method for modelling confined concrete around the anchor cage in a non-linear 3D finite element method calculation so that it accurately represents real structural and material behaviour?

The research question is divided in the following sub questions:
What is confinement and how does it affect the concrete properties?
Which stress states occur around the anchor cage?
How can the occurring compressive stresses best be modelled within the strain based rotating crack model within DIANA?
What role does confinement play in a model representing the area around the anchor cage?

1.6 Outline

The outline of this thesis is displayed by the flowchart in Figure 1-4.

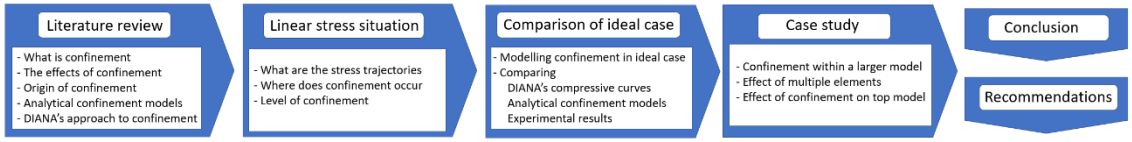

Figure 1-4: Flowchart thesis layout

In chapter one the general subject is introduced and the research question is stated. Next in chapter two the literature review is presented. The literature review focusses on: what is confinement, where does it occur, the effects of confinement, the origin of confinement, concrete under concentrated loads and the approach that DIANA has to confinement. If the effects that confinement has on concrete are explored the linear stress situation inside the wind turbine foundation are investigated in chapter three. These stress levels give valuable information on the magnitude and location on where how much confinement is present in the wind turbine foundation. Subsequently in chapter four the ideal case of confinement is investigated. Comparing different compressive behaviour models with analytical models and experimental values. From this a general modelling strategy is derived for modelling the confinement ranges resulting from the linear stress analysis. After that in chapter five the effect of confinement on a case study with a non-linear analysis is conducted. This is done to investigate how the confinement react in a total model in which the stresses are not always ideally orientated and composed of multiple elements. Then in chapter six all the findings are concluded and the research question is answered.

2 LITERATURE REVIEW

The multiaxial compressive stress states surrounding the anchor cage will be of great interest, this is due to the of the effects of biaxial and triaxial compression. There are some differences between the types of confinement. Over time researchers have presented multiple analytical models describing the stress-strain curve of confined concrete. Partially loading of the concrete by the limited area of the anchor flange have effect on the multiaxial stress development in the concrete. After this the way confinement is approached by DIANA finite element analysis, within the total strain crack model is discussed.

2.1 What is confinement

Confinement is a term that is used to indicate a multiaxial compressive stress state. If all the principal stresses are compressive of nature there will be confinement. This is derived from a confined area, so no expansion is possible. The effects that confinement has on concrete are described following paragraph.

2.2 Multiaxial compressive stress states

Uniaxial compression is easy to imagine for most people. When a concrete cube is compressed over one axis you get a uniaxial compressed stress state. By compressing one of the secondary axis a biaxial compressed stress state is acquired. A multiaxial compressive stress state is a stress state that occurs if al three principal stress directions are composed of compressive stresses. In most practical cases the compressive stresses on the secondary axis are called the confining stress and the stress on the primary axis the loading stress. As earlier described this multiaxial compressive stress state are present in the concrete surrounding the anchor flanges. Extensive research on the topic was carried out by Bongers (2008), with its most important predecessors being Newman (1979), Van Mier (1984), Vonk (1992) and Van Geel (1995a, 1995b, 1998).

2.2.1 Multiaxial compressive stresses test setup

Experiments on multiaxial compressive stresses are performed with two different test configurations. The triaxial cell and the true triaxial loading apparatus. For the triaxial cell the test specimen are mainly cylindrical shaped. The specimen is placed into a pressure vessel and fluid pressure is loading the specimen in radial direction. This radial loading results in a confining stress. The axial direction is loaded by a hydraulic jack. A impermeable membrane is used to prevent the hydraulic fluid from entering into the tested specimen. A big limitation of this test setup is that the two confining principal stresses are always equal.

For the true triaxial loading apparatus the test specimen are mainly cubes or prisms. The loading apparatus is build up from three orthogonal loading frames which can be pressed independently from each other, resulting in a diverse loading options. The type of loading platens results to be quite influential in the stress development in the tested specimen. Because the confining effects large forces are needed to crush the concrete specimen, especially for higher strength concrete and higher confinement levels. Large hydraulic jacks are needed to deliver these forces via loading platens to the tested specimen. This results in large and expensive equipment to conduct these type of tests.

2.2.2 Influence on strength

The lateral confinement is of great influence on the compressive strength of concrete in the axial direction. The axial compressive strength increases in the case of lateral compressive stresses and decreases in the case of lateral tensile stresses. These influences are noted for biaxial an triaxial compression.

2.2.2.1 Biaxial strength

In a triaxial cell the biaxial strength can be measured by means of not loading the axial load (Richart et al 1928). The limitation of this technique is that the compressive stresses are always equal. The top load would be zero in this setup. With a modification to the test setup a hollow cylinder was loaded in a triaxial cell. This would only give satisfactory results for thin-walled tubes, because of the nearly zero radial stress. These drawbacks do not occur when the specimen are loaded biaxially between two sets of load bearing platens controlled by hydraulic jacks. This can also be done in a true triaxial loading apparatus using only two of the three axis. These kind of experiments where performed by Iyengar (1965) using rigid bearing plates. Both tests from Bellamy and Iyengar found similar results. Later it was found by Robinson (1967), Kupfer et al (1969,1973), Liu (1972) and Nelissen (1972) that the friction caused by these ridged bearing plates in the concrete steel interface greatly improves the biaxial compressive strength of the specimen. The friction of these loading platens resulted in extra confining of the directly loaded areas.
In Figure 2-1 different biaxial strength data with reduction of platen restraint is shown for tests performed by Technical University in Munich (TUM), Bundensanstalt für Materialprüfungin Berlin (BAM) and University of Colerado (CU).

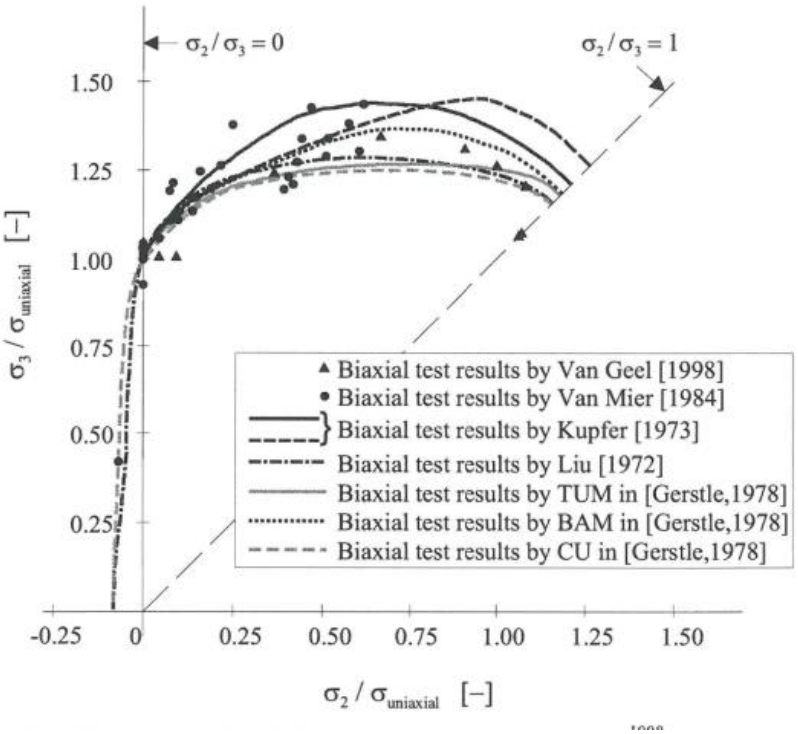

Figure 2-1: Plane stress (biaxial) strength envelope (Van Geel 1998)

It is clearly seen that the compressive stresses rise above one in the graph, meaning that the compressive stress measured lays above the uniaxial compressive strength of the specimen. Indicating that the biaxial compressive strength is higher than the uniaxial compressive strength.

2.2.2.2 Triaxial strength

When the concrete is lateral confined in both directions the strength is influenced even more. This principle of this material behaviour is incorporated in the mohr-coulomb strength criterion. The criterion is based upon the maximum and minimum principal stresses and the internal friction. Because of its appealing physical background and simplicity this criterion is widely accepted and used. The first triaxial cell experiments were conducted by Richart et al (1928). Later tests are conducted by Hobbs (1971) using a triaxial cell and by Mills et al (1970), Launay et al (1970) and Bertacchi et al (1972) using a true triaxial loading apparatus. The boundary conditions and their influence are researched by Gerstle et al (1978).
In Figure 2-2 the results are shown from triaxial tests, herein are the confining stresses equal. The compressive meridian consists of the ultimate stress states with one major compressive principal stress and two equal minor confining stresses. The tensile meridian consists of the ultimate stress states with two equal major confining stresses and one minor compressive stress.

$$\sigma_0 = \frac{1}{3} * (\sigma_1 + \sigma_2 + \sigma_3) \quad (1)$$

$$\tau_0 = \frac{1}{3} * \sqrt{(\sigma_1 - \sigma_2)^2 + (\sigma_2 - \sigma_3)^2 + (\sigma_3 - \sigma_1)^2} \quad (2)$$

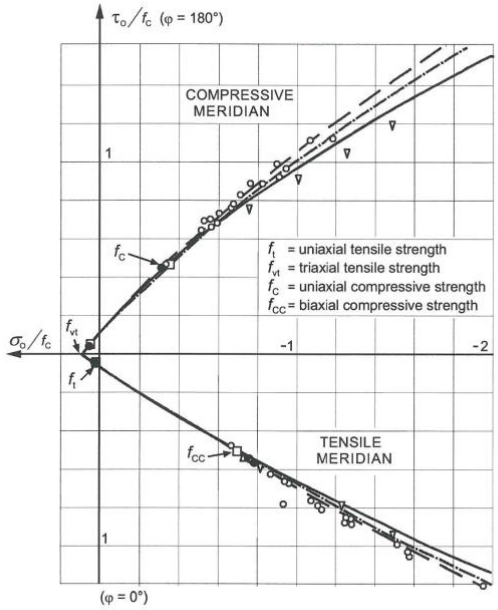

Figure 2-2: Cross section of triaxial strength envelope in τ0-σ0 plane (Podgorski 1985)

The characteristics of the Mohr-Coulomb strength criterion are confirmed by experimental data displayed in Figure 2-2. The triaxial strength envelope is convex, sensitive to lateral confinement and open ended. Meaning the strength will increase with increasing confining stress and that the specimen will not fail if the confining stress stays equal to the compressive stress.

2.2.3 Stress-displacement curves

The results of triaxial tests on normal strength cubes are displayed in Figure 2-3. The lateral confining pressures are equal. Remarkable is the increase in ductility as well as the major increase of strength with increasing confining pressure. The post-peak behaviour changes from highly brittle in uniaxial compression to ductile for high confinement levels. This phenomenon is often called the brittle-ductile transition. This is investigated by multiple researchers (Jamet 1984, Smith et al 1989, Sfer et al 2002).

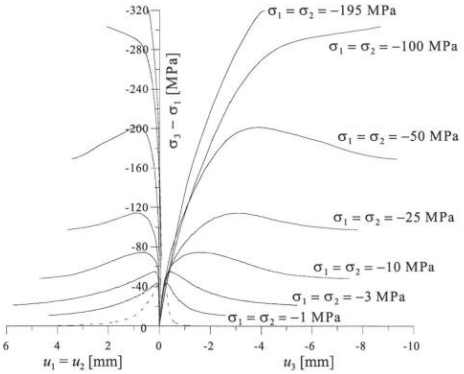

Figure 2-3: Stress-displacement curves in triaxial compression tests (Van Geel 1998)

Looking at Figure 2-4 it displays the development of volumetric strain of concrete loaded in triaxial compression. Three notable points are pointed out by Kotsovos & Newman (1977). The first point is indicating a change in the rate of volumetric strain towards more contraction. This point exhibits clear non-linear material behaviour.
The second point is indicating a change in the rate of volumetric strain towards more dilation. These two points can only be determined by looking closely to the deformational behaviour and indicate the starting of micro cracks inside the specimen.
The third point is around peak stress in Figure 2-3 and is denoted by the minimum overall volume. After this the cracks will propagate through the specimen and link up. These points show remarkable changes in the fracture process of the specimen (Kotsovos & Newan 1977, Imran & Pantazopoulou 1996).
After conducting rotation experiments in which the most compressive principal stress was rotated, van Mier (1984, 1986) proved that the strength after rotation was dependent on the loading history in some cases. It was found to be mainly depending on the macrocracks formed in the post-peak stage before rotation, so only the linked cracks would have effect of the strength of the specimen.

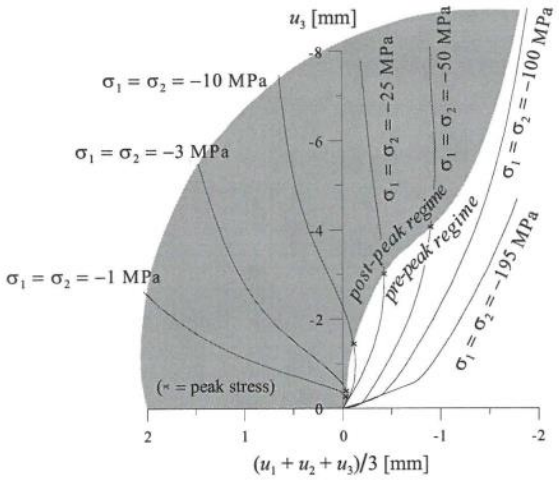

Figure 2-4: Axial displacement verses mean 'volumetric displacement' in triaxial tests on normal strength concrete (Van Geel 1998)

2.3 Origin of confinement

Multiaxial compressive stress state leads to confinement of the concrete, which enhances the properties of the concrete specimen. This is described in the previous paragraphs. A distinction has to be made between actively confined and passively confined concrete. This distinction results from the origin of the confinement.

2.3.1 Active confinement

Actively confined concrete is as the name says actively pressed together, for instance by meaning of prestressing the concrete. There are some differences in the activation of the confinement between active and passive concrete. Active confinement is present from the start of loading and is often constant during the expansion of the concrete. Numerous experiments concerning multiaxial compression have been carried out by different researchers using a triaxial cell or a true loading apparatus, making use of active confinement.

2.3.2 Passive confinement

Passive confinement in the concrete is induced by the resistance delivered by an external influence when the concrete wants to expand. This can for instance be induced by spiral or tie reinforcements, applying an outer shell or the geometrical shape. When the concrete is compressed on the main axis it wants to expand sideways on the secondary axes because of the Poisson ratio, this expansion is prevented leading to confinement. Passive confinement models tend to react more ductile, building up the confinement with larger getting dilations. Passive confinement is mainly investigated by testing concrete columns with various reinforcement and strengthening types. The way these experiments investigating passive confinement are performed makes the outcomes heavily depended on the parameters used, causing a problem in comparing the results.

2.3.3 Confinement in the wind turbine foundation

The confinement that is present in the wind turbine foundation will be qualified as passive confinement by the definition. But the confinement does develop immediately when the load is applied resembling active confinement. Because of the similarities in strain rates between the compressed material and confining material, the confinement resembles more active than passive characteristics. In contrast to a concrete column confined with fibre reinforced polymer wrapping. In this case a minimum deformation is needed to develop confinement. The comparison between the DIANA models and analytical models is made at a set level of confinement and not with the development path of the confinement. It is because of these characteristics and the comparison at a set level of confinement that there is compared with active confinement analytical models.

2.4 Analytical confinement models

Multiple analytical models have been proposed to describe the stress-strain relation of the confined concrete. The basis of the theory was laid down by Richard et al (1928) and the first analytical formula was described by Mander et al (1988). Later some researchers have proposed slight adjustments to this formulas and some researchers have proposed their own analytical formulas. The effectiveness of these formulas are compared with test results acquired by the researchers. A comparison of the existing analytical models conducted by Mansouri et al (2016) and Shahbeyk et al (2017) showed that the models proposed by Attard and Setunge (1996), Jiang and Teng (2007), Xiao et al (2010) and Lim and Ozbakkaloglu (2014) showed the most similarities with the test results. The most important parameters were the peak stress and corresponding peak strain.

2.4.1 Peak conditions

The analytical models fit a curve through some distinctive points. The most important point in the curve is described at the top by the peak stress and the peak strain. A description of the different approaches to the peak stress and the peak strain in the confinement models are displayed in Table 2-1.

Table 2-1: Analytical models peak stress and peak strain

Researcher	Peak stress (f_{cc})	Peak strain (ε_{cc})
Attard and Setunge	$f_{c0} * \left[\left(\frac{f_l}{f_t}+1\right)^{1.25\left(1+0.062\frac{f_l}{f_{c0}}\right)f_{c0}{}^{-0.21}}\right]$	$\varepsilon_{c0}\left[1+\frac{f_l}{f_{c0}}(17-0.06f_{c0})\right]$
Jiang and Teng	$f_{c0}\left[1+3.5\left(\frac{f_l}{f_{c0}}\right)\right]$	$\varepsilon_{c0}\left[1+17.5\left(\frac{f_l}{f_{c0}}\right)^2\right]$
Xiao et al	$f_{c0}\left[1+3.24\left(\frac{f_l}{f_{c0}}\right)^{0.80}\right]$	$\varepsilon_{c0}\left[1+17.4\left(\frac{f_l}{f_{c0}}\right)^{1.06}\right]$
Lim and Ozbakkaloglu	$f_{c0}+5.2f_{c0}^{0.91}\left(\frac{f_l}{f_{c0}}\right)^{f_{c0}^{-0.06}}$	$\varepsilon_{c0}+0.045\left(\frac{f_l}{f_{c0}}\right)^{1.15}$

2.4.2 Curve description

The different analytical compressive curves described by the researchers are represented by the curve displayed in Figure 2-5. Points of general interest are the peak conditions of the confined and unconfined curve, the inflection point of the descending curve and the residual stress of the confined curve.

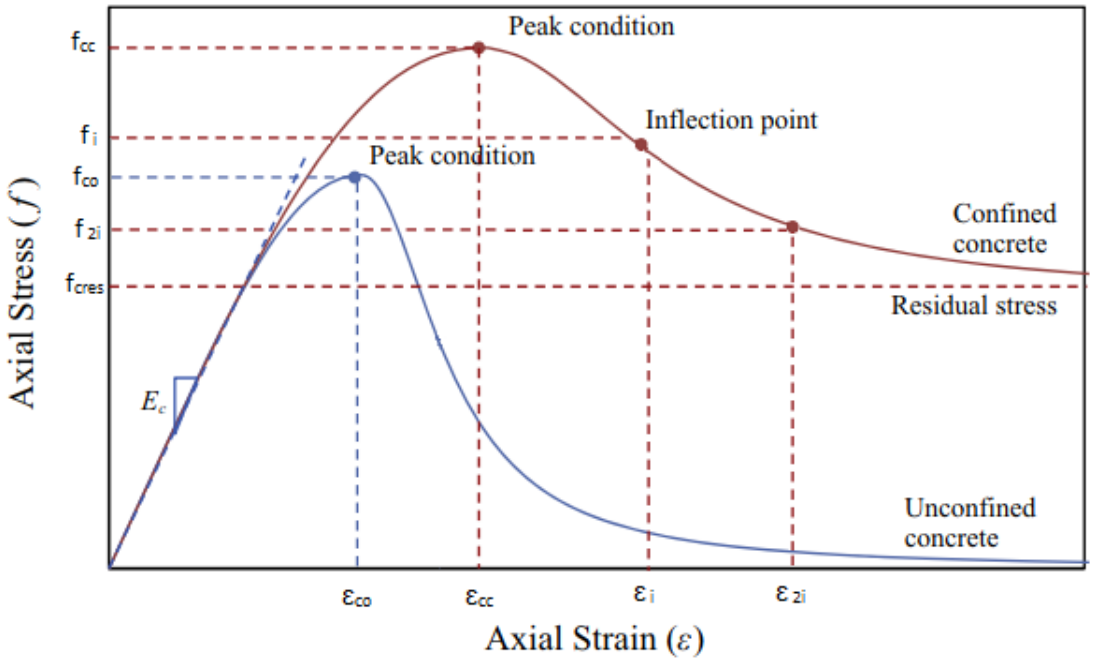

Figure 2-5: Confined compressive curve (modified from Lim and Ozbakkaloglu 2014)

2.4.2.1 Attard and Setunge

The curve is described by equation 3.

$$f_c = \frac{Ax+Bx^2}{1+Cx+Dx^2} * f_{c0} \quad (3)$$

For the ascending curve with ($0<\varepsilon<\varepsilon_{cc}$):

$$x = \frac{\varepsilon_c}{\varepsilon_{c0}} \quad (4)$$

$$A = \frac{E_c * \varepsilon_{cc}}{f_{cc}},\ B = \frac{(A-1)^2}{0.55} - 1,\ C = (A-2),\ D = (B+1) \quad (5)$$

And for the descending curve ($\varepsilon>\varepsilon_{cc}$):

$$f_i = f_{cc}\left[\frac{0.41-0.17\ln(f_{c0})}{5.06\left(\frac{f_l}{f_{c0}}\right)^{0.57}+1}+1\right],\ \varepsilon_i = \varepsilon_{cc}\left[\frac{0.5-0.3\ln(f_{c0})}{1.12\left(\frac{f_l}{f_{c0}}\right)^{0.26}+1}+2\right],\ E_i = \frac{f_i}{\varepsilon_i} \quad (6)$$

$$f_{2i} = f_{cc}\left[\frac{0.45-0.25\ln(f_{c0})}{6.35\left(\frac{f_l}{f_{c0}}\right)^{0.62}+1}+1\right],\ \varepsilon_{2i} = 2\varepsilon_i - \varepsilon_{cc},\ E_{2i} = \frac{f_{2i}}{\varepsilon_{2i}} \quad (7)$$

$$A = \left[\frac{\varepsilon_{2i}-\varepsilon_i}{\varepsilon_{cc}}\right]\left[\frac{\varepsilon_{2i}*E_i}{(f_{cc}-f_i)} - \frac{4*\varepsilon_i*E_{2i}}{(f_{cc}-f_{2i})}\right],\ C = A-2 \quad (8)$$

$$B = (\varepsilon_i - \varepsilon_{2i})\left[\frac{E_i}{(f_{cc}-f_i)} - \frac{4*E_{2i}}{(f_{cc}-f_{2i})}\right],\ D = B+1 \quad (9)$$

Where, f_c is the actual compressive stress
- f_{c0} is the uniaxial peak compressive stress
- f_{cc} is the confined peak compressive stress
- f_l is the confinement stress
- f_i is the compressive stress of the first inflection point
- f_{2i} is the compressive stress of the second inflection point
- ε_c is the actual strain
- ε_{c0} is the uniaxial peak strain
- ε_{cc} is the confined peak strain
- ε_i is the strain of the first inflection point
- ε_{2i} is the strain of the second inflection point
- E_c is the young's modulus of the concrete

2.4.2.2 Jiang and Teng

The curve is described with equation 10.

$$f_c = \frac{\left(\frac{\varepsilon_c}{\varepsilon_{cc}}\right)*r}{r-1+\left(\frac{\varepsilon_c}{\varepsilon_{cc}}\right)^r} \quad (10)$$

With:

$$r = \frac{E_c}{E_c - \frac{f_{cc}}{\varepsilon_{cc}}} \quad (11)$$

Where, f_c is the actual compressive stress
- f_{cc} is the confined peak compressive stress
- ε_c is the actual strain
- ε_{cc} is the confined peak strain
- E_c is the young's modulus of the concrete

2.4.2.3 Xiao et al

The curve is described with the same formula as for the Jiang and Teng model, equation 10. The difference between the models lies in the determination of the peak strength and peak strain, these formulas are displayed in Table 2-1. The confined stress-strain curve is displayed in Figure 2-5.

2.4.2.4 Lim and Ozbakkaloglu

The curve is described with equation 12.

$$f_c = \begin{cases} \frac{f_{cc}\left(\frac{\varepsilon_c}{\varepsilon_{cc}}\right)r}{r-1+\left(\frac{\varepsilon_c}{\varepsilon_{cc}}\right)^r} & , \ 0 \le \varepsilon_c \le \varepsilon_{cc} \\ f_{cc} - \frac{f_{cc}-f_{cres}}{1+\left(\frac{\varepsilon_c-\varepsilon_{cc}}{\varepsilon_i-\varepsilon_{cc}}\right)^{-2}} & , \ \varepsilon_c > \varepsilon_{cc} \end{cases} \quad (12)$$

With:

$$r = \frac{E_c}{E_c - \frac{f_{cc}}{\varepsilon_{cc}}}, \quad f_{cres} = 1.6 * f_{cc}\left(\frac{f_l^{0.24}}{f_{c0}^{0.32}}\right) \le f_{cc} - 0.15 f_{c0} \quad (13)$$

$$\varepsilon_i = 2.8 * \varepsilon_{cc}\left(\frac{f_{cres}}{f_{cc}}\right) f_{c0}^{-0.12} + 10 * \varepsilon_{cc}\left(1 - \frac{f_{cres}}{f_{cc}}\right) f_{c0}^{-0.47} \quad (14)$$

Where, f_c is the actual compressive stress
f_{c0} is the uniaxial peak compressive stress
f_{cc} is the confined peak compressive stress
f_l is the confinement stress
ε_c is the actual strain
ε_{cc} is the confined peak strain
ε_i is the strain of the first inflection point
E_c is the young's modulus of the concrete

2.5 Concrete under concentrated loads

Concrete under concentrated loads is a subject that is studied for quite some time now, an extensive summary on the topic of concentrated loads has been given by Song (2017). The partially loaded area beneath the anchor flange gives rise to non-linear stress development in the surrounding concrete.

The concentration of loads appears frequently on concrete structures, for instance in post-tensioned anchorage zones, bearings of bridge type structures and tunnel lining segments. When a concentrated load is introduced into a structure through a limited area, large compressive forces are transmitted. Directly under the loaded area a multi-axial stress state develops. High compressive stresses are transmitted to the concrete beneath this area, a bit further down from the loaded area tensile stresses will form through distribution of the compressive stresses. At the loaded concrete edge tensile stresses may occur. These spalling stresses in most cases will not result in actual spalling of the concrete (Breen et al 1994). The concentrated loads can be divided in two cases, the spatial case and the plane case. Where the spatial case means that both sides of the load area are smaller than the supporting concrete and the plane case means that only one side of the load area is smaller than the supporting concrete. The stresses in the spatial case are distributed in two directions and the stresses in the plane case only in one direction. The stress distribution is uniform at a depth approximately equal to the width of the structure. Within this distance the stresses can not be determined by ordinary bending theory (Leonhardt & Mönnig 1986). This region is called the “St. Venant disturbance zone”.

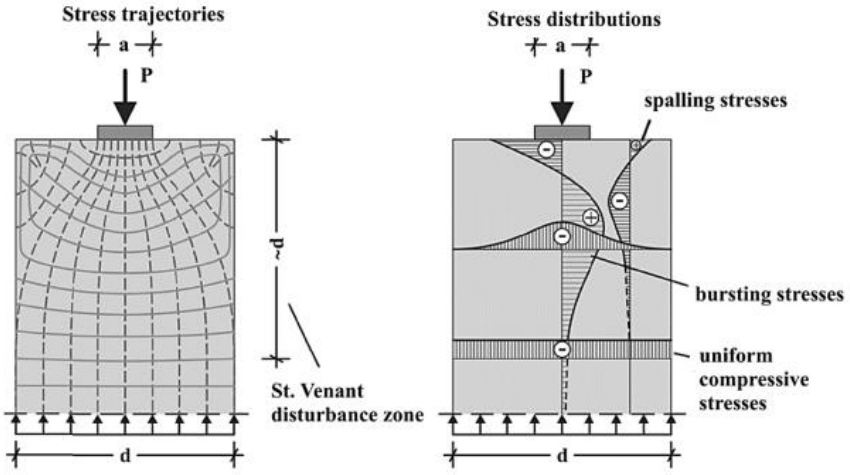

Figure 2-6: Flow of stresses in concrete member under localized force: a Stress trajectories; b: Stress distribution (Wichers 2013)

Because of the multiaxial stress states originating from the area load, larger compressive stresses in comparison with uniaxial loading are allowable. The surrounding non-loaded concrete confines the loaded concrete (Leonhardt & Mönnig 1986). In practise, concrete is often reinforced which improves its confining capacities, resulting in a larger load-bearing capacity.

Investigating the anchor cage pressing onto the concrete, it is noticed that the top flange pressing down onto the concrete resembles a plane concentrated load case. The force acting on the flange can only be distributed into the concrete in one direction. Looking at the cross section it is seen that only one side of the load area is smaller than the supporting concrete. In the other direction the ring goes round continuously. The top flange on the concrete resembles a strip partial loading case. These partially loaded area cause a multiaxial compressed stress state beneath the anchor flange, resulting in an confined area directly beneath the anchor flange and bursting stresses to develop in the concrete body.

2.6 DIANA FEA approach to confinement

A numerical procedure for analyzing analytical problems is the finite element method. The finite element method is widely used for stress analysis, heat transfer, fluid flow, lubrication, electrics and magnetic fields. The finite element method uses discretization to divide the problem into parts. This finite number of parts or elements will be connected to each other by boundary conditions. The overall issue is broken down into a number of smaller issues. For the given degrees of freedom, all of the equations that follow from the various elements are coupled and solved by the computer (Cook et al 1988, Kotsovos and Pavlović 1995).

Within the strain based crack model DIANA takes confinement into account in a two step manner. In a confined area DIANA makes use of a uniaxial compression curve in the three principal directions. These principal stresses form the principal stress vector, this stress vector is scaled until it falls at the edge of the four parameter failure surface. This scaling factor is then applied by multiplying with the uniaxial compressive stress, resulting in a strength increase factor.

2.6.1 DIANA's compressive models

There are several compressive models available within the DIANA FEA program. The following four show the most similarities with the confined compression curves described in the theory and do not need extensive input parameters which are only available after numerous dedicated experiments. These four curves are: Thorenfeldt, Parabolic, Maekawa and Hognestad. An overview of these compressive curves is described in Figure 2-7. The formulas are stated next.

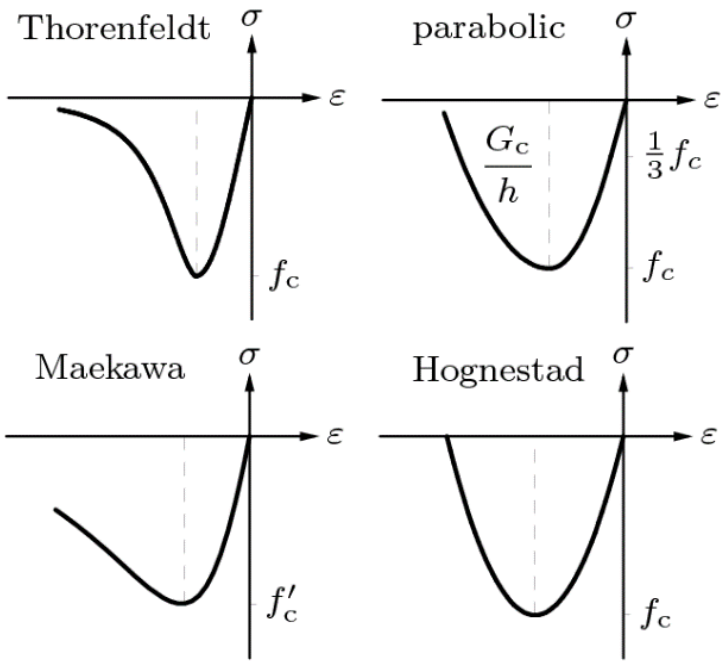

Figure 2-7: Compressive curves DIANA

2.6.1.1 The Thorenfeldt curve

The Thorenfledt compression curve is described by equation 15.

$$f_c = -f_{c0} * \frac{\varepsilon_c}{\varepsilon_{c0}} * \left(\frac{n}{n - \left(1 - \left(\frac{\varepsilon_c}{\varepsilon_{c0}}\right)^{nk}\right)} \right) \quad (15)$$

With:

$$n = 0.80 + \frac{f_{c0}}{17}\ ,\ k = \begin{cases} 1 & if\ \varepsilon_{c0} < \varepsilon_c < 0 \\ 0.67 + \frac{f_{c0}}{62} & if\ \varepsilon_c \leq \varepsilon_{c0} \end{cases} \quad (16)$$

$$\varepsilon_{c0} = -\frac{f_{c0}}{E_c} * \left(\frac{n}{n-1}\right) \quad (17)$$

Where, f_c is the actual compressive stress
f_{c0} is the uniaxial peak compressive stress
ε_c is the actual strain
ε_{c0} is the uniaxial peak strain
n is the curve fitting parameter
k is the post-peak decay term
E_c is the young's modulus

2.6.1.2 The Parabolic curve

The parabolic compression curve is described by equation 18.

$$f_c = \begin{cases} -f_{c0} * \frac{1}{3} * \frac{\varepsilon_c}{\varepsilon_{\frac{c0}{3}}} & if\ \varepsilon_{\frac{c0}{3}} < \varepsilon_c \leq 0 \\ -f_{c0} * \frac{1}{3}\left(1 + 4\left(\frac{\varepsilon_c - \varepsilon_{\frac{c0}{3}}}{\varepsilon_{c0} - \varepsilon_{\frac{c0}{3}}}\right) - 2\left(\frac{\varepsilon_c - \varepsilon_{\frac{c0}{3}}}{\varepsilon_{c0} - \varepsilon_{\frac{c0}{3}}}\right)^2\right) & if\ \varepsilon_{c0} < \varepsilon_c \leq \varepsilon_{c0/3} \\ -f_{c0}\left(1 - \left(\frac{\varepsilon_c - \varepsilon_{c0}}{\varepsilon_u - \varepsilon_{c0}}\right)^2\right) & if\ \varepsilon_u < \varepsilon_c \leq \varepsilon_{c0} \\ 0 & if\ \varepsilon_c \leq \varepsilon_u \end{cases} \quad (18)$$

With equations 19-21 describing the way of determining the characteristic strain values.

$$\varepsilon_{c0/3} = -\frac{1}{3} * \frac{f_{c0}}{E_c} \quad (19)$$

$$\varepsilon_{c0} = -\frac{5}{3} * \frac{f_c}{E_c} = 5 * \varepsilon_{c0/3} \quad (20)$$

$$\varepsilon_u = \varepsilon_{c0} - \frac{3}{2} * \frac{G_c}{h * f_{c0}} \quad (21)$$

Where, f_c is the actual compressive stress
f_{c0} is the uniaxial peak compressive stress
ε_c is the actual strain
ε_{c0} is the uniaxial peak strain
ε_u is the ultimate strain
G_c is the compressive fracture energy
E_c is the young's modulus
h is the element length

2.6.1.3 The Maekawa curve

The Maekawa compressive curve is defined by equation 22, resembled by a fracture damage parameter K.

$$f_c = -K * E_c * (\varepsilon_c - \varepsilon_x) \quad (22)$$

With:

$$K = e^{\left(-0.73\left(\frac{\varepsilon_c}{\varepsilon_{c0}}\right)*\left(1-e^{-1.25\left(\frac{\varepsilon_c}{\varepsilon_u}\right)}\right)\right)} \quad (23)$$

$$\varepsilon_x = \left(\frac{\varepsilon_c}{\varepsilon_{c0}} - \frac{20}{7}\left(1 - e^{-0.35\left(\frac{\varepsilon_c}{\varepsilon_{c0}}\right)}\right) * \varepsilon_{c0}\right. \quad (24)$$

$$\varepsilon_{c0} = -2 * \frac{f_{c0}}{E_c} \quad (25)$$

Where, f_c is the actual compressive stress
f_{c0} is the uniaxial peak compressive stress
ε_c is the actual strain
ε_{c0} is the uniaxial peak strain
K is the fracture damage parameter
E_c is the young's modulus

2.6.1.4 The Hognestad curve

The Hognestad compressive curve is described by the equation 26.

$$f_c = -f_{c0} * \left(2 * \frac{\varepsilon_c}{\varepsilon_{c0}} - \left(\frac{\varepsilon_c}{\varepsilon_{c0}}\right)^2\right) \quad (26)$$

With the characteristic strain value determined by equation 27.

$$\varepsilon_{c0} = -\frac{2f_{c0}}{E_c} \quad (27)$$

Where, f_c is the actual compressive stress
f_{c0} is the uniaxial peak compressive stress
ε_c is the actual strain
ε_{c0} is the uniaxial peak strain
E_c is the young's modulus

2.6.2 Hsieh-Ting-Chen four-parameter failure surface

DIANA makes use of the four-parameter Hsieh-Ting-Chen failure surface to calculate the increase of strength with increasing isotropic stress. This model is presented by Hsieh et al (1981) and is developed for the implementation of finite element calculations of concrete. A visualization of the failure surface is given by Figure 2-8, it represents the general failure surface in principal stress space.

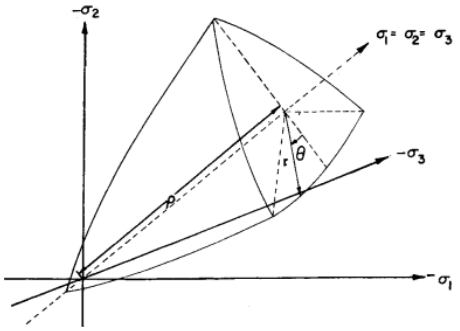

Figure 2-8: Failure surface (Hsieh et al 1981)

The parameters representing the failure surface can be described wit equation 28.

$$\rho = \frac{1}{3} I_1 \,,\; r = \sqrt{2J_2},\; \theta = \cos^{-1}\left(\frac{\sqrt{3}}{2}\frac{S_1}{\sqrt{2}}\right),\; |\theta| \leq 60° \qquad (28)$$

With:

$$I_1 = \sigma_1 + \sigma_2 + \sigma_3 \qquad (29)$$

$$J_2 = \frac{1}{6}((\sigma_1 - \sigma_2)^2 + (\sigma_2 - \sigma_3)^2 + (\sigma_3 - \sigma_1)^2) \qquad (30)$$

$$S_1 = \sigma_1 - \frac{1}{3} I_1 \; if \; \sigma_1 > \sigma_2 > \sigma_3 \qquad (31)$$

If a constant value is taken for θ, r becomes a nonlinear function of ρ. This formula is described with equation 32.

$$f(\rho, r, \theta) = \alpha r^2 + (\alpha \cos\theta + \beta) r + C\rho - 1 = 0 \qquad (32)$$

Equation 32 can be rewritten as the characteristic four-parameter criteria which is displayed by equation 33. The four constants are determined by fitting the formula to: the uniaxial compressive and tensile strength, the biaxial compressive strength and experimental data of triaxial tests on concrete specimen.

$$f = 2.0108 * \frac{J_2}{f_{c0}^2} + 0.9714 * \frac{\sqrt{J_2}}{f_{c0}} + 9.1412 * \frac{f_{c1}}{f_{c0}} + 0.2312 * \frac{I_1}{f_{c0}} - 1 = 0 \qquad (33)$$

With:

$$f_{c1} = \max \; principal \; stress \; (\sigma_1, \sigma_2, \sigma_3) \qquad (34)$$

Where, I_1 is the first stress invariant
J_2 is the second deviatoric stress
f_{c1} is the maximum principal stress
f_{co} is the uniaxial compressive strength

The strength increase factor is calculated by dividing the failure strength by the uniaxial compressive strength, shown by equation 35.

$$K_\sigma = \frac{f_{cf}}{f_{c0}} \geq 1 \qquad (35)$$

The peak strain factor by DIANA is assumed to be the same as the peak stress factor.

$$K_\varepsilon = K_\sigma \qquad (36)$$

So in DIANA the increase in strain capacity is directly linked to the increase in strength of the specimen.

3 LINEAR ELASTIC STRESS SITUATION

An understanding of the magnitude and direction of the stresses developing under and around the anchor flange is required. To get an insight in where the confinement will develop and to investigate the level of this confinement. To get this insight of the occurring stress situation around the anchor flange, the assumption is made to start with a linear material model. The stresses are a result of the pre-tensioning and the overturning moment. Before the calculations can be made a clear understanding of the properties and dimensions is stated. First a SCIA calculation is made to calculate the stresses directly beneath the anchor flange. Later DIANA models representing the foundation are made, this is to investigate the stress development in the concrete.

3.1 Dimensions, properties and loads surrounding the anchor cage

In the following paragraph the dimensions and properties of the concrete body are discussed. Followed by the dimensions of the anchor cage. Then the loads on the foundation resulting from the tower are stated.

3.1.1 Dimensions and properties of the concrete body

The dimensions of the concrete wind turbine foundation will show some deviations for different projects. But the overall constructive design will be the same. The concrete body is build up out of two distinct parts with different concrete properties. The concrete base and the concrete pedestal on top. The dimensions and properties of the reference project are shown in Figure 3-1 to 3-2 and Table 3-1.

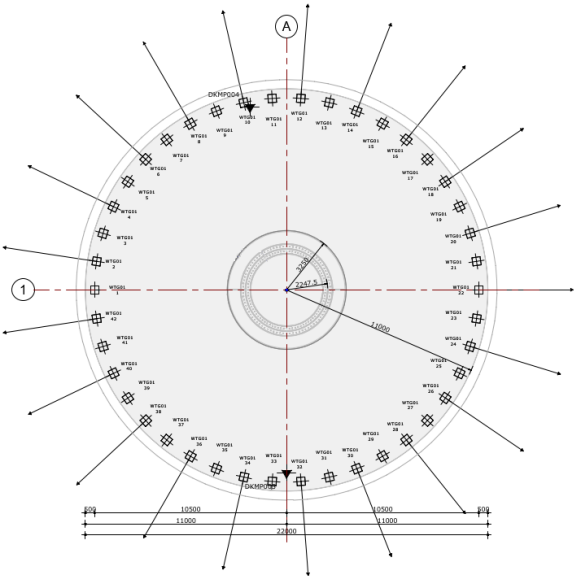

Figure 3-1: Top view wind turbine foundation

Displayed in Figure 3-1 is the top view of the wind turbine foundation. It is seen that the piles are situated on the outer ring. The foundation has a diameter of 22 meters.
A cross section of the foundation is displayed in Figure 3-2. The bottom cylinder of the foundation has a height of 1.5 meter, which then is tapered in over a height of 1.5 meter. The pedestal has a height of 600 mm and a diameter of 6.5 meter.

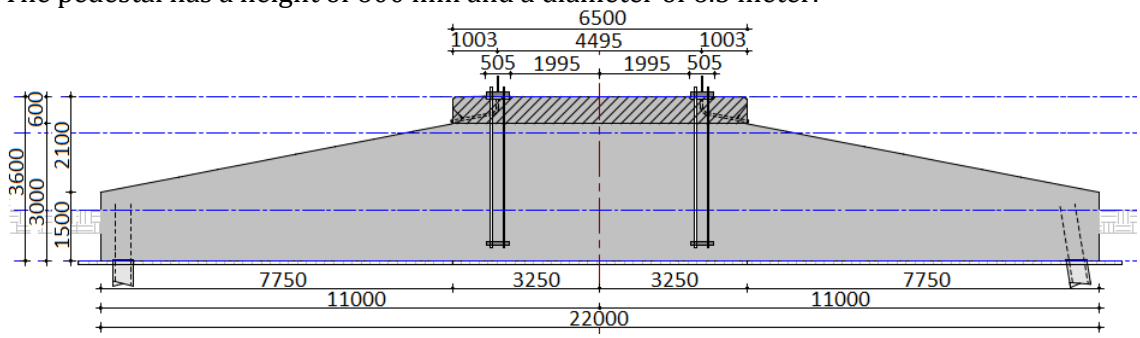

Figure 3-2: Cross section wind turbine foundation

The concrete properties of the foundation are displayed in Table 3-1.

Table 3-1: Concrete strength

Component	**Strength class**
Concrete pedestal	C55/67
Concrete base	C30/37

3.1.2 Dimensions of the anchor cage

As described and displayed before the anchor cage is situated in the middle of the concrete body to ensure the connection with the tower. The anchor cage is specially designed to cope with the imposed loads for the particular wind turbine. The flange dimensions, diameter, thickness and width will be customized to the project. The top and bottom flange does not has to be the same in dimensions. The anchor rods amount and dimensions are also fitted to the project. This will occur in proper consultation with the tower manufacturer to ensure a fitting connection. The dimensions of the anchor cage are displayed in Figures 3-3 to 3-6.

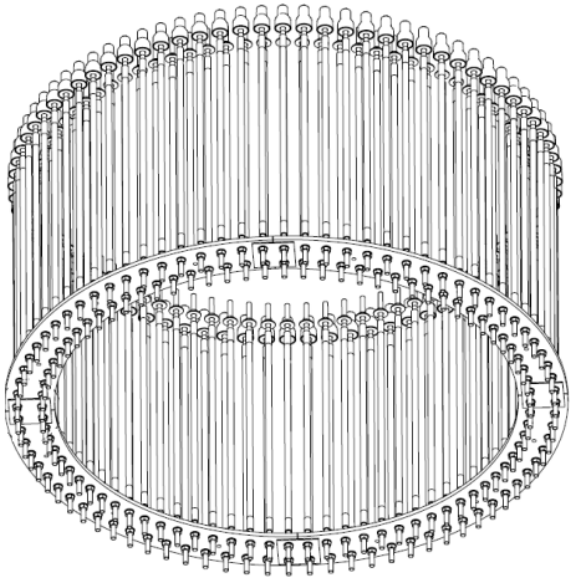

Figure 3-3: Anchor cage

Figure 3-3 shows a schematic view of the anchor cage with the bottom flange being horizontal and the anchor rods being displayed vertical.

Displayed in Figure 3-4 is the top anchor flange. This flange will be part of the tower in the finished design. When the concrete foundation is poured around the anchor cage a secondary anchor flange is fitted to the top of the anchor rods. This is to ensure a tight fit with the bottom flange of the tower. The secondary flange is used as a template to hold the anchor rods in place. The top flange of the anchor cage is T-shaped with holes on either side of the middle rib.

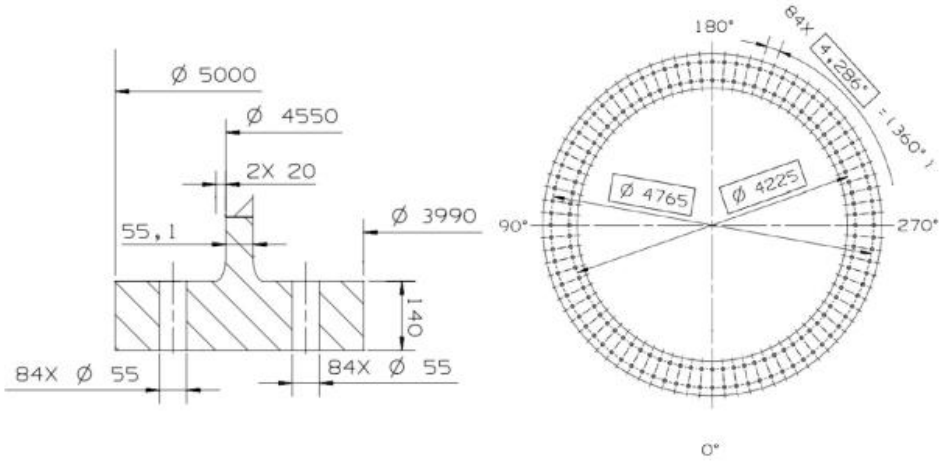

Figure 3-4: Top flange dimensions

A schematic view of the anchor rod is displayed in Figure 3-5. At the end the rods are fitted with screw-thread, in the middle the anchor is isolated. This will guarantee that friction can not develop between the rod and the concrete during prestressing. So only the anchor plates are pressing onto the concrete.

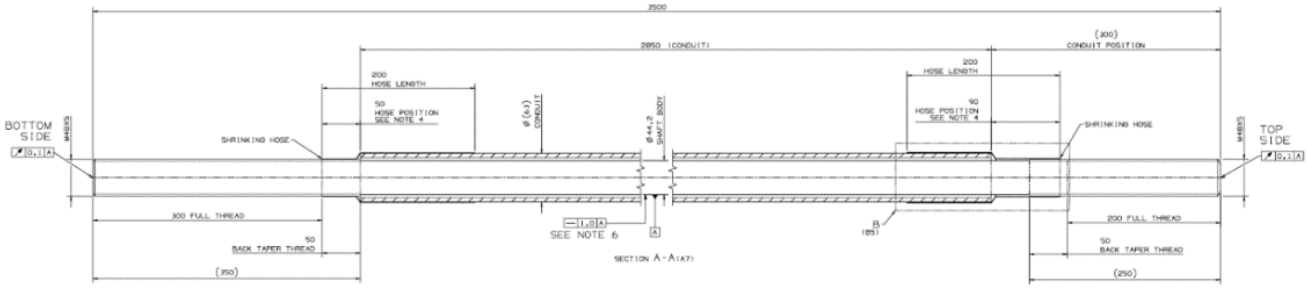

Figure 3-5: Anchor rod dimensions

The bottom anchor plate is presented in Figure 3-6. This is a cross section of a disk, same as the top flange. The outer dimensions are the same as the top flange, the thickness can differ from each other. This is mainly because the extra forces being present in the top flange require a larger thickness.

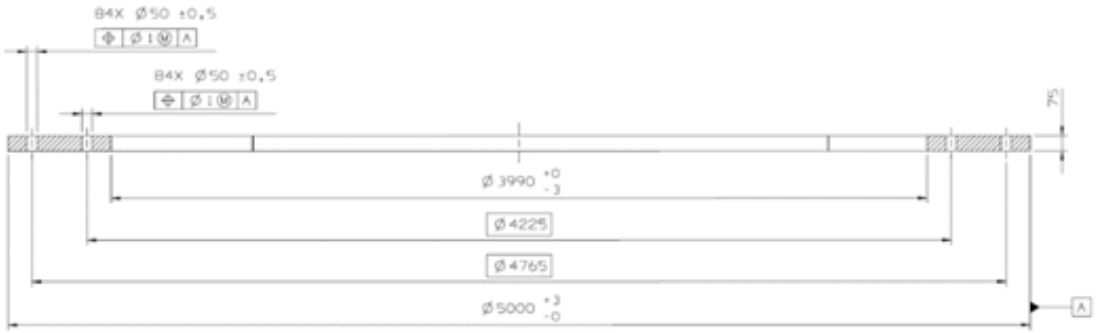

Figure 3-6: Bottom flange dimensions

3.1.3 Loads on the anchor cage

The forces acting on the foundation slab are originating from the gravity, the wind and the surrounding soil. The gravity pulls on the large slab resulting in a downward force on the surrounding soil or piles. The gravity also pulls on the wind turbine itself resulting in a vertical force on top of the foundation slab. The use of the wind turbine is to capture the energy from the wind, so it needs to cope with large forces resulting from the wind. The wind blowing against the blades and tower will result in an horizontal force on the foundation slab. These wind forces are also resulting in a overturning moment, the wind wants to tip the turbine tower over. A schematic view of the loads is presented in Figure 3-7. Depending on the foundation slab design the surrounding soil and or piles result in support reactions on the foundation slab. Being the supports of the foundation slab these forces need to be in equilibrium with the other imposed forces. The ground water level at the construction site influences the buoyancy of the foundation slab. This buoyancy can enlarge the chance of uplift to occur, even if the ground water rises only for a short period of time.

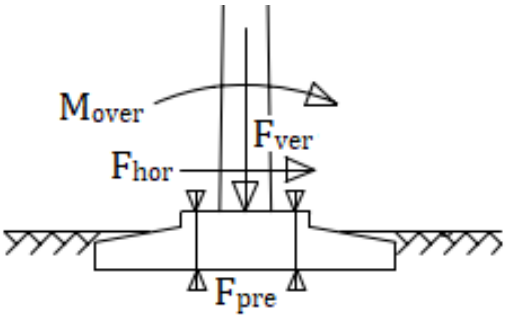

Figure 3-7: Forces on foundation

The three main loads acting on the anchor cage resulting from connection with the tower are: a downward vertical force (F_{hor}), a horizontal force (F_{ver}) and a overturning moment (M_{over}). As displayed in Figure 3-7. These loads are taken from the reference project where they were determined by different loading combinations. The loads displayed in Table 3-2 express the maximum loads resulting from the different loading combinations. After applying the loads on the top of the anchor cage, the top flange is rotated until the foundation fails. For the reference project this is done by means of a non linear finite element analysis. The extra rotation results in an extra moment load. This moment load at failure is denoted as failure moment load (M_{fail}). The connection between the tower and the foundation is made by means of the anchor cage as described before. The anchor rods connecting the top and bottom flange of the anchor cage are prestressed after installation of the tower, this force is indicated as the prestressing force.

Table 3-2: Loads on the foundation

Description		**Quantity**	**Factor**	**ULS**	**Unit**
Horizontal force	F_{hor}	912	1.35	1231	kN
Vertical force	F_{ver}	7658	1.35	10338	kN
Overturning moment	M_{over}	135213	1.35	182538	kNm
Moment Failure	M_{fail}	n/a	n/a	290675	kNm
Prestressing force	F_{pre}	401	1.00	401	N/mm^2

It is concluded from Table 3-2 that the influence of the horizontal and vertical force on the stress development beneath the anchor flange is small relative to the prestressing and moment load. Because of this only the prestressing and moment load are taken into consideration for calculating the stress trajectories beneath the anchor flange.

3.2 Stresses directly below top anchor flange

To get a grasp on the stresses developing in the concrete directly below the anchor flange as a result of the acting forces a SCIA calculation is made. For this calculation, plane sections are assumed to remain plane. The top flange is assumed to be supported by a spring support. For this a bedding constant (Kc) is calculated in appendix I, this represents the resistance of the concrete. For the calculation x represents the distance to the point of rotation and φ the rotation angle, displayed in Figure 3-8.

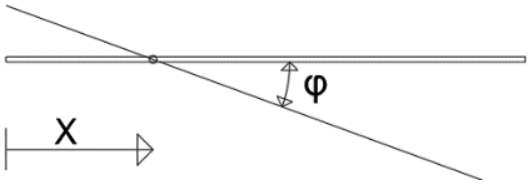

Figure 3-8: Description x and φ

The horizontal force will initially not result in a stress beneath the anchor flange and is left out of consideration for this calculation. The vertical force is divided by the area of the top flange to get the stress directly beneath the anchor flange. The total prestressing force can also be divided by the total area for the resulting compressive stresses directly beneath the anchor flange. So the stresses beneath the flange are just the force divided by the area of the flange pressing into the concrete. The overturning moment will try to rotate the top flange, pressing on one side of the flange and pulling on the other side. As long as the pre-tensioning force is larger than the pulling force from the moment, the top flange will keep its contact with the concrete. In ULS the pulling force on the top flange will overcome the prestressing force and the top flange will lose contact with the concrete resulting in a shifting of the stiffness. On the pulling side the stiffness is determined by the anchor rods and on the pushing side the stiffness is determined by the concrete body. The point of rotation will shift away from the middle resulting in an increase in the compressive load on the concrete. In the SCIA model the top anchor flange is supported by an area support representing the underlying concrete with Kc as the bedding constant. The anchor rods are modelled as steel rods connected to the top flange and supported by pin supports at the bottom. The prestress is applied as a thermal load on the anchor rods, the moment is applied on the top flange. A non-linear calculation is made to include the support non-linearity, calculating with only compressive forces in the support. The SCIA calculation report is presented in Appendix II. The main results are displayed in Table 3-3.

Table 3-3: SCIA results

Results	**unit**	**SCIA**
Uz prestress	mm	0.58
σ_c prestress	N/mm^2	-14.5
ϕ	rad	0.0013
X	mm	2908
σ_c Total	N/mm^2	-66.0

Seen is that the deflection from the prestress results in a uniform compressive stress in the concrete. This is as expected because the prestressing anchors are exerting an equal tension force divided over the top flange. As described before the moment will increase at the compression side and decrease at the tension side. When the tension stresses resulting from the moment become larger than the compressive stresses resulting from the prestressing, the compressive area will decrease. This will increase the compressive stress that is excreted into the concrete directly below the top flange. Directly below the top flange there is a thin grout layer which ensures a seamless fit between the concrete body and the top flange. The prescribed grout layer strength is of C100/115, to cope with the high local stresses. The SCIA analysis findings will act as an upper limit of the compressive stresses.

3.3 Stress development in the concrete

To get an insight in the stress development in the concrete beneath the anchor flange, two models are used. An axisymmetric DIANA model and a 3D DIANA model. The outcomes of the two models are compared to check whether the modelling choices have any effect on the stress development. The 3D DIANA model is representing half of the turbine foundation making use of the symmetry axis. Because of the predominantly small vertical force, emphasis is put on the pre-tensioning and the overturning moment.

3.3.1 Axisymmetric model description

The axisymmetric model resembles half of the cross section of the total foundation. Being an axisymmetric model the model is rotated around the vertical y-axis resulting in a cylindrical model. The anchor rods are modelled as reinforcements with the same total surface area as the anchors. The prestressing load in the anchors is applied by a pre tensioning load in the reinforcements. The moment load can not be applied on this model because no moment arm can be formed. The simplification is made to leave the concrete part beneath the bottom anchor plate out of consideration. This to ensure that the concrete is not pulling on the bottom plate. The model is supported by hinge supports resembling the pile supports of the foundation. The stresses are extracted from the model at the placing of the red line in between the two anchor rows, as displayed in Figure 3-9.

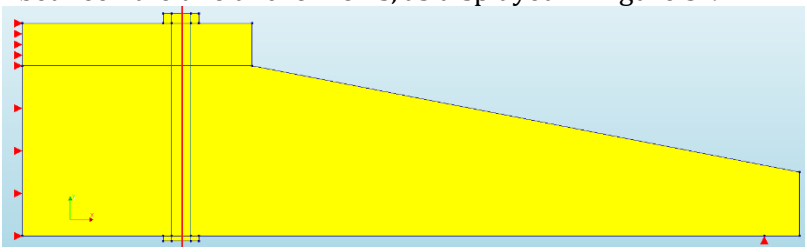

Figure 3-9: The axisymmetric model

3.3.2 DIANA 3D model description

The 3D model resembles half of the total wind turbine foundation. This is done to ensure the moment can still be applied by means of tension and compression stresses on top of the anchor flange. The prestressing force is applied by implementing a pre-tensioning load on the modelled anchor rods. The model is supported in the same way as the axisymmetric model, with hinges at the location of the piles. To compare the stresses they are extracted from the same place as in the axisymmetric model, between the two rows of anchor rods. The model is displayed in Figure 3-10.

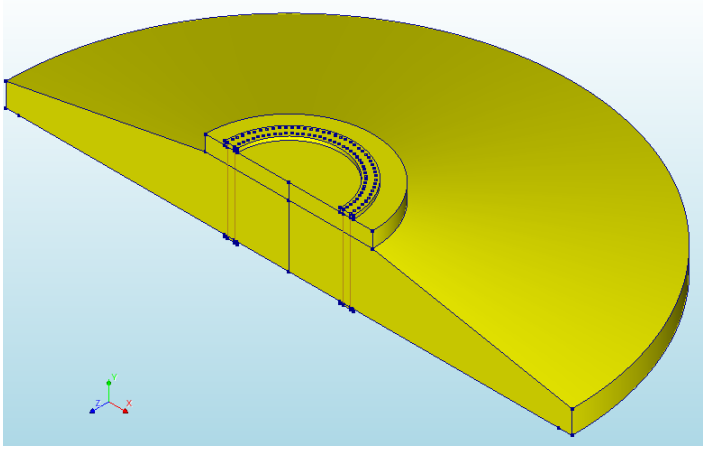

Figure 3-10: The 3D model

3.3.3 Pre-tensioning stresses

The pre-tensioning force is applied when the tower is connected to the foundation, before the wind turbine is taken in operation. This causes the initial stress situation for the foundation. A pre-tensioning force of 401 N/mm² is applied on the anchor rods. The results are displayed in Figure 3-11, the values of the three stress directions are taken in between the two anchor rows. The results from the axisymmetric model are presented with straight lines and denoted with the caption Axi. The results from the 3D model are presented with dashed lines and denoted with 3D.

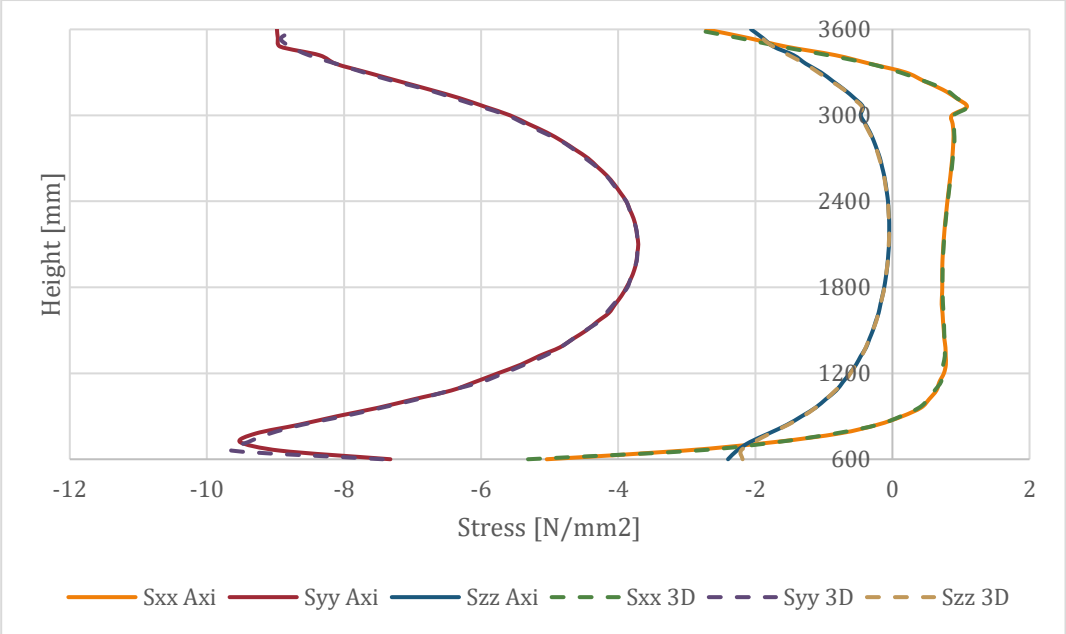

Figure 3-11: Pre-tensioning stresses in the concrete over the height; Syy, Szz, Sxx from left to right

Looking at the development of Syy stresses it is seen that the pre-tensioning of the anchors is transmitted from the anchor plate into the concrete and divided over an increasing area. Because of the larger active area the stresses are less in the middle of the concrete body, then at the top and bottom. This distribution of Syy stresses gives rise to bursting stresses in the X-direction of the model. The Sxx stress development is characteristic for a partially loaded area. The partially loaded area gives rise to compressive stresses directly below the loaded area. Deeper in the structure bursting stresses will develop. These bursting stresses are tension stresses inside the concrete body. The Szz stresses originate from the concrete body supporting itself in tangential direction. Because of the solid ring the concrete is prevented to deform in this direction and pushes on itself giving rise to compressive stresses. The larger the stresses on top pushing on the concrete the larger the tangential stresses become. This is why the Szz stresses are the highest at the top and bottom of the concrete body.

It is seen in Figure 3-11 that for the area directly beneath the anchor plate a state of triaxial compression is present, being compressed from al three directions. This area reaches to a depth of about 350 mm beneath the anchor flange. So this part of the concrete body will always be in compression and confinement will be present.

3.3.4 Overturning moment

The overturning moment could only by applied on the 3D model. A total overturning moment of 290675 kNm as described in Table 3-2 is applied on the total model. This is applied on the top flange with a factor of 1 on the left decreasing to a factor of -1 to the right. A schematic view is displayed in Figure 3-12. Leading to a triangular load shape, with zero moment being applied on the middle of the turning axis.

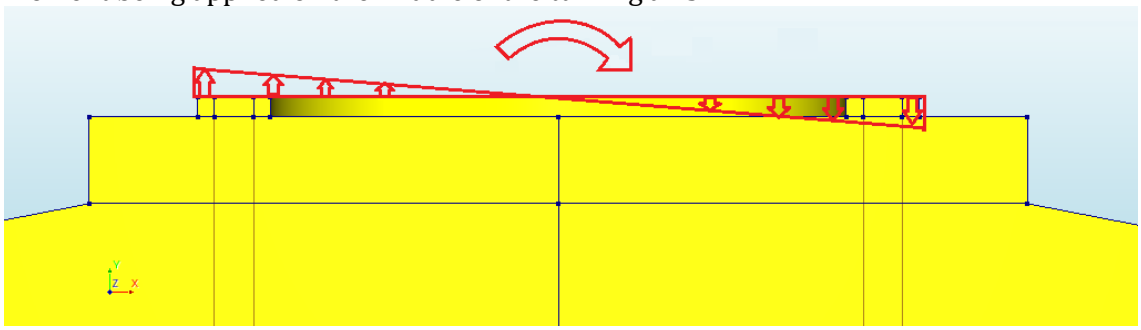

Figure 3-12: Schematic view of the moment load on 3D model

Displayed in Figure 3-13 is the effect of the moment on the pushing side in the middle between the inner and outer anchor. This is between the inner and outer anchor rod at the right side in Figure 3-12.

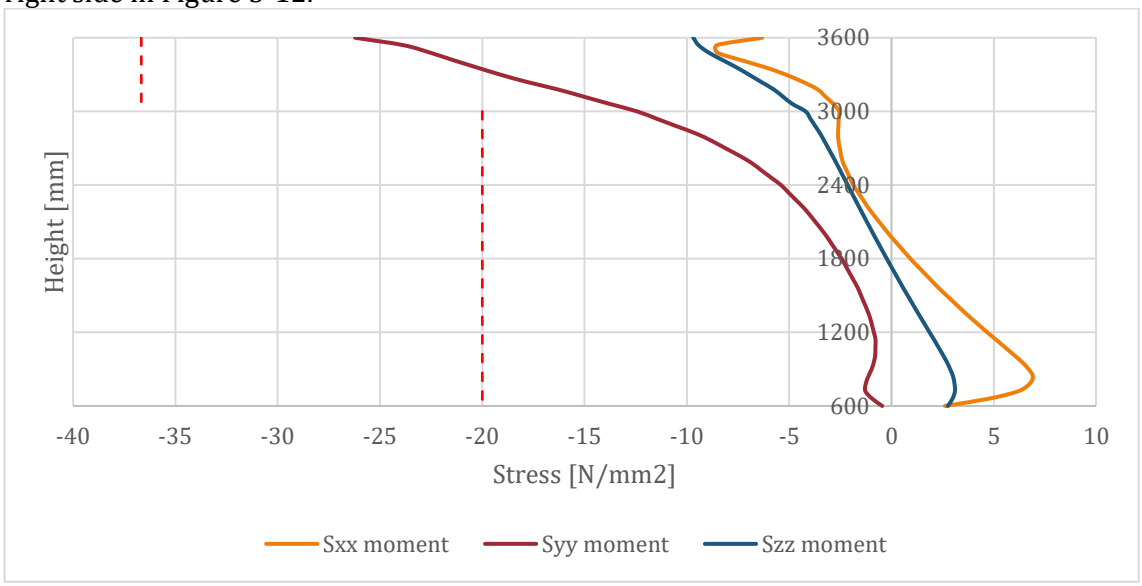

Figure 3-13: Moment stresses in the concrete over the height; Syy, Szz, Sxx from left to right

Observing the effect of the overturning moment on the Syy stresses it is noticed that the anchor flange presses onto the concrete resulting in large a compressive stress. These compressive stresses distribute over the concrete body resulting in a decrease of the compressive stress further down. In the x-direction the Sxx stresses show a compressive stress at the top and a tension stress further down in the concrete body. For the top half of the concrete body this will mean that the bursting stresses will be reduced and that a larger part of the concrete body will be in multiaxial compression. The large compressive stresses in the top part of the concrete body will result in compressive stresses in the tangential direction. Resulting in a large multiaxial compressed area at the top part of the foundation resulting from the overturning moment. The maximum compressive stress is denoted with the vertical dashed red line. As a result from the moment load confinement will take place at the top half of the concrete foundation.

3.3.5 Combined action prestressing and overturning moment

Looking at the results of the prestressing combined with the overturning moment Figure 3-14 is obtained. The two load cases combined result in a larger load on the foundation. The bursting stresses caused by the prestressing are overcome by the compressive stresses induced from the moment resulting in a larger section with compressive stresses at the top of the foundation. Because the stresses in X and Y-direction are larger in compression the stresses in Z-direction are also getting larger, resulting in a larger area being in multiaxial compression.

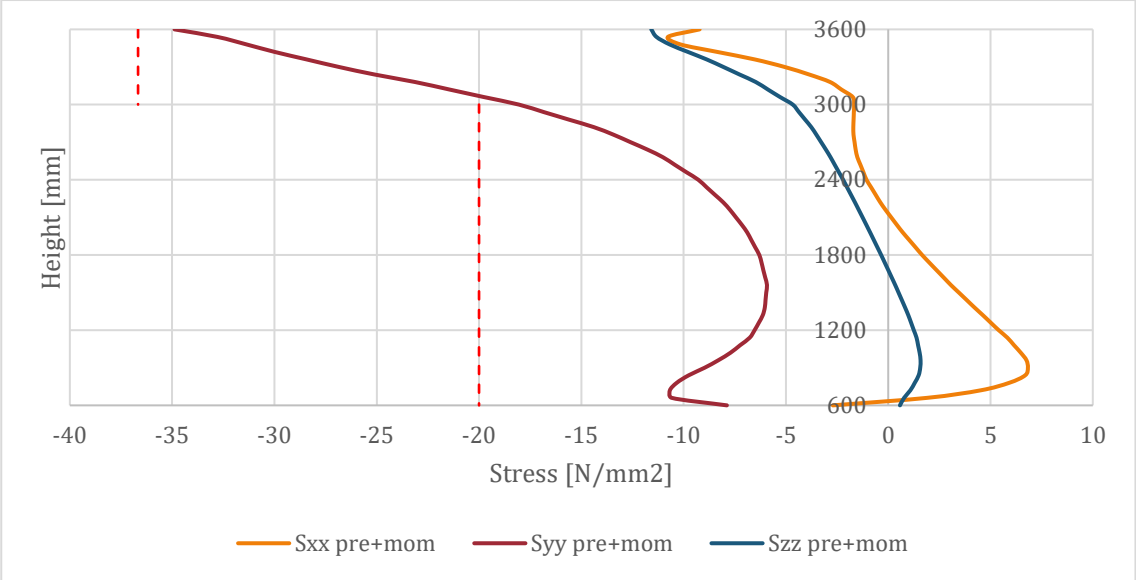

Figure 3-14: Stresses resulting from moment and prestressing in the concrete over the height; Syy, Szz, Sxx from left to right

It is clearly seen that there is multiaxial compression in the top half of the concrete surrounding the anchor cage. Focussing at the magnitude of the confinement and the Syy as the load it is noted that the load is 34.9 N/mm^2 directly beneath the flange. It is seen that Sxx is the lowest compressive stress and thus also indicates the level of confinement. For the top half of the foundation there is a confinement present going up to 10.0 N/mm^2.

3.3.6 Overall occurring confinement

So the prestressing will result in a confined area beneath the anchor flange reaching a depth of about 350 mm. The confinement will vary from almost 2 to 0 N/mm^2. This confinement will always be present at the top an act as the starting situation. The confinement resulting from the combined moment and prestressing load will be present in the top half of the foundation and vary from 10 to 0 N/mm^2.

3.3.7 Significance of confinement

Looking at the capacity utilisation of the concrete body beneath the anchor flange and comparing this with the strength increase of the different confinement models Figure 3-15 is obtained. The unity check is calculated by dividing the load by the calculated compressive strength of the relevant analytical model with the confinement present and displayed over the height of the foundation. The different confinement models described in the theory are compared by the peak strength value. The unity check without considering confinement is displayed by the dashed line for comparison. The large spike in the graph at a height of 3000 mm is originating from the difference in concrete strength of the base and the pedestal. Overall a large strength increase is noted resulting in a much lower value of the unity check. There are some variations noted between the different confinement models but all follow the sort of same curve, the strength increase will differ a bit. These differences are the result of different approached in calculating the compressive strength increases in the different analytical models.

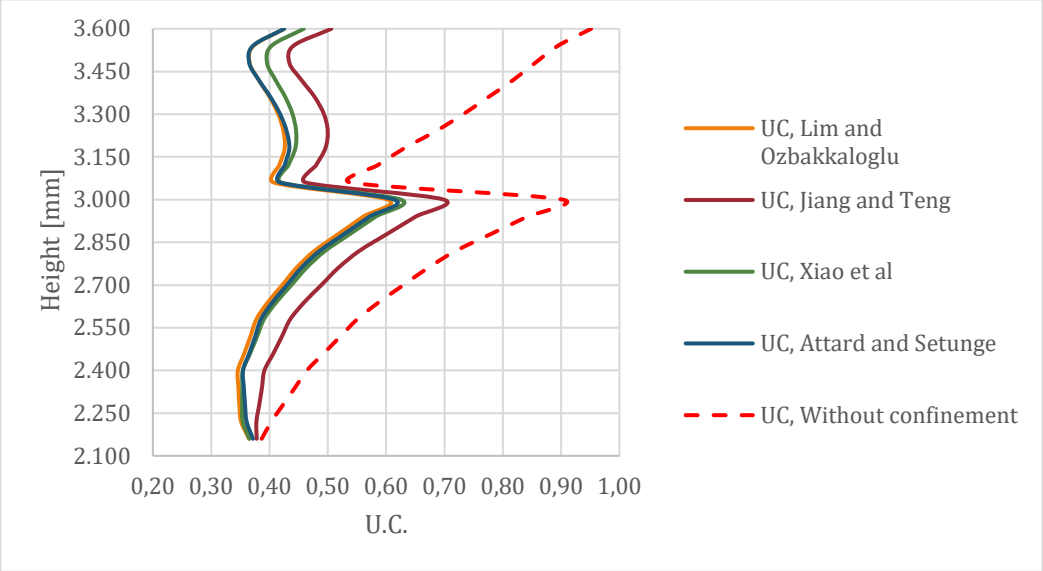

Figure 3-15: Unity check over height of the foundation

So without taking the confinement into consideration a unity check of 0.95 is found at the top of the foundation. This reduces to 0.50 when taken the confinement into consideration, making use of the analytical confinement models. At a height of 3000 mm in the foundation where the confinement is only 1.7 N/mm^2 the unity check of 0.54 is decreased to 0.46. Which indicates a significant improvement even at a low confinement level. So correctly capturing these enhanced properties by DIANA will have great impact on the elements being present in confined areas.

4 COMPARISON OF IDEAL CONFINEMENT CASE

To get an insight in the way DIANA approaches confinement a series of analysis is made. The model used is simplified to only the bare minimum needed to capture confinement. This is done to remove any unnecessary variables that could influence the confinement. The tested model represents a axisymmetric model of a cylinder. The axisymmetric model is meshed with one element to ensure a homogeneous stress distribution within the element. These model is tested in the earlier described confinement range present in the foundation, ranging from 0.0 to 10.0 N/mm^2. The model is tested for all the four different compressive behaviour models. The results of the DIANA models are compared with the values of the analytical models and experimental results. Mainly focussing on the peak strength and peak strain.

4.1 Comparing DIANA compressive curves, analytical models and experimental values

To compare the compressive behaviour models they are weighted against the described analytical models and the experimental data values. So for the different confinement levels the stress-strain diagram is calculated using the analytical models. These curve are compared to the stress-strain curves calculated by DIANA making use of the different compressive behaviour models. The peak of these stress-strain curves will be compared to experimental data on confinement test performed by many researchers.

4.1.1 Analytical models

The stress-strain curves coming from the DIANA models are compared with the stress-strain curves obtained from the analytical confinement models. These models specially designed for describing the compressive curves of confined concrete are described earlier in the literature review. They are described at paragraph 2.4. These four analytical models being: Attard and Setunge, Jiang and Teng, Xiao et al and Lim and Ozbakkaloglu.

4.1.2 DIANA compressive curves

The DIANA model used for the comparison of the compressive curves is a axisymmetric model, representing a cylinder. The model is 200 mm in height and 100 mm in width, representing a standard compressed cylinder. The model is displayed in Figure 4-1. At the bottom the model is supported in Y direction, at the left side the model is supported in X direction. The confining load is applied on the right side of the model. The model is calculated with a confining pressure of: 0; 1.0; 5.0 and 10.0 N/mm^2. The top load is applied by a prescribed deformation situated at the top side, this deformation is 2 mm in total. This deformation is large enough to cause failure of the element and not excessively large which would only enlarge the calculation time unnecessary. The model has runed four times for each confinement stress. One time for each of the in the literature review described compressive model, being: Parabolic, Thorenfeldt, Maekawa and Hognestad compressive curve. The model is calculated and meshed with one element representing the whole model, causing a homogeneous and ideal stress distribution.

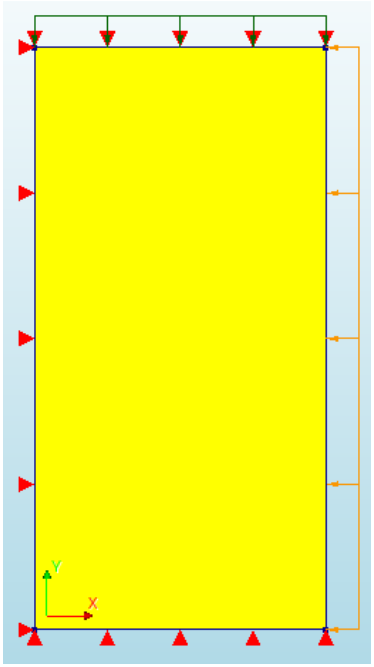

Figure 4-1: DIANA model

The different DIANA models has runed with the parameters described in Table 4-1. These parameters are the same as the parameters being used for the earlier performed linear analysis.

Table 4-1: Parameters for DIANA model used for compressive behaviour comparison

Parameter	**Value**	**Unit**
Young's modulus	38200	N/mm^2
Poisson ratio	0.2	-
Compressive strength	63.0	N/mm^2
Compressive fracture energy	24.2	N/mm^2

4.1.3 Experimental values

For comparison the mean values of the peak strength and peak strain are derived from a database of actively confined concrete experiments. This database of actively confined concrete is compiled by Lim and Ozbakkaloglu (2015) for the developing a confinement model for concrete confined with fiber reinforced polymers. In this study the actively confined experiments are compared to experiments conducted with reinforced polymers. The database is displayed in Appendix 3. The comparison is made up to a confinement ratio (f_l/f_{co}) of 10/63 = 0.16, because of this the database results are displayed up to a confinement ratio of 0.2. The confinement ratio on the horizontal axis is plotted against the strength enhancement ratio (f_{cc}/f_{co}) on the vertical axis. A trendline is formed out of these data points to calculate the strength increase factor at the applied confinement ratios. This trendline is the best fitting curve so represents a mean value. For the strength enhancement ratio the upper and lower quartile are indicated with the blue line above and below the black trendline. The datapoints and trendline with its upper and lower quartile are displayed in Figure 4-2.

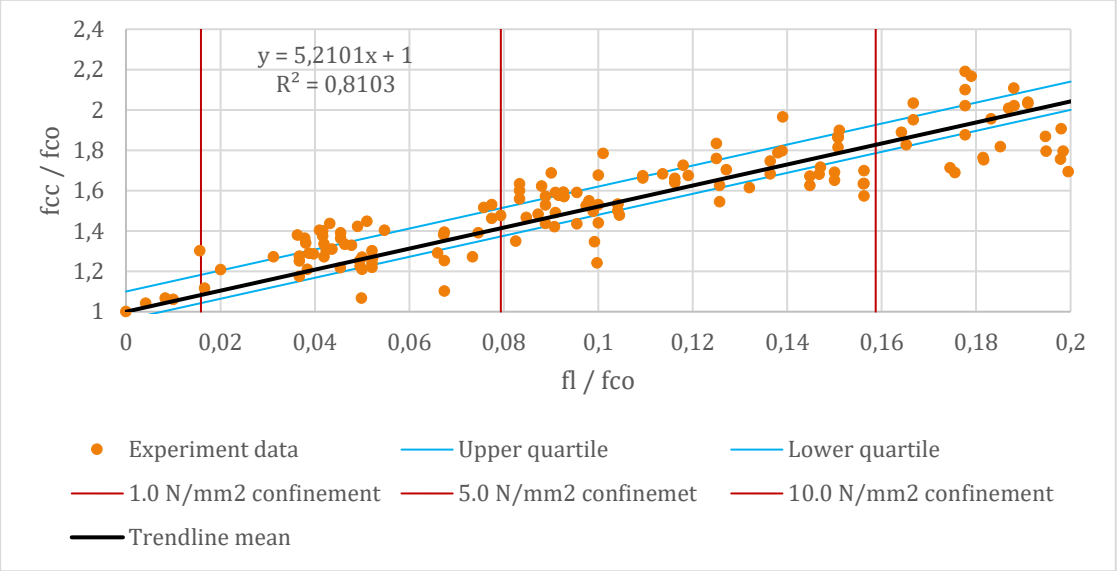

Figure 4-2: Strength enhancement ratio from experimental database

The strain enhancement ratio figure is constructed in the same manner. All the datapoints up to a confinement ratio of 0.2 are presented. A trendline is added showing the best fitting line in black. The upper and lower quartile are indicated by the blue lines in the figure. The strain enhancement ratio is displayed in Figure 4-3.

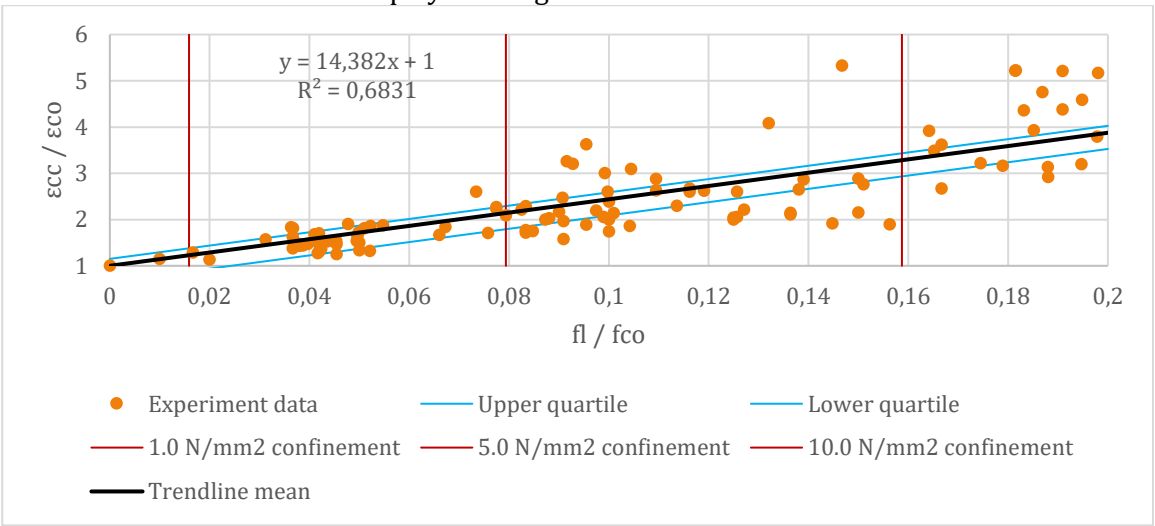

Figure 4-3: Strain enhancement ratio from experimental database

The enhancement ratios are calculated for three confinement ratios, representing the three confinement levels of 1.0, 5.0 and 10.0 N/mm^2. These confinement ratios are denoted with the red lines in Figure 4-2 and 4-3. Using the formula of the trendline the strength and strain enhancement ratios can be calculated. These formulas are displayed in the upper left corner of Figure 4-2 and 4-3. The enhancement ratios of the upper and lower quartile line are also calculated. These results for the different confinement values are displayed in Table 4-2.

Table 4-2: Experimental values

Confinement	**f_l [N/mm^2]**	**1**	**5**	**10**
Unconfined peak stress	f_{co} [N/mm^2]	63	63	63
Unconfined peak strain	ε_{co} [-]	0.0021	0.0021	0.0021
Confinement ratio	f_l / f_{co} [-]	0.016	0.079	0.159
Mean confined peak stress	f_{cc} [N/mm^2]	68.2	89.1	115.1
Lower quartile peak stress	f_{cc} 25% [N/mm^2]	65.7	86.5	112.6
Upper quartile peak stress	f_{cc} 75% [N/mm^2]	74.5	93.4	121.4
Mean confined peak strain	ε_{cc} [-]	0.0026	0.0045	0.0069
Lower quartile peak strain	ε_{cc} 25% [-]	0.0021	0.0038	0.0062
Upper quartile peak strain	ε_{cc} 75% [-]	0.0029	0.0048	0.0072

4.1.4 Results

The results of the comparison are displayed in Figure 4-4 to 4-7. The total curves are displayed at the top of each page. The top of the curves is displayed in the middle and the peak stress against the peak strain at the bottom of each page. The compressive curves originating from DIANA compressive curves are displayed with a solid line, the analytical compressive curves are displayed using dashed lines. The interquartile range of the experiments is displayed by a red box highlighting the area in the graph. The mean values of the experiments are denoted by the black line inside of the interquartile range. This area gives an estimation of the scattering of the experimental values.

4.1.4.1 Comparison with zero confinement

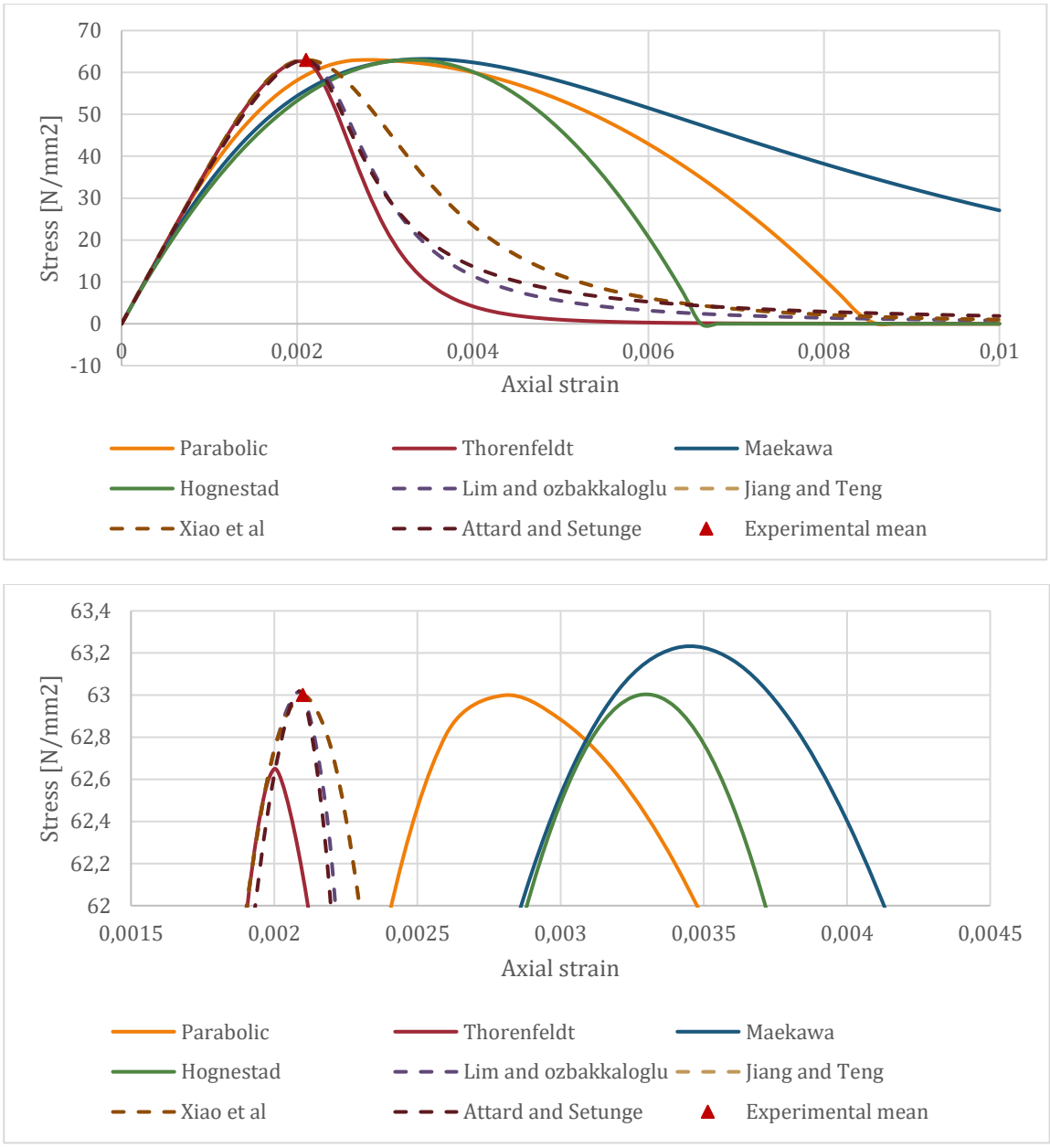

Figure 4-4: Comparison at 0.0 confinement; top, Total curves; middle, Top of the curves; bottom, Peak of the curves

4.1.4.2 Comparison with 1.0 N/mm^2 confinement

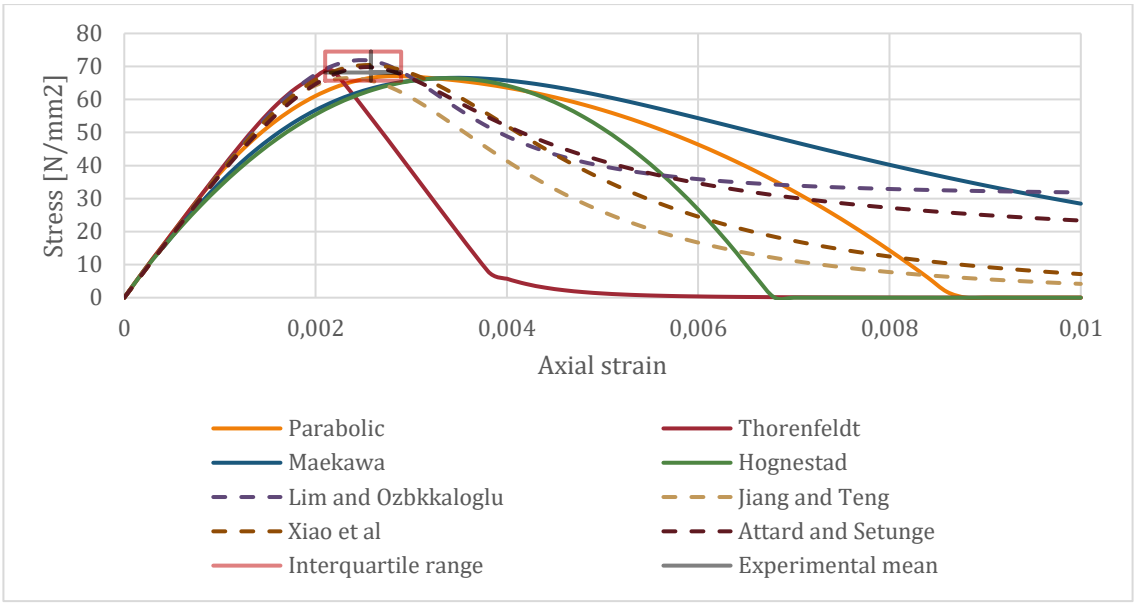

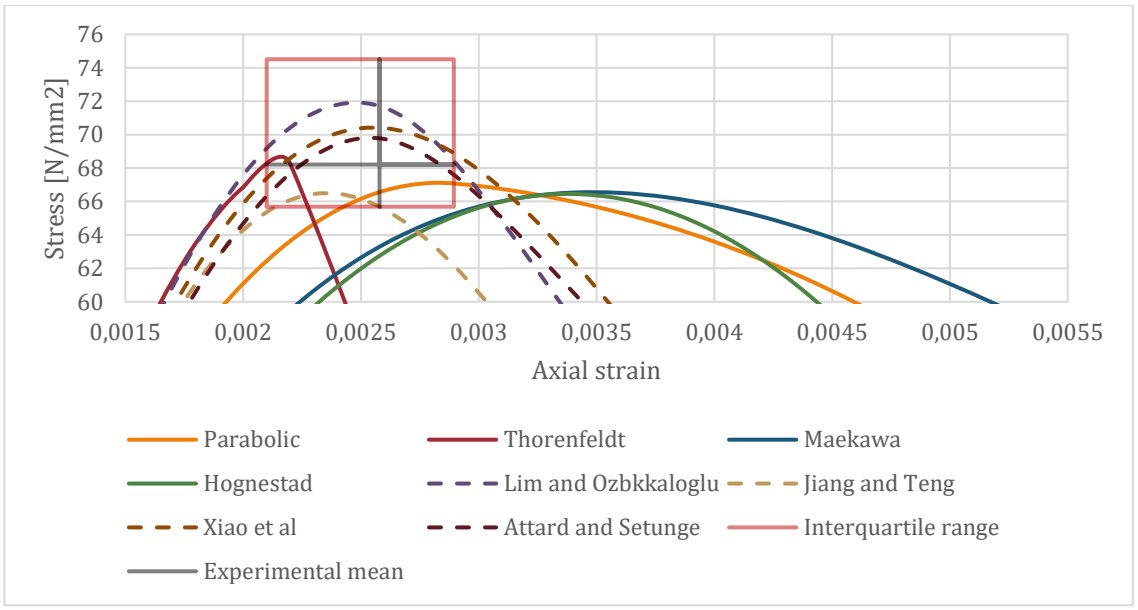

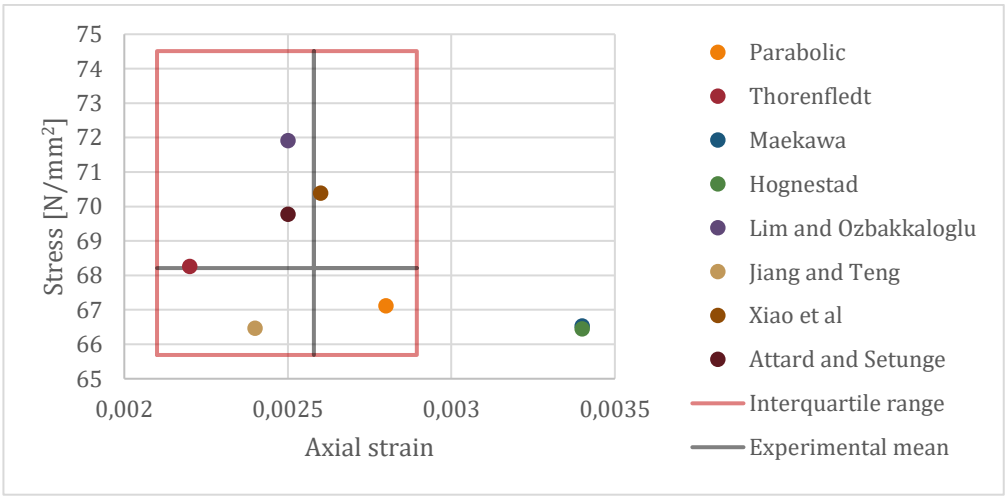

Figure 4-5: Comparison at 1.0 confinement; top, Total curves; middle, Top of the curves: bottom, Peak of the curves

4.1.4.3 Comparison with 5.0 N/mm^2 confinement

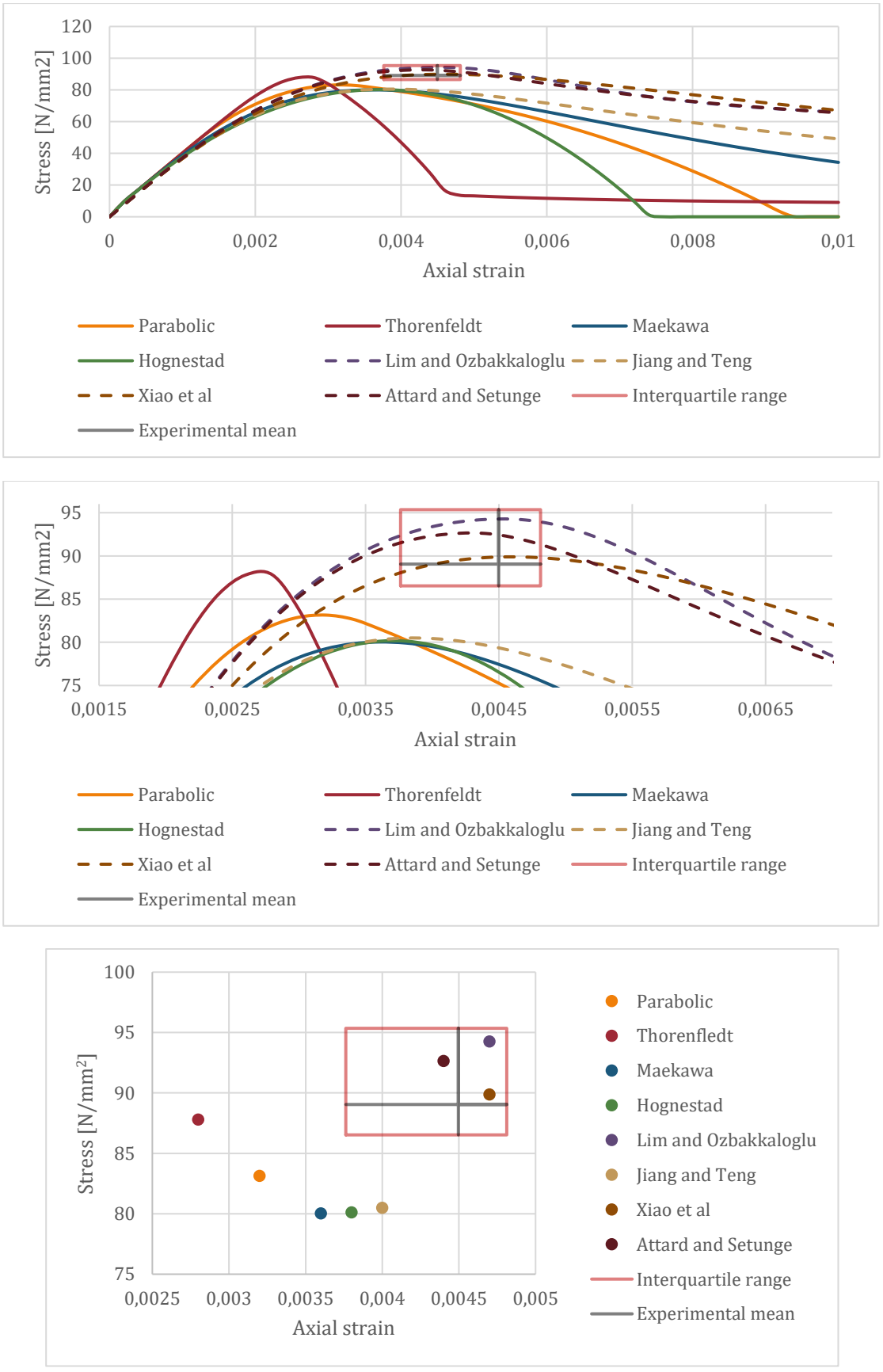

Figure 4-6: Comparison at 5.0 confinement; top, Total curves; middle, Top of the curves: bottom, Peak of the curves

4.1.4.4 Comparison with 10.0 N/mm^2 confinement

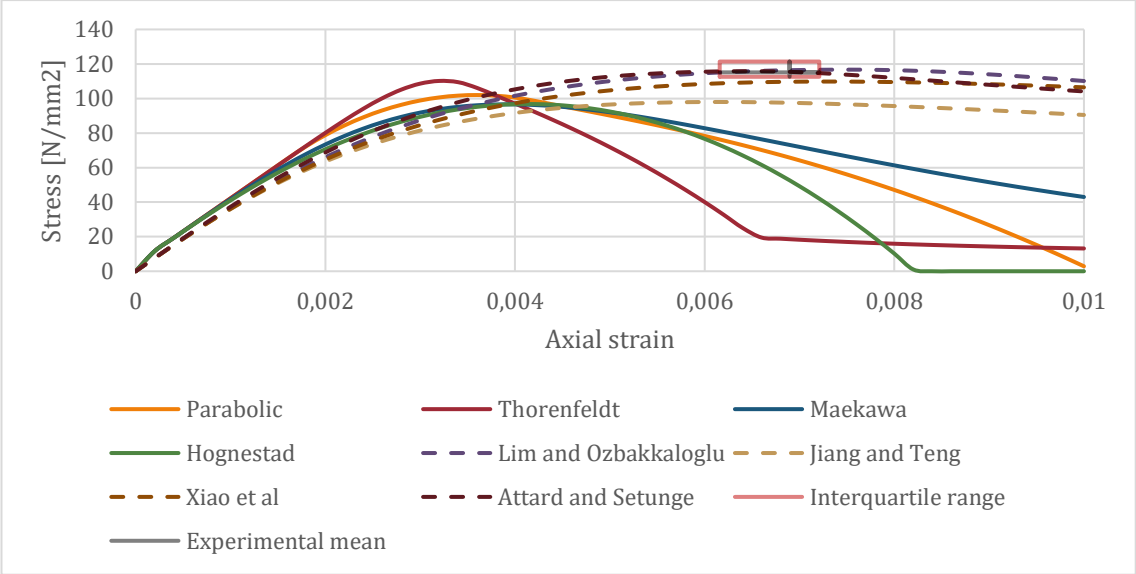

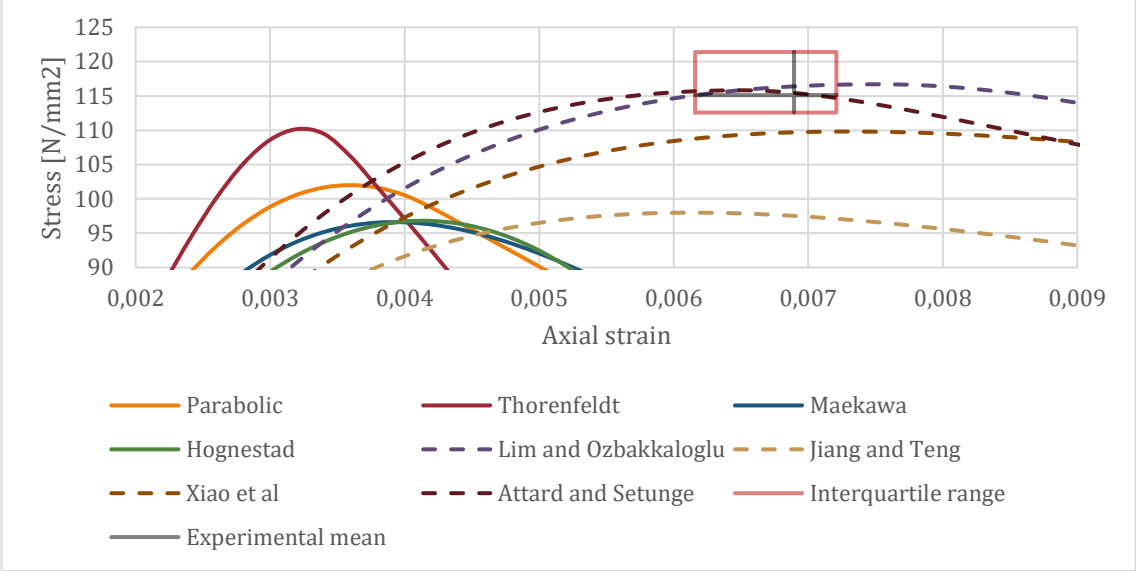

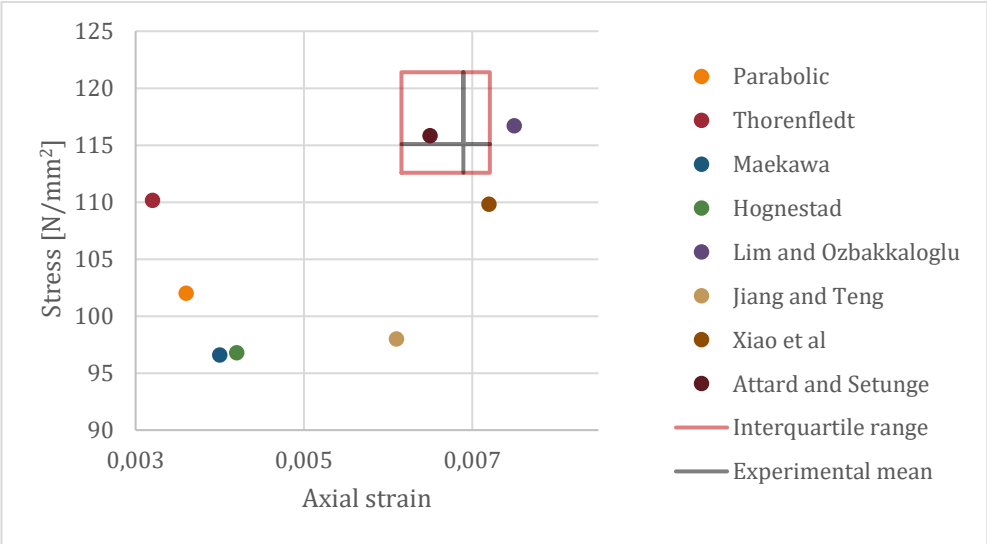

Figure 4-7: Comparison at 10.0 confinement; top, Total curves; middle, Top of the curves: bottom, Peak of the curves

4.1.4.5 Individual response on confinement

To get a clear insight in the individual response of the different compressive behaviour models on confinement the different confinement levels are plotted in the same graph for each compressive behaviour model, these are displayed in Figure 4-8.

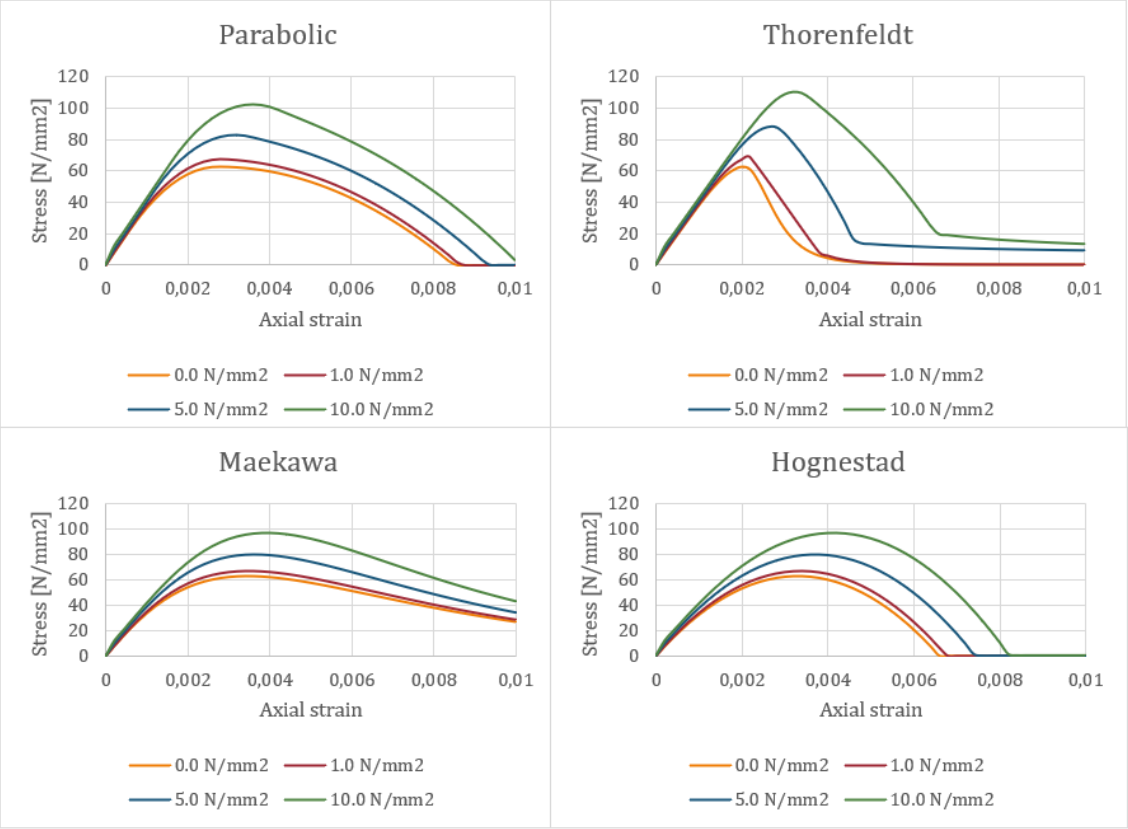

Figure 4-8: Compare of compressive behaviour models with different levels of confinement

4.1.5 Comments and remarks

To compare the compressive curves there has been a close look to three characteristic points in the stress-strain curves. The peak strength, the peak strain and the residual strength of the compressive curve. The peak strength is the maximum compressive stress in the principal axis. The peak strain is the strain at peak strength. The residual strength is represented by the trend in the stress-strain curve after the peak strength.

4.1.5.1 Peak strength

It is observed that the Thorenfledt model reacts the strongest on the applied confinement and shows the highest peak strength. The Parabolic model reacts the second strongest and the Maekawa and the Hognestad models are reacting the weakest to the confinement. For the most part all of the DIANA models demonstrate the beneficial impact that confinement has on the compressive strength, although all the peak strengths fall below the experimental mean value. No large overestimations of peak strength are made by DIANA which could resulting in unsafe calculations.

4.1.5.2 Peak strain

The strains resulting from the various DIANA models exhibit some scattering when the peak strain is observed in the absence of any confinement. This is a result from the assumptions made in the compressive behaviour models. Looking at the effect of the confinement on the peak strain it is observed that all the DIANA models show a lower peak strain than the analytical models. At the higher confinement levels the peak strain deviates a lot from the trend in the analytical models and the experimental values. The Hognestad compressive model shows the largest increase in peak strain and the closest approach to the analytical models and experimental value. Closely after the Hognestad model comes the Maekawa compressive model which results lay close together. The Thorenfeldt model shows the least peak strain increase with the different confinement levels. The parabolic model does lay in the middle of these two outers.

4.1.5.3 Residual strength

A key feature of the confined stress-strain curve is the development of larger residual strengths at larger confinement levels. Residual strength of the curve is denoted by the strength path after peak strength. Because of the compression on all the sides, the material has no way to go hence the confinement. If all the binding connections inside the material break down, there will still be a certain volume filled. This volume of material will still resist some forces, resulting in a residual strength. This residual strength is only somewhat shown in the Parabolic and Maekawa model. Only in these models the residual strength is also present without any confinement. None of the DIANA models show the development of residual strength related to confinement. They show uplift of the general curve as a result of the confinement. The Hognestad model shows the earliest complete loss of compressive strength. The Thorenfeldt model shows a residual strength of the confinement level after a steep decline after the peak strength, this is not like the residual strength shown in the analytical models. The Parabolic model lays in between the Hognestad and Maekawa models.

4.1.6 Concluding

Taking all the different factors into consideration the Parabolic model is most suitable for modelling the confinement within the discussed confinement levels. The Parabolic model shows a stable progression before and after peak strength with and without the presence of confinement. The strength increase is in between the other DIANA models but does show good response to the confinement. The difference between the Parabolic model and the analytical models comes mainly from the different approach to confinement. This is a direct approach for the analytical models making use of the confinement as a variable in the calculation. DIANA uses the scaling of the uniaxial compressive curve in the failure surface. Resulting in a strength increase factor. The difference in peak strain is resulting from the different approach in terms of calculating the peak strain. The analytical models use a direct approach and DIANA scales the strain with the strength increase factor. As the strength and strain scale not proportionate, this will result in a larger difference at higher confinement levels. This smaller amount of strain will result in a confined region in the model which reacts less ductile than the experiments demonstrated. However, does show a large strain increase compared to the non-confined areas in the model. So this lagging strain development will not have large impacts on a massive concrete structure such as a wind tower foundation.

A direct confinement approach by DIANA will result in additional compressive capacity, as it would better approach the analytical confinement curves. This would also greatly improve the development of residual strength. This could be of great interest for future research.

5 CONFINEMENT WITHIN THE CASE STUDY

In the previous chapter the ideal case of confinement is compared with analytical models and experimental values. The model used for this comparison was meshed with only one element, so the cooperation of elements would not influence the outcomes. The principal stresses are also perpendicular to the planes of the model. In a full scale model this would more often not be the case. A full scale model consist of components meshed with multiple elements. In which the principal stresses do not always follow the meshed grid. For the further investigation of confinement within a non-linear analysis an axisymmetric scale model is presented. The axisymmetric top model is a scale model of the axisymmetric model used in the linear analysis representing the area surrounding the anchor cage. This model is developed to investigate the effect of confinement added to the axisymmetric model subjected with increasing pretension stresses. So the effect of confinement on this larger top model could be investigated.

5.1 Axisymmetric top model

Because of the large areas outside of the area of interest a scale model is made with the axisymmetric model as the basis. This scale model is representing the top of the axisymmetric model. The top model is made to focus on the stress development surrounding the anchor cage and keeping the calculation time low. The part of the foundation that is modeled is displayed in Figure 5-1.

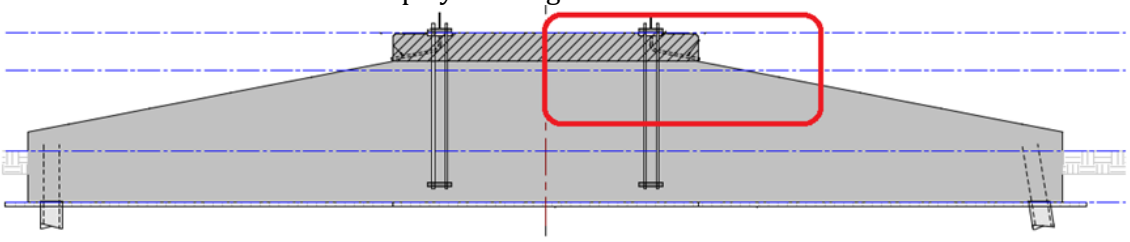

Figure 5-1: Location and dimensions of axisymmetric top model

Because the anchor plates have the same dimensions, the stresses on the top and bottom will develop in the same manner. Therefore there can be made use of the symmetry line halfway and only the top half of the area between the anchor plates is modeled. This results in a model height of 600 mm pedestal and 900 mm of the body.

The ending pedestal and inclined side of the foundation in the upper right corner of the model has little to no influence on the stresses beneath the anchor plates, because it lays outside of the influence area. The anchor plates are pressed together and the concrete only reacts to this movement.

The top model has a width of 4495 mm, the concrete body a height of 900 mm and the pedestal a height of 600 mm. The anchor plate is situated on top of the pedestal in the middle of the width. The anchor plate has a width of 505 mm and a height of 140 mm. The two supports on top of the anchor plate resemble the anchor rods which are prestressed. In the model the load is applied by a prescribed displacement at the top of the anchor plate, at the place where the anchor bolts connect with the anchor plate. The left side of the model is supported resembling the rest of the model after rotating around the Y-axis, being a axisymmetric model. At the bottom side the top model is supported resembling the symmetry axis between the two anchor plates.

The axisymmetric top model is displayed in Figure 5-2. A non-linear analysis is made of the model to capture the effect that confinement has on the increasing pre-tensioning forces. Modeled as a prescribed displacement at the top anchor plate.

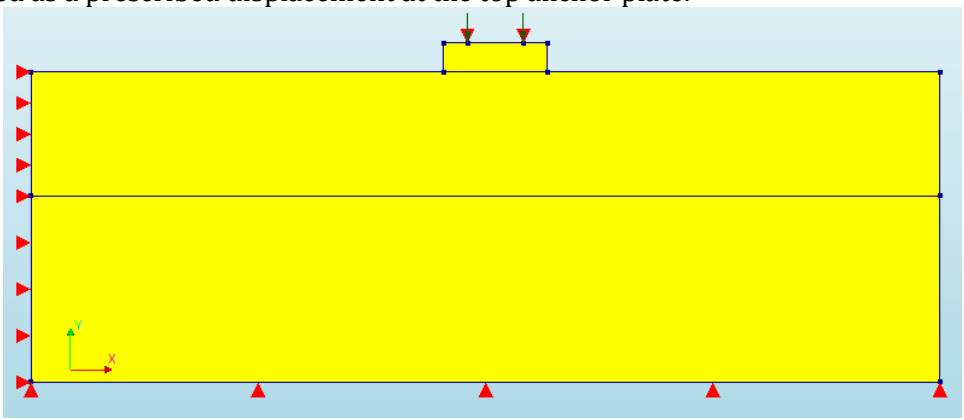

Figure 5-2: Axisymmetric top model

The parameters used for the non-linear analysis are displayed in Table 5-1. For the top anchor plate linear material properties are adopted. The pedestal is of concrete type C55/67 and the concrete body is of concrete type C30/37.

Table 5-1: Non-linear analysis parameter for the Top model

Parameter	**Unit**	**C55/67**	**C30/37**	**Steel**
Young's modulus	N/mm²	38200	32800	210000
Poisson ratio	-	0.2	0.2	0.3
Compression curve	-	Parabolic	Parabolic	-
Compressive strength	N/mm²	63	38	-
Compressive fracture energy	N/mm	24.2	21.35	-
Reduction model	-	Vecchio and Collins 1993		-
Lower bound reduction curve	-	0.4	0.4	-
Confinement model	-	Selby and Vecchio		-
Tensile curve	-	Hordijk		-
Tensile strength	N/mm²	4.34	2.89	-
Tensile fracture energy	N/mm	0.153	0.140	-
Crack bandwidth specification	-	Rots		-
Reduction model	-	Damage based		-

The displacement load in the non-linear analysis is the same as the displacement caused by the prestressing in the linear analysis. This displacement is applied with load steps of 0.2 of the total prestressing displacement and applied 45 times, so in total 9 times the displacement caused by the prestressing in the linear model.

5.2 Comparing top model with total axisymmetric model

If the modeling assumptions are correct then the axisymmetric model and the top model would give the same principal stresses if loaded to the same extent. Comparing the principal stresses resulting from the total axisymmetric model loaded with the total prestressing force, with the principal stresses of the axisymmetric top model loaded to the same displacement would than be giving the same results. The principal stresses of the linear 3D model, linear axisymmetric model and the axisymmetric top model are displayed in Figure 5-3. All the models are loaded to the same extent. The linear models by prestressing and the axisymmetric top model by a displacement. It is clearly seen that all the principal stresses follow the same trajectory. The stresses are extracted at the same location as before for the linear models, between the two anchor rods in the middle of the model.

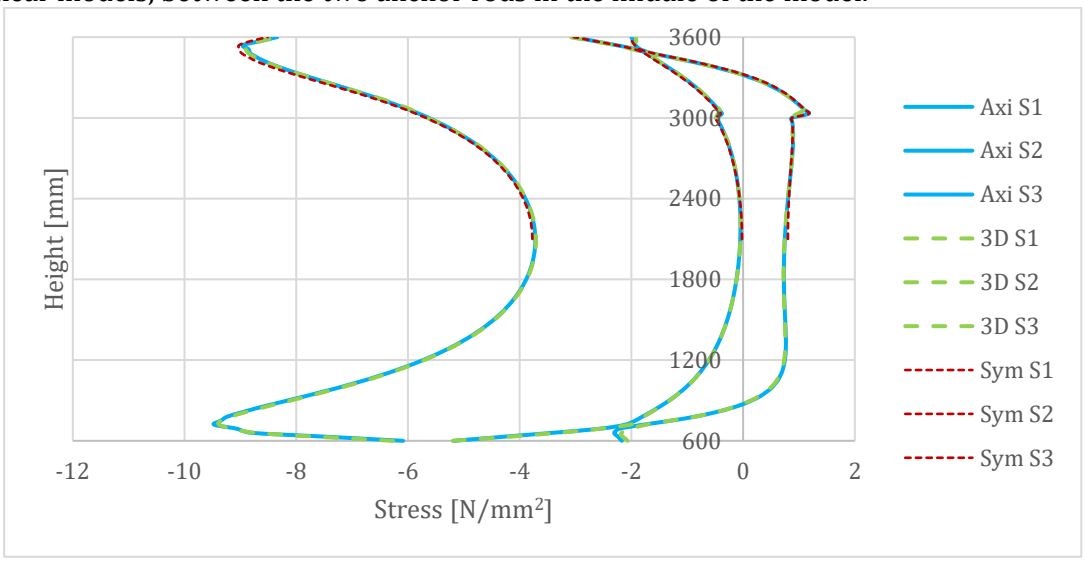

Figure 5-3: Comparison principal stresses of linear axisymmetric model, linear 3D model and the axisymmetric top model

So Figure 5-3 provides confirmation that the principal stresses in the middle of the top model are similar to those of the linear models. For the rest of the model a clear distinction can be made by coloring a positive principal stress red and a negative principal stress blue. This is done for the larges principal stress (S1) in Figure 5-4, comparing the total axisymmetric model with the top axisymmetric model. A small compressive area is shown beneath the anchor flange and at the hard of the model, this compression is the result of the partially loaded area by the anchor flange. Overall the principal stresses are nearly similar.

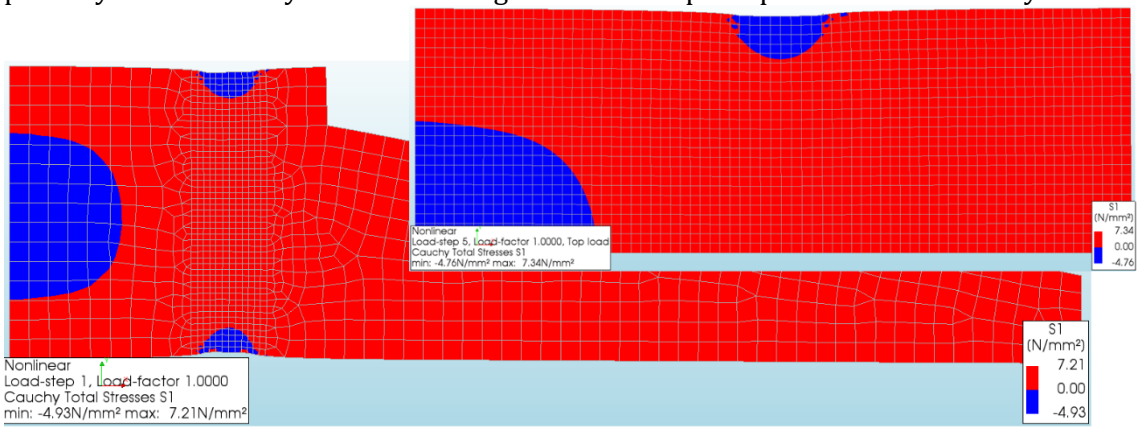

Figure 5-4: Comparison principal stress (S1), Left total axisymmetric model, Right axisymmetric top model

Looking at the comparison of the principal stresses S2 and S3 between the total axisymmetric and the axisymmetric top model the same level of agreements is shown between the different stress situations. An overview of principal stress S2 is presented in Figure 5-5. It is observed that there is compression at the hearth of the model and that some tension stressed develop at the ends of the model.

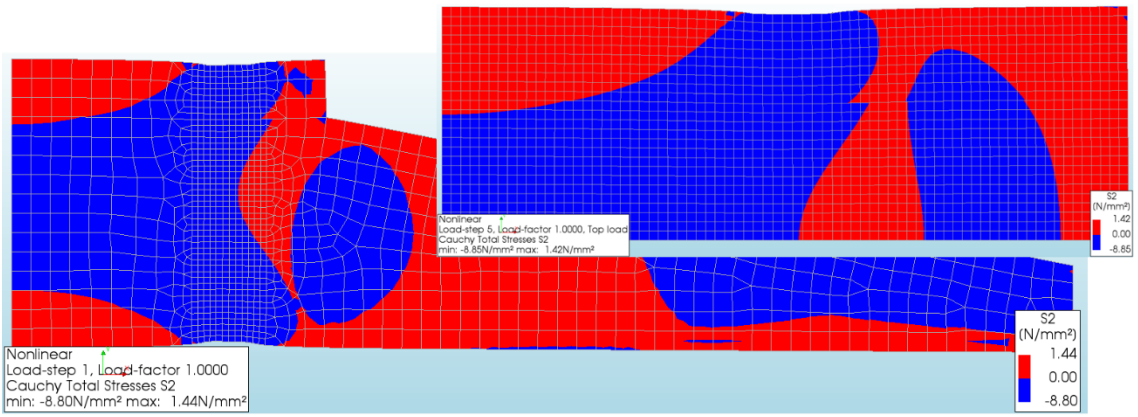

Figure 5-5: Comparison principal stress (S2), Left total axisymmetric model, Right axisymmetric top model

The comparison of the smallest principal stress (S3) is displayed in Figure 5-6. Because of the pre-tensioning almost the whole model is compressed, this results in an predominantly blue colouring of the models. In the middle of the models, the upper left corner in the figures, there is a small part of the corner being coloured in red. This tension is created by the spalling stresses resulting from the partially loaded area.

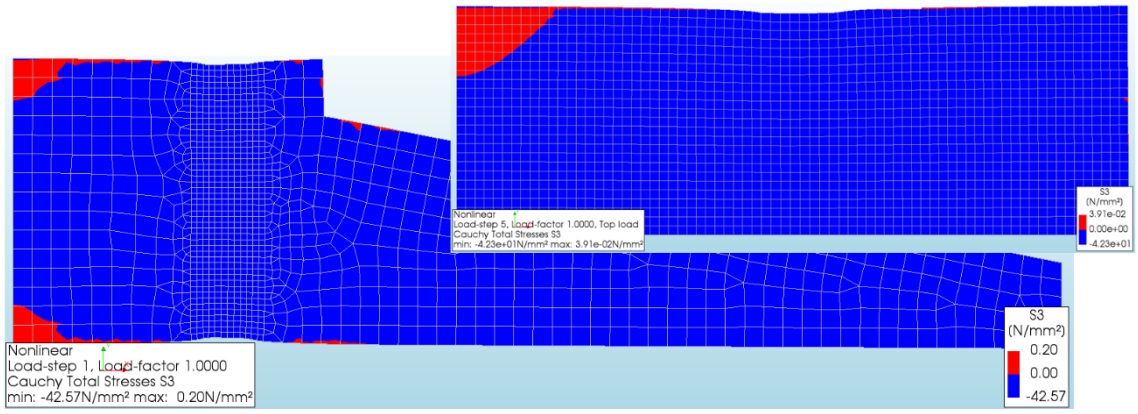

Figure 5-6: Comparison principal stress (S3), Left total axisymmetric model, Right axisymmetric top model

Because of the similarities in the principal stresses in the middle of the anchor cage, it can be concluded that the axisymmetric top model reacts in the same manner as the total axisymmetric model. Furter investigation of the principal stressed in the axisymmetric top model denotes that the principal stresses surrounding the anchor cage and in the overall model react in the same manner as the principal stresses for the total axisymmetric model. So for investigating the influence of confinement the outcomes for the Top model can be extended to the total axisymmetric model.

5.3 Effect of confinement on the Top model

To investigate the effect that confinement has on the Top model a comparison is made where the model is runed taking confinement into account and without confinement. The load is applied as described before, by means of an increasing displacement of the anchor flange. Load step 5 will result in the same load as applied by the prestressing in the linear calculations. So load step 15 equals to 3 times the prestressing load. The model is run with and without confinement by means of excluding it from the DIANA calculation. DIANA has the option to include or exclude confinement from the calculation.
By looking at the displacements of the two runs the location of the failure becomes clear. Looking at the displacements in the model without confinement it is seen that the elements directly below the anchor flange fail. The compressive strength is exceeded and the element will be crushed. Resulting in a zero displacement below the crushed element. This becomes clearly visible at load step 28, which is displayed in Figure 5-7.

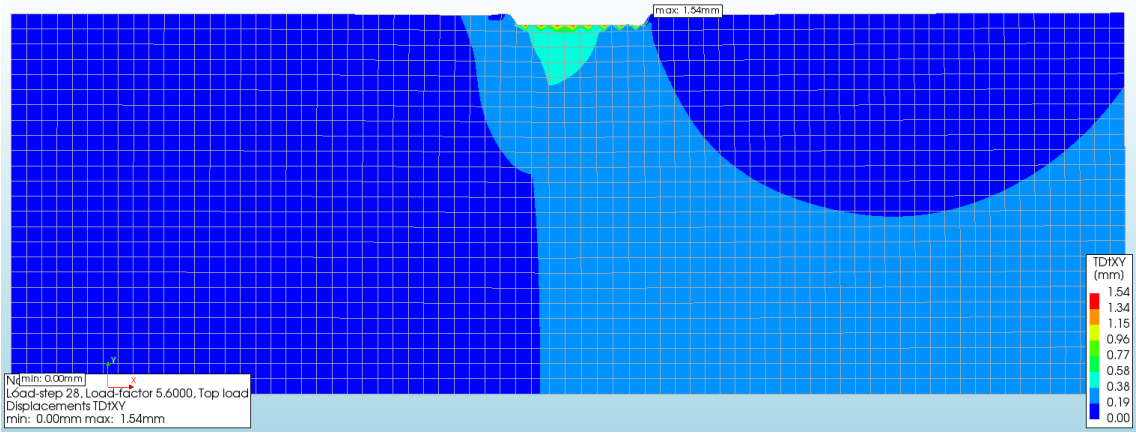

Figure 5-7: Top model without confinement, Load step 28

Looking at the displacements for load step 28 of the run with confinement included in the model, it is seen that the model is still able to resist the applied load. None of the elements fail in compression. The displacements with confinement are displayed in Figure 5-8. This is the result of the higher allowable compression stresses resulting from the confinement in the area below the anchor plate. Through including confinement the compressive stresses in the elements directly beneath the anchor flange are able to develop higher stresses than the uniaxial compressive strength.

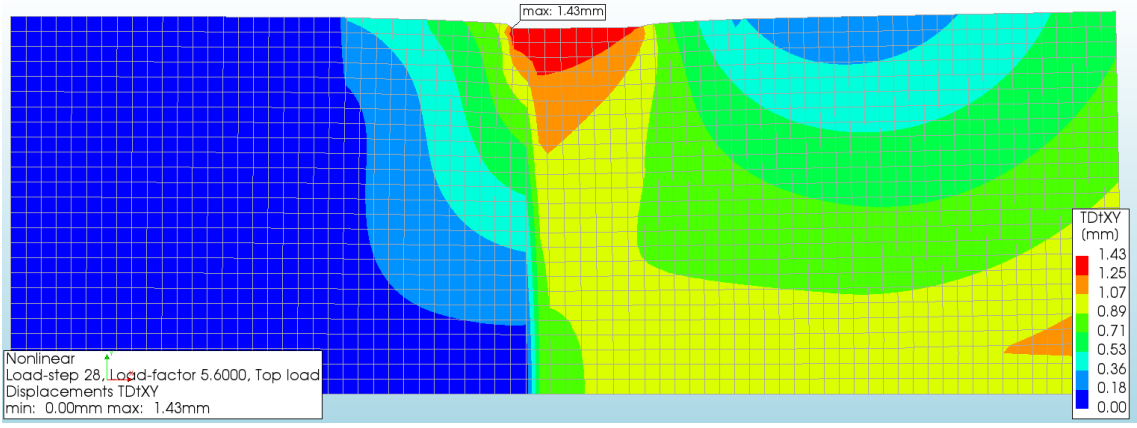

Figure 5-8: Top model with confinement, load step 28

If the displacement is further increased the model gives a clear picture if we look to the displacements at load step 36. This is displayed in Figure 5-9. It is noted that the underlying concrete of class C30/37 is crushed and that the concrete layer of the pedestal is able to withstand the compressive load.

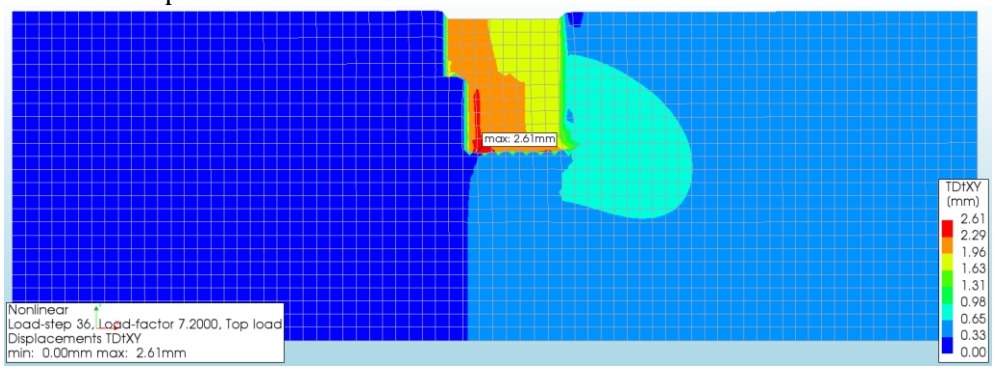

Figure 5-9: Top model with confinement, load step 36

Taking a closer look to the largest principal stress it is seen that there is a small area beneath the anchor flange that is in compression. This is displayed in Figure 5-10. If the largest principal stress is a compressive stress than the other two principal stresses will also be compressive stresses. So this small area beneath the anchor flange is in triaxial compression and confinement will increase the allowable compressive force for these elements. Therefore the elements directly below the anchor flange will not fail and the elements deeper inside of the structure will fail first, although the load is less the capacity is also less than that of the by confinement enhanced top elements.

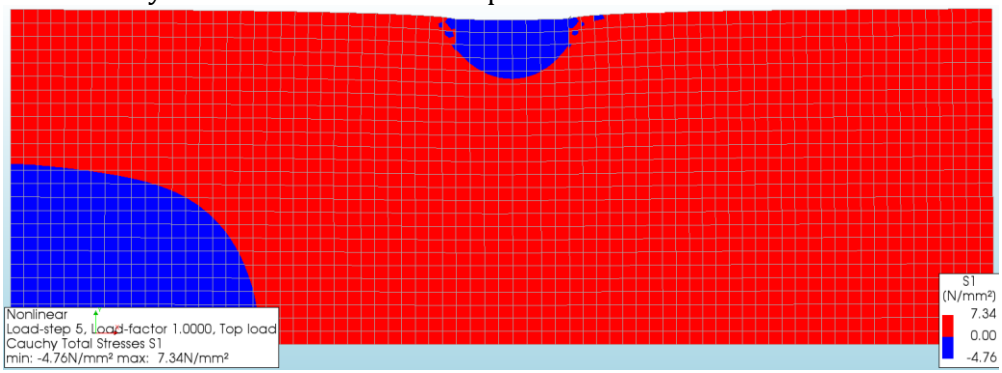

Figure 5-10: Top model principal stress S1

A large influence on the model is the crack that is formed by the bursting stresses developed by the partially loaded area that the anchor plate resembles. This crack formed at load step 15 which resembles 3 times the prestressing force applied on the anchor rods. The crack is displayed in Figure 5-11. Where cracks appear there are tensile stresses present. Where there are tensile stresses there is no triaxial compressive stress field so no confinement can develop at these places. This is seen in the top model by the initial failing of the elements closest to the crack. Once an element fails it does not press on the element next to it causing a chain reaction which leads to the presented failure modes.

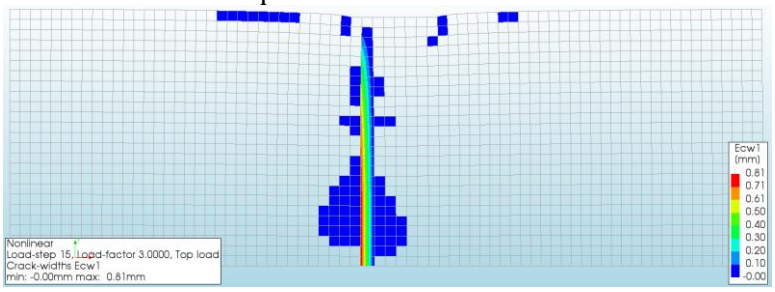

Figure 5-11: Top model crack formation

So the model without confinement fails in compression directly below the anchor flange and the model with confinement fails in compression directly below the transition in concrete strength. The difference in the location of failure becomes clear if there is looked at the load displacement diagram of the concrete node in the middle of the anchor plate and below the transition line. The placement of this element is displayed in Figure 5-12. The element is denoted with the red dot in the middle of the figure, with the arrow pointing towards it.

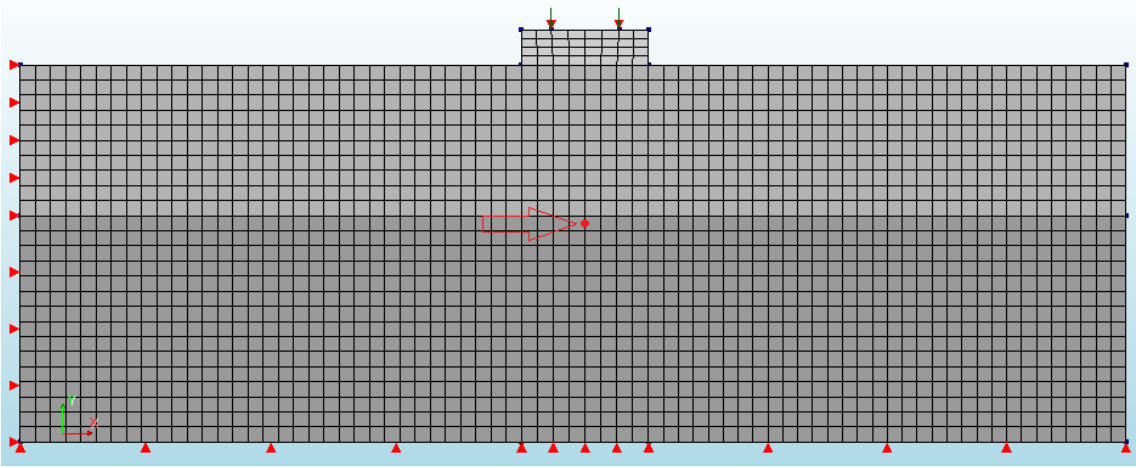

Figure 5-12: Indication of element for extracting load displacement diagram

Looking at the downwards displacement of this element plotted against the load factor Figure 5-13 is obtained. The downward displacement of this element is the result of the prescribed displacement at the top of the anchor cage. A load factor of 1 resembles one time the prestressing load. Observed is that the model without confinement fails at a load of about 5 times the prestressing load. When the element directly below the anchor flange fails the rest of the model relaxes, resulting in a zero displacement. Because of the confinement present in the model with confinement the load can increase to higher values for the top elements. This results in a later failure of the model. At a load of about 6.5 times the prestressing load the first element of the underlying concrete reaches its compressive strength and fails. This results in relaxation of the underlying elements denoted with a steep drop in displacement. So the confinement that is captured in the top part of the model is the cause for the higher admissible load and the later failure of the model.

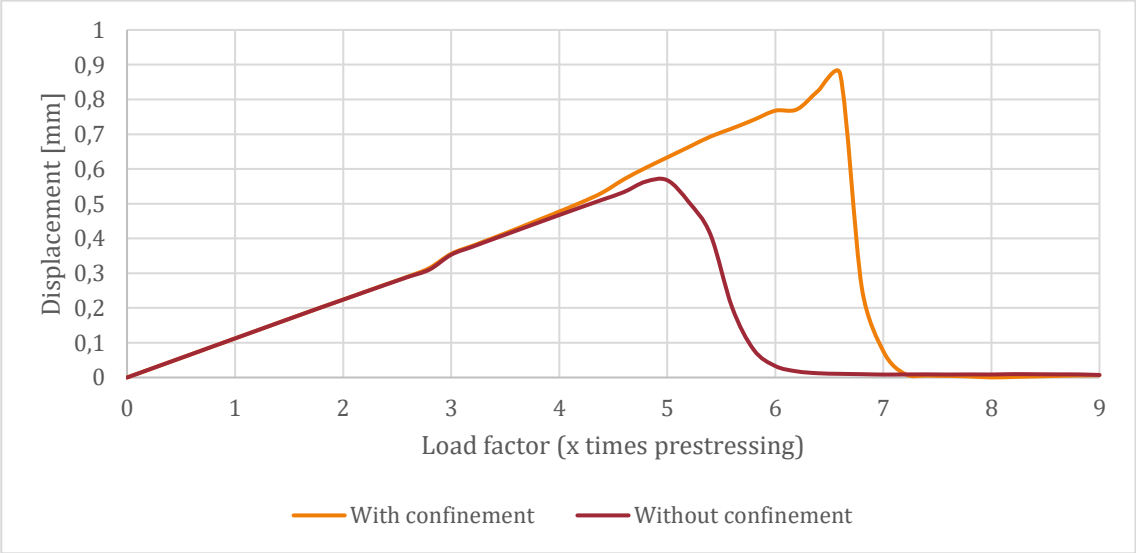

Figure 5-13: Load displacement graph of Top model

5.4 Confinement within the Top model

For the investigation if DIANA is also able to capture confinement within a larger model the outcomes of the Top model including and excluding confinement are compared. The effect of confinement becomes clear if the failure modes are compared. The model including confinement fail at a different place and at a later loading step. The different place of failure results directly from the occurring confinement. The confined elements can withstand a larger compressive force. Because of this increased compressive strength capacity, the elements also fail at a later loading step. The model including confinement can withstand 30% larger load than the model without confinement.

Seen is that confinement is present in a small area around the anchor flange. In this area not all the principal stresses line up with the grid of the meshed elements. As it was the case for the ideal case in chapter 4. The effects of confinement are clearly visible in this part of the model. So DIANA is able to detect confinement and process the enhancement resulting from it in a non ideal case.

The expansion from one to multiple elements in the approach of confinement has no effects on its outcomes. Confinement and its effects are checked for every element on its own. If all the principal stresses in the element are compressive of nature, confinement will have effect. Meaning that the uniaxial compressive curve is enhanced by the strength enhancement ratio. The cooperation of connected elements is captured by DIANA.

6 CONCLUSION

In the conclusion the answer is provided to the research question and its sub questions. The sub questions are answered before the research question. The recommendations are discussed subsequently.

6.1 Conclusion

The first sub question was:
What is confinement and how does it affect the concrete properties?
Confinement is a result of multiaxial compressive stresses, where the concrete is actively pressed together or prevented from expanding in the secondary axis. Confinement has a positive effect on the compression strength of concrete. The peak strain is also positively influenced by the confinement. The level of influence depends on the level of confinement on the concrete specimen.

The second sub question was:
Which stress states occur around the anchor cage?
The stresses resulting from the prestressing of the anchor rods results in a starting point for the foundation. After prestressing these stresses would always be present. A small area beneath the anchor flange is in multiaxial compression resulting from the partially loaded area. Looking at the stresses resulting from the prestressing and an additional moment load it is observed that the top halve of the foundation is in multiaxial compression in between the anchor rods. And that the pedestal has substantial confinement which ranges between 1 to 10 N/mm^2. Observing the unity check over the height of the foundation, comparing it with and without confinement gives a clear image on the beneficial effect that confinement has on the concretes strength. For a confinement of 10 N/mm^2 the unity check decreased from 0.95 to 0.50.

The third sub question was:
How can the occurring compressive stresses best be modelled within the stain based rotating crack model within DIANA?
To give an answer on this question the selected compressive behavior models are compared with the confinement models described in the literature and the experimental data. In general the peak strength is slightly underestimated by DIANA but overall in good agreement with the analytical models and the experimental data. The peak strain is underestimated because of the assumption that DIANA applies, namely the strain increase factor is equal to the strength increase factor. None of the DIANA models show a increasing residual strength with increased confinement. Overall the Parabolic compressive model is most suitable for modeling confinement within the wind turbine foundation, because of its peak being closest to the experimental data with and without confinement. And it has a stable progression throughout the curve.

The fourth sub question was:
What role does confinement play in a model representing the area around the anchor cage?
Concluding from the top model subjected to a increasing prestressing force it is shown that confinement influences the place and load at which the model fails. The top model was able to resist 30% more load when including confinement. So confinement plays an important role in the model, although it would only be present in a small part under the anchor flange.

The research question was stated as follows:
What is the best method for modelling confined concrete around the anchor cage in a non-linear 3D finite element method calculation so that it accurately represents real structural and material behaviour?
Summarizing from the sub questions, confinement enhances the peak compressive strength and peak strain of a concrete specimen. A small part of the concrete beneath the anchor plate is in permanent triaxial compression because of prestressing of the anchor rods. The pushing movement of the moment results in a larger area that is subjected to confinement within the wind turbine foundation. The overall confinement ranges from 0 to 10 N/mm^2 in the top half of the foundation. From the comparison of compressive behavior models with analytical models and experimental values, it is concluded that the Parabolic compressive model is best suited for modeling the compressive behavior of the elements in the wind turbine foundation. Applying the results of the one element study to a case study showed the influence that confinement had on the outcome of the analysis. Due to limitations in the analysis performed and in their interpretations, it is not possible to give an unequivocal answer based on this study. The study did show that even when the confined area is relatively small, the effect of using a correct confinement model can be great. Resulting in a 30% higher load for the Top model.

6.2 Recommendations for future work

Some recommendations have risen during the execution of this research for the further investigation of confinement within the wind turbine foundation.

The way confinement is approached by DIANA within the strain based crack model is somewhat limiting in its possibilities to resemble the analytical confinement curves. There is a work around for this problem by using the user-supplied subroutines of DIANA. For implementing a curve described by the analytical models within the total strain based crack model the whole material model has to be reworked. This would require a fair bit of time and sufficient knowledge about the DIANA background and programming skills.

During the course of this research the focus is laid on plain concrete. The implementation of reinforcements will have its effect on confinement and the confined areas inside the wind turbine foundation. Before the added reinforcements will have effect on the confinement sufficient strains need to develop in the concrete. Also the placing of reinforcement has its influence on the confinement that is generated. More research is needed on the topic to give a definitive answer on the influence reinforcements has on confinement inside the foundation.

For the case study only the prestressing load is considered. This is done to reduce the complexity and the calculation time of the model. For further investigations the influence of the moment load would be of great interest. The step to a full 3D model needs to be taken in order to apply a moment load and extract all the resulting principal stresses. The moment can not be applied on a axisymmetric model and a 2D plate model does not show the stresses in the tangential axis.

7 REFERENCES

Eurocode 2 (2005). Design of concrete structures, Part 1-1: General rules and rules for buildings. EN 1992-1-1: 2005.

Fib model code for concrete structures 2010, part 7.2.3.1.6 Confined concrete, part 7.2.3.1.7 Partially loaded, part 7.3.6 Strut and tie.

Bertacchi, P., Bellotti, R. (1972). Experimental research on deformation and failure of concrete under triaxial loads. Deformation and the Rupture of Solids Subjected to Multiaxial Stresses - part I: 'Concrete ', paper I/3; Proceedings of the International RILEM Symposium, Cannes, France, pp. 37-52.

Bongers, J. P. W. (2006). Concrete behaviour in multiaxial compression : numerical modelling. Technische Universiteit Eindhoven.

Breen, J. E., Burdet, O., Roberts, C., Sanders, D. & Wollmann, G. (1994). Anchorage zone reinforcement for post-tensioned concrete girders. National Cooperative Highway Research Program, Report No. 356. Washington, D. C., USA: National Academy Press.

Cook, R.D., Malkus. D.S., Plesha. M.E., (1988). Consepts and applications of finite element analysis. Wisconsin. Gerstle, K.H., Linse, D.L., Bertacchi, P., Kotsovos, M.D., KO, H,-Y., Newman, J.B., Rossi, P., Sschickert, G., Taylor,

M.A., Traina, L.A., Zimmerman, R.M., Bellotti, R. (1978). Strength of concrete under multiaxial stress states. Concrete and Concrete Structures (ed. B. Bresler); Proceedings of the Douglas McHenry International Symposium, Mexico City, SP 55-5, ACI, Detroit, pp. 103-131.

Hobbs, D.W. (1971). Strength of concrete under combined stress. Cement and Concrete Research, 1, pp. 41-56.

Imran, I., Pantazopoulou, S.J. (1996). Experimental study of plain concrete under triaxial stress. ACI Materials Journal, 93(6), pp. 589-601.

Iyengar, K.T.S.R., Chandrashekhara, K., Krishnaswamyh, K.T. (1965). Strength of concrete under biaxial compression. ACI Journal, 62(February), pp. 239-249.

Jamet, P., Millard, A., Nahas, G. (1984). Triaxial behaviour of a micro-concrete - complete stress-strain curves for confining pressures ranging from 0 to 100 Mpa. Concrete under Multiaxial Conditions - session 4: 'experimental results ', Vol. 1; Proceedings of RILEM-CEB Symposium, Toulouse, France, pp. 133-140.

Jiang, T., and Teng, J. G. (2007). “Analysis-oriented stress-strain models for FRP-confined concrete.” Eng. Struct., 29(11), 2968–2986

Kotsovos, M.D., Pavlović, M.N. (1995). Structural concrete, Finite-element analysis for limit- state design.

Kotsovos, M.D., Newman, J.B. (1977). Behaviour of concrete under multiaxial stress. ACI Journal, 74 (September), pp. 443-446.

Kupfer, H., Hilsdorf, H.K., Rusch, H. (1969). Behavior of concrete under biaxial stresses. ACI Journal, 66 (August), pp. 656-666.

Kupfer, H.B., Gerstle, K.H. (1973). Behavior of concrete under biaxial stresses. Journal of the Engineering Mechanics Division, ASCE, 99(EM4), pp. 853-866.

Launay, P., Gachon, H., Poitevin, P. (1970). Deformation et resistance ultime du beton sous etreinte triaxiale. Annales de l'Institut Technique du Batiment et des Travaux Publics, 269(Mai), pp. 23-48.

Leonhardt, F. & Mönnig, E. (1986). Vorlesungen über Massivbau: Teil 2: Sonderfälle der Bemessung im Stahlbetonbau (3. Auflage). Berlin Heidelberg, Germany: Springer.(in German).

Lim, J.C.; Ozbakkaloglu, (2014) T. Stress–strain model for normal-and light-weight concretes under uniaxial and triaxial compression. Constr. Build. Mater. 71, 492–509.

Lim, Jian C. and Ozbakkaloglu, Togay (2015) Lateral Strain-to-Axial Strain Relationship of Confined Concrete. Journal of Structural Engineering, 141 (5).

Liu, T.C.Y., Nilson, A.H., SLATE, F.O. (1972). Stress-strain response and fracture of concrete in uniaxial and biaxial compression. ACI Journal, 69(May), pp. 291-295.

Mander, J.B. Priestley, M,J,N. Park, R. (1988). Theoretical stress-strain model for confined concrete. Journal of structural engineering vol 114. No 8.

Mansouri, I., Gholampour, A., Kisi, O. and Ozbakkaloglu, T. (2018). “Evaluation of peak and residual conditions of actively confined concrete using neuro-fuzzy and neural computing techniques.” Neural Computing and Applications, 29(3), 873-888.

Mills, L.L., Zimmerman, R.M. (1970). Compressive strength of plain concrete under multiaxial loading conditions. ACI Journal, 67(0ctober), pp. 802-807.

Nelissen, L.J.M. (1972). Biaxial testing of normal concrete. Heron, 18(1).

Newman, J.B. (1979). Concrete under complex stress. Developments in Concrete Technology -1 (ed. F.D. Lydon), Applied Science Publishers, London, pp. 151-219.

Richart, F.E., Brandtaeg, A., Brown, R.L. (1928). A study of the failure of concrete under combined compressive stresses. Engineering experiment station, Bulletin No. 185, University of Illinois, Urbana, Illinois.

Robinson, G.S. (1967). Behavior of concrete in biaxial compression. Journal of the Structural Division, ASCE, 93(ST1), pp. 71-86.
Samani A, and Attard M, (2012)"A Stress-Strain Model for Uniaxial and Confined Concrete under Compression," Engineering Structures, vol. 41, pp. 335-349.
Shahbeyk S, Moghaddam M Z., and Safarnejad M. (2017). Faculty of Civil and Environmental Engineering, Tarbiat Modares University, Jalal Ale Ahmad Highway, P.O. Box 14115-143, Tehran, Iran
Sfer, D., Carol, I., Gettu, R., Etse, G. (2002). Study of the behavior of concrete under triaxial compression. Journal of Engineering Mechanics, ASCE, 128(2), pp. 156-163.
Song, F.,(2017) Steel fiber reinforced concrete under concentrated load, Thesis. Department of civil and environmental engineering, Ruhr university, Bochum Germany.
Smith, S.S., Willam, K.J., Gerstle, K.H., Sture, S. (1989). Concrete over the top, or: Is there life after peak? A Cl Materials Journal, 86(5), pp. 491-497.
Van Geel, H.J.G.M. (1995a). Concrete behaviour under compressive loading - Experimental research. Part I: Survey of literature. Report BK095.02, Eindhoven University of Technology, Eindhoven, The Netherlands.
Van Geel, H.J.G.M. (1995b). Concrete behaviour under compressive loading - Experimental research. Part 11: Bibliography 1900-1994. Report BK095.02, Eindhoven University of Technology, Eindhoven, The Netherlands.
Van Geel, H.J.G.M. (1998). Concrete behaviour in multiaxial compression: experimental research, PhD thesis, Eindhoven University of Technology, Eindhoven, The Netherlands.
Van Mier, J.G.M. (1984). Strain-softening of concrete under multiaxial loading conditions, PhD thesis, Eindhoven University of Technology, Eindhoven, The Netherlands.
Van Mier, J.G.M., Vonk, R.A. (1991). Fracture of concrete under multiaxial stress-recent developments. Materials and structures, RILEM, 24, pp. 61-65.
Van Mier, J.G.M., Vervuurt, A. (1997). Numerical analysis of interface fracture in concrete using a lattice-type fracture model. International Journal of Damage Mechanics, 6(0ctober), pp. 408-432.
Van Vliet, M.R.A., Van Mier, J.G.M., (1996). Experimental investigation of concrete fracture under uniaxial compression. Mechanics of Cohesive-Frictional Materials, 1, pp. 115-127.
Vonk, R.A. (1992). Softening of concrete loaded in compression, PhD thesis, Eindhoven University of Technology, Eindhoven, The Netherlands.
Xiao QG, Teng JG, Yu T. (2010) Behavior and modeling of confined high strength concrete. J Compos Constr 2010;14(3):249–59.

8 APPENDICES

1. ASSUMPTION BEDDING CONSTANT, KC 51
2. SCIA ENGINEERING RAPPORT 52
3. DATABASE ACTIVELY CONFINED CONCRETE 53

1. ASSUMPTION BEDDING CONSTANT, KC

Because of the partially loaded area the stresses in the concrete are not linear over the first part, this is called the St. Venant disturbance zone. An assumption is made to calculate the resistance of the different composed material characteristics. This is done according to the Eurocode with the theory of partially loaded areas.

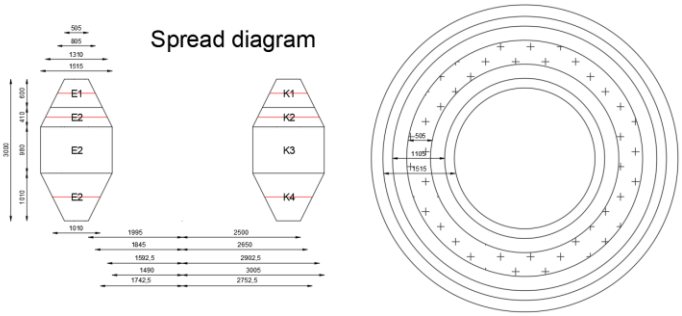

With the following properties

Description	**Symbol**	**Amount**	**Unit**
Young's modulus top, K1	E1	38200	N/mm²
Young's modulus rest, K2-4	E2	32800	N/mm²
Length K1	L1	600	mm
Length K2	L2	410	mm
Length K3	L3	980	mm
Length K4	L4	1010	mm
Surface area, flange	A_{fl}	7131337	mm²
Surface area, K1	A1	11367775	mm²
Surface area, K2	A2	18499111	mm²
Surface area, K3	A3	21394010	mm²
Surface area, K4	A4	14262674	mm²

The bedding constant per layer is calculated by

$$K_i = \frac{E_i * A_i}{L_i} \frac{N}{mm}$$

The total bedding constant is a summation of the layers

$$K_c = \frac{K_{tot}}{A_{fl}}, \qquad \text{with } \frac{1}{K_{tot}} = \sum \frac{1}{K_i}$$

This gives the following values per layer

$$K_1 = \frac{38200 * 11367775}{600} = 7.23 * 10^8 \frac{N}{mm}, \qquad \frac{1}{K_1} = \frac{1}{7.23 * 10^8} = 1.38 * 10^{-9}$$

$$K_2 = \frac{32800 * 18499111}{410} = 1.48 * 10^9 \frac{N}{mm}, \qquad \frac{1}{K_1} = \frac{1}{1.48 * 10^9} = 6.76 * 10^{-10}$$

$$K_3 = \frac{32800 * 21394010}{980} = 7.16 * 10^8 \frac{N}{mm}, \qquad \frac{1}{K_1} = \frac{1}{7.16 * 10^8} = 1.40 * 10^{-9}$$

$$K_4 = \frac{32800 * 14262674}{1010} = 4.63 * 10^8 \frac{N}{mm}, \qquad \frac{1}{K_1} = \frac{1}{4.63 * 10^8} = 2.16 * 10^{-9}$$

So this gives a K_{tot} of

$$K_{tot} = \frac{1}{\frac{1}{K_1} + \frac{1}{K_2} + \frac{1}{K_3} + \frac{1}{K_4}} = \frac{1}{1.38 * 10^{-9} + 6.76 * 10^{-10} + 1.40 * 10^{-9} + 2.16 * 10^{-9}}$$

$$= 1.78 * 10^8 \frac{N}{mm}$$

Resulting in bedding constant K_c of

$$K_c = \frac{K_{tot}}{A_{fl}} = \frac{1.78 * 10^8}{7131337} = 24.98 \frac{N}{mm^3}$$

2. SCIA ENGINEERING RAPPORT

1. Inhoudsopgave

1. Inhoudsopgave 1
2. Model gegevens 2
2.1. Model 2
2.2. 2D-elementen 2
2.3. 2D elementondersteuningen 2
2.4. Beddingen 2
2.5. Staaf nummering 3
2.6. Staven 3
2.7. Knooppunt nummering 6
2.8. Knoopondersteuningen 6
3. Belastingen 10
3.1. Belastingsgevallen 10
3.2. BG1 / Voorspanning 10
3.3. BG2 / Moment 11
3.4. Combinaties 11
4. Voorspanning 12
4.1. 3D verplaatsing 12
4.2. 3D verplaatsing; u_z 12
4.3. Contactspanningen; sigmaz Voorspanning 13
4.4. Reacties; Rz Voorspanning 13
4.5. Resultante; Rx, Ry, Rz, Mx, My, Mz Voorspanning 14
5. Voorspanning + Moment 15
5.1. 3D verplaatsing 15
5.2. 3D verplaatsing; u_z 15
5.3. Contactspanningen; sigmaz Voorspanning + Moment 16
5.4. Reacties; Rz Voorspanning + Moment 16
5.5. Resultante; Rx, Ry, Rz, Mx, My, Mz Voorspanning + Moment 17

2. Model gegevens

2.1. Model

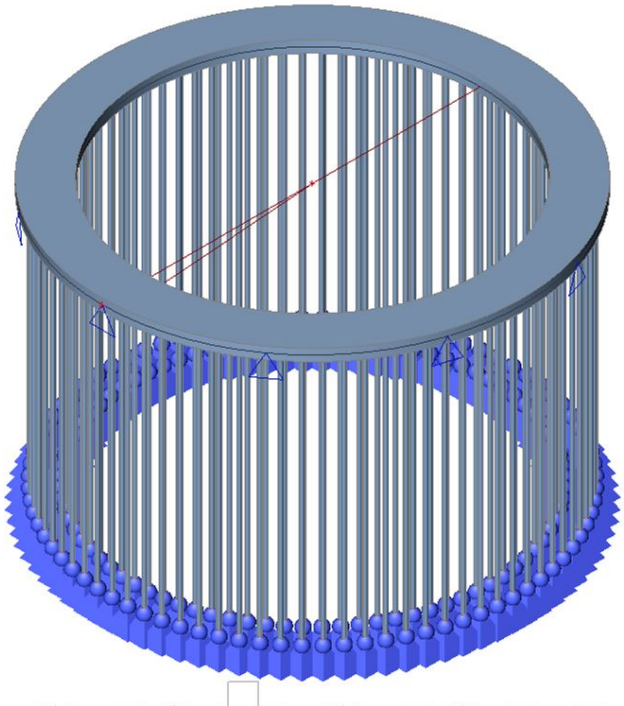

2.2. 2D-elementen

Naam	Laag	Type	Element type	Materiaal	Dikte type	D. [mm]
E1	Laag1	vloer (90)	Standaard	S 355	constant	140,000

2.3. 2D elementondersteuningen

Naam	Type	Bedding	2D-element
ondersteuning	Individueel	Bedding1	E1

2.4. Beddingen

Naam	C1x [N/mm³]	C1z	C1y [N/mm³]	Stijfheid [N/mm³]	C2x [N/mm]	C2y [N/mm]
Bedding1	0,0500	Verend	0,0500	24,9800	30000,0000	30000,0000

2.5. Staaf nummering

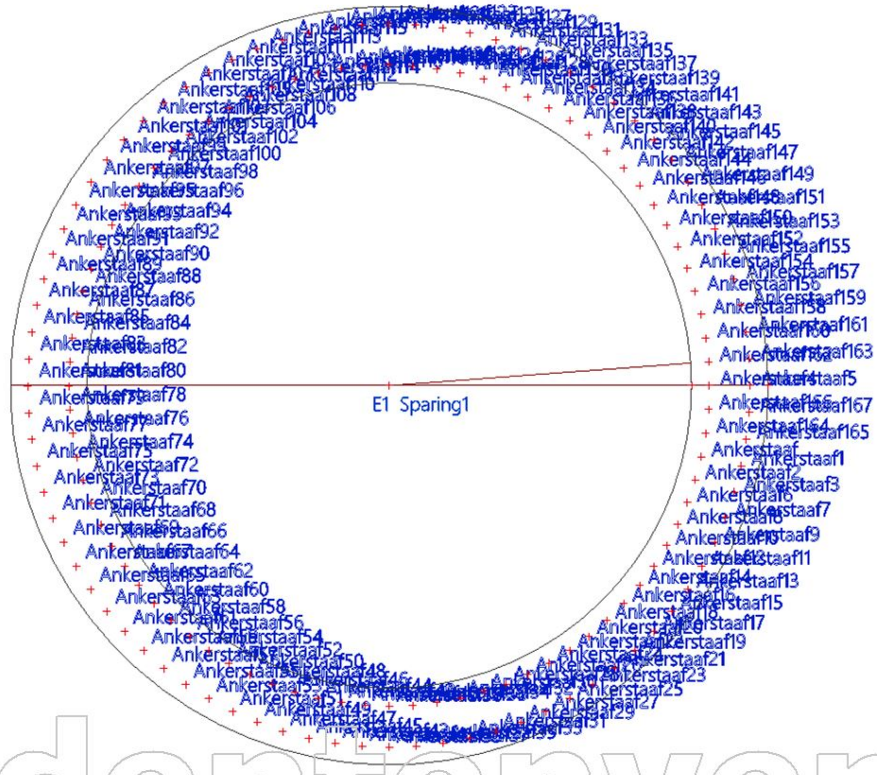

2.6. Staven

Naam	Doorsnede	Materiaal	Lengte [mm]	Beginknoop	Eindknoop	Type
Ankerstaaf	CS3 - Cirkel (44,200)	S 235	3000,000	K339	K340	Balk (80)
Ankerstaaf1	CS3 - Cirkel (44,200)	S 235	3000,000	K337	K338	Balk (80)
Ankerstaaf2	CS3 - Cirkel (44,200)	S 235	3000,000	K343	K344	Balk (80)
Ankerstaaf3	CS3 - Cirkel (44,200)	S 235	3000,000	K341	K342	Balk (80)
Ankerstaaf4	CS3 - Cirkel (44,200)	S 235	3000,000	K12	K13	Balk (80)
Ankerstaaf5	CS3 - Cirkel (44,200)	S 235	3000,000	K14	K15	Balk (80)
Ankerstaaf6	CS3 - Cirkel (44,200)	S 235	3000,000	K347	K348	Balk (80)
Ankerstaaf7	CS3 - Cirkel (44,200)	S 235	3000,000	K345	K346	Balk (80)
Ankerstaaf8	CS3 - Cirkel (44,200)	S 235	3000,000	K351	K352	Balk (80)
Ankerstaaf9	CS3 - Cirkel (44,200)	S 235	3000,000	K349	K350	Balk (80)
Ankerstaaf10	CS3 - Cirkel (44,200)	S 235	3000,000	K355	K356	Balk (80)
Ankerstaaf11	CS3 - Cirkel (44,200)	S 235	3000,000	K353	K354	Balk (80)
Ankerstaaf12	CS3 - Cirkel (44,200)	S 235	3000,000	K359	K360	Balk (80)
Ankerstaaf13	CS3 - Cirkel (44,200)	S 235	3000,000	K357	K358	Balk (80)
Ankerstaaf14	CS3 - Cirkel (44,200)	S 235	3000,000	K363	K364	Balk (80)
Ankerstaaf15	CS3 - Cirkel (44,200)	S 235	3000,000	K361	K362	Balk (80)
Ankerstaaf16	CS3 - Cirkel (44,200)	S 235	3000,000	K8	K9	Balk (80)
Ankerstaaf17	CS3 - Cirkel (44,200)	S 235	3000,000	K6	K7	Balk (80)
Ankerstaaf18	CS3 - Cirkel (44,200)	S 235	3000,000	K40	K41	Balk (80)
Ankerstaaf19	CS3 - Cirkel (44,200)	S 235	3000,000	K42	K43	Balk (80)
Ankerstaaf20	CS3 - Cirkel (44,200)	S 235	3000,000	K44	K45	Balk (80)
Ankerstaaf21	CS3 - Cirkel (44,200)	S 235	3000,000	K46	K47	Balk (80)
Ankerstaaf22	CS3 - Cirkel (44,200)	S 235	3000,000	K48	K49	Balk (80)
Ankerstaaf23	CS3 - Cirkel (44,200)	S 235	3000,000	K50	K51	Balk (80)
Ankerstaaf24	CS3 - Cirkel (44,200)	S 235	3000,000	K52	K53	Balk (80)
Ankerstaaf25	CS3 - Cirkel (44,200)	S 235	3000,000	K54	K55	Balk (80)
Ankerstaaf26	CS3 - Cirkel (44,200)	S 235	3000,000	K56	K57	Balk (80)
Ankerstaaf27	CS3 - Cirkel (44,200)	S 235	3000,000	K58	K59	Balk (80)
Ankerstaaf28	CS3 - Cirkel (44,200)	S 235	3000,000	K60	K61	Balk (80)

Naam	Doorsnede	Materiaal	Lengte [mm]	Beginknoop	Eindknoop	Type
Ankerstaaf29	CS3 - Cirkel (44,200)	S 235	3000,000	K62	K320	Balk (80)
Ankerstaaf30	CS3 - Cirkel (44,200)	S 235	3000,000	K64	K65	Balk (80)
Ankerstaaf31	CS3 - Cirkel (44,200)	S 235	3000,000	K66	K63	Balk (80)
Ankerstaaf32	CS3 - Cirkel (44,200)	S 235	3000,000	K68	K69	Balk (80)
Ankerstaaf33	CS3 - Cirkel (44,200)	S 235	3000,000	K70	K71	Balk (80)
Ankerstaaf34	CS3 - Cirkel (44,200)	S 235	3000,000	K72	K73	Balk (80)
Ankerstaaf35	CS3 - Cirkel (44,200)	S 235	3000,000	K74	K75	Balk (80)
Ankerstaaf36	CS3 - Cirkel (44,200)	S 235	3000,000	K76	K77	Balk (80)
Ankerstaaf37	CS3 - Cirkel (44,200)	S 235	3000,000	K78	K79	Balk (80)
Ankerstaaf38	CS3 - Cirkel (44,200)	S 235	3000,000	K80	K81	Balk (80)
Ankerstaaf39	CS3 - Cirkel (44,200)	S 235	3000,000	K82	K83	Balk (80)
Ankerstaaf40	CS3 - Cirkel (44,200)	S 235	3000,000	K84	K85	Balk (80)
Ankerstaaf41	CS3 - Cirkel (44,200)	S 235	3000,000	K86	K87	Balk (80)
Ankerstaaf42	CS3 - Cirkel (44,200)	S 235	3000,000	K88	K89	Balk (80)
Ankerstaaf43	CS3 - Cirkel (44,200)	S 235	3000,000	K90	K91	Balk (80)
Ankerstaaf44	CS3 - Cirkel (44,200)	S 235	3000,000	K92	K93	Balk (80)
Ankerstaaf45	CS3 - Cirkel (44,200)	S 235	3000,000	K94	K95	Balk (80)
Ankerstaaf46	CS3 - Cirkel (44,200)	S 235	3000,000	K96	K97	Balk (80)
Ankerstaaf47	CS3 - Cirkel (44,200)	S 235	3000,000	K98	K99	Balk (80)
Ankerstaaf48	CS3 - Cirkel (44,200)	S 235	3000,000	K100	K101	Balk (80)
Ankerstaaf49	CS3 - Cirkel (44,200)	S 235	3000,000	K102	K103	Balk (80)
Ankerstaaf50	CS3 - Cirkel (44,200)	S 235	3000,000	K104	K105	Balk (80)
Ankerstaaf51	CS3 - Cirkel (44,200)	S 235	3000,000	K106	K107	Balk (80)
Ankerstaaf52	CS3 - Cirkel (44,200)	S 235	3000,000	K108	K109	Balk (80)
Ankerstaaf53	CS3 - Cirkel (44,200)	S 235	3000,000	K110	K111	Balk (80)
Ankerstaaf54	CS3 - Cirkel (44,200)	S 235	3000,000	K112	K113	Balk (80)
Ankerstaaf55	CS3 - Cirkel (44,200)	S 235	3000,000	K114	K115	Balk (80)
Ankerstaaf56	CS3 - Cirkel (44,200)	S 235	3000,000	K116	K117	Balk (80)
Ankerstaaf57	CS3 - Cirkel (44,200)	S 235	3000,000	K118	K119	Balk (80)
Ankerstaaf58	CS3 - Cirkel (44,200)	S 235	3000,000	K120	K121	Balk (80)
Ankerstaaf59	CS3 - Cirkel (44,200)	S 235	3000,000	K122	K123	Balk (80)
Ankerstaaf60	CS3 - Cirkel (44,200)	S 235	3000,000	K124	K125	Balk (80)
Ankerstaaf61	CS3 - Cirkel (44,200)	S 235	3000,000	K126	K127	Balk (80)
Ankerstaaf62	CS3 - Cirkel (44,200)	S 235	3000,000	K128	K129	Balk (80)
Ankerstaaf63	CS3 - Cirkel (44,200)	S 235	3000,000	K130	K131	Balk (80)
Ankerstaaf64	CS3 - Cirkel (44,200)	S 235	3000,000	K132	K133	Balk (80)
Ankerstaaf65	CS3 - Cirkel (44,200)	S 235	3000,000	K134	K135	Balk (80)
Ankerstaaf66	CS3 - Cirkel (44,200)	S 235	3000,000	K136	K137	Balk (80)
Ankerstaaf67	CS3 - Cirkel (44,200)	S 235	3000,000	K138	K139	Balk (80)
Ankerstaaf68	CS3 - Cirkel (44,200)	S 235	3000,000	K140	K141	Balk (80)
Ankerstaaf69	CS3 - Cirkel (44,200)	S 235	3000,000	K142	K143	Balk (80)
Ankerstaaf70	CS3 - Cirkel (44,200)	S 235	3000,000	K144	K145	Balk (80)
Ankerstaaf71	CS3 - Cirkel (44,200)	S 235	3000,000	K146	K147	Balk (80)
Ankerstaaf72	CS3 - Cirkel (44,200)	S 235	3000,000	K148	K149	Balk (80)
Ankerstaaf73	CS3 - Cirkel (44,200)	S 235	3000,000	K150	K151	Balk (80)
Ankerstaaf74	CS3 - Cirkel (44,200)	S 235	3000,000	K152	K153	Balk (80)
Ankerstaaf75	CS3 - Cirkel (44,200)	S 235	3000,000	K154	K155	Balk (80)
Ankerstaaf76	CS3 - Cirkel (44,200)	S 235	3000,000	K156	K157	Balk (80)
Ankerstaaf77	CS3 - Cirkel (44,200)	S 235	3000,000	K158	K159	Balk (80)
Ankerstaaf78	CS3 - Cirkel (44,200)	S 235	3000,000	K160	K161	Balk (80)
Ankerstaaf79	CS3 - Cirkel (44,200)	S 235	3000,000	K162	K163	Balk (80)
Ankerstaaf80	CS3 - Cirkel (44,200)	S 235	3000,000	K164	K165	Balk (80)
Ankerstaaf81	CS3 - Cirkel (44,200)	S 235	3000,000	K166	K167	Balk (80)
Ankerstaaf82	CS3 - Cirkel (44,200)	S 235	3000,000	K168	K169	Balk (80)
Ankerstaaf83	CS3 - Cirkel (44,200)	S 235	3000,000	K170	K171	Balk (80)
Ankerstaaf84	CS3 - Cirkel (44,200)	S 235	3000,000	K172	K173	Balk (80)
Ankerstaaf85	CS3 - Cirkel (44,200)	S 235	3000,000	K174	K175	Balk (80)
Ankerstaaf86	CS3 - Cirkel (44,200)	S 235	3000,000	K176	K177	Balk (80)
Ankerstaaf87	CS3 - Cirkel (44,200)	S 235	3000,000	K178	K179	Balk (80)
Ankerstaaf88	CS3 - Cirkel (44,200)	S 235	3000,000	K180	K181	Balk (80)
Ankerstaaf89	CS3 - Cirkel (44,200)	S 235	3000,000	K182	K183	Balk (80)
Ankerstaaf90	CS3 - Cirkel (44,200)	S 235	3000,000	K184	K185	Balk (80)
Ankerstaaf91	CS3 - Cirkel (44,200)	S 235	3000,000	K186	K187	Balk (80)
Ankerstaaf92	CS3 - Cirkel (44,200)	S 235	3000,000	K188	K189	Balk (80)
Ankerstaaf93	CS3 - Cirkel (44,200)	S 235	3000,000	K190	K191	Balk (80)
Ankerstaaf94	CS3 - Cirkel (44,200)	S 235	3000,000	K192	K193	Balk (80)

Naam	Doorsnede	Materiaal	Lengte [mm]	Beginknoop	Eindknoop	Type
Ankerstaaf95	CS3 - Cirkel (44,200)	S 235	3000,000	K194	K195	Balk (80)
Ankerstaaf96	CS3 - Cirkel (44,200)	S 235	3000,000	K196	K197	Balk (80)
Ankerstaaf97	CS3 - Cirkel (44,200)	S 235	3000,000	K198	K199	Balk (80)
Ankerstaaf98	CS3 - Cirkel (44,200)	S 235	3000,000	K200	K201	Balk (80)
Ankerstaaf99	CS3 - Cirkel (44,200)	S 235	3000,000	K202	K203	Balk (80)
Ankerstaaf100	CS3 - Cirkel (44,200)	S 235	3000,000	K204	K205	Balk (80)
Ankerstaaf101	CS3 - Cirkel (44,200)	S 235	3000,000	K206	K207	Balk (80)
Ankerstaaf102	CS3 - Cirkel (44,200)	S 235	3000,000	K208	K209	Balk (80)
Ankerstaaf103	CS3 - Cirkel (44,200)	S 235	3000,000	K210	K211	Balk (80)
Ankerstaaf104	CS3 - Cirkel (44,200)	S 235	3000,000	K212	K213	Balk (80)
Ankerstaaf105	CS3 - Cirkel (44,200)	S 235	3000,000	K214	K215	Balk (80)
Ankerstaaf106	CS3 - Cirkel (44,200)	S 235	3000,000	K216	K217	Balk (80)
Ankerstaaf107	CS3 - Cirkel (44,200)	S 235	3000,000	K218	K219	Balk (80)
Ankerstaaf108	CS3 - Cirkel (44,200)	S 235	3000,000	K220	K221	Balk (80)
Ankerstaaf109	CS3 - Cirkel (44,200)	S 235	3000,000	K222	K223	Balk (80)
Ankerstaaf110	CS3 - Cirkel (44,200)	S 235	3000,000	K224	K225	Balk (80)
Ankerstaaf111	CS3 - Cirkel (44,200)	S 235	3000,000	K226	K227	Balk (80)
Ankerstaaf112	CS3 - Cirkel (44,200)	S 235	3000,000	K228	K229	Balk (80)
Ankerstaaf113	CS3 - Cirkel (44,200)	S 235	3000,000	K230	K231	Balk (80)
Ankerstaaf114	CS3 - Cirkel (44,200)	S 235	3000,000	K232	K233	Balk (80)
Ankerstaaf115	CS3 - Cirkel (44,200)	S 235	3000,000	K234	K235	Balk (80)
Ankerstaaf116	CS3 - Cirkel (44,200)	S 235	3000,000	K236	K237	Balk (80)
Ankerstaaf117	CS3 - Cirkel (44,200)	S 235	3000,000	K238	K239	Balk (80)
Ankerstaaf118	CS3 - Cirkel (44,200)	S 235	3000,000	K240	K241	Balk (80)
Ankerstaaf119	CS3 - Cirkel (44,200)	S 235	3000,000	K242	K243	Balk (80)
Ankerstaaf120	CS3 - Cirkel (44,200)	S 235	3000,000	K244	K245	Balk (80)
Ankerstaaf121	CS3 - Cirkel (44,200)	S 235	3000,000	K246	K247	Balk (80)
Ankerstaaf122	CS3 - Cirkel (44,200)	S 235	3000,000	K248	K249	Balk (80)
Ankerstaaf123	CS3 - Cirkel (44,200)	S 235	3000,000	K250	K251	Balk (80)
Ankerstaaf124	CS3 - Cirkel (44,200)	S 235	3000,000	K252	K253	Balk (80)
Ankerstaaf125	CS3 - Cirkel (44,200)	S 235	3000,000	K254	K255	Balk (80)
Ankerstaaf126	CS3 - Cirkel (44,200)	S 235	3000,000	K256	K257	Balk (80)
Ankerstaaf127	CS3 - Cirkel (44,200)	S 235	3000,000	K258	K259	Balk (80)
Ankerstaaf128	CS3 - Cirkel (44,200)	S 235	3000,000	K260	K261	Balk (80)
Ankerstaaf129	CS3 - Cirkel (44,200)	S 235	3000,000	K262	K263	Balk (80)
Ankerstaaf130	CS3 - Cirkel (44,200)	S 235	3000,000	K264	K265	Balk (80)
Ankerstaaf131	CS3 - Cirkel (44,200)	S 235	3000,000	K266	K267	Balk (80)
Ankerstaaf132	CS3 - Cirkel (44,200)	S 235	3000,000	K268	K269	Balk (80)
Ankerstaaf133	CS3 - Cirkel (44,200)	S 235	3000,000	K270	K271	Balk (80)
Ankerstaaf134	CS3 - Cirkel (44,200)	S 235	3000,000	K272	K273	Balk (80)
Ankerstaaf135	CS3 - Cirkel (44,200)	S 235	3000,000	K274	K275	Balk (80)
Ankerstaaf136	CS3 - Cirkel (44,200)	S 235	3000,000	K276	K277	Balk (80)
Ankerstaaf137	CS3 - Cirkel (44,200)	S 235	3000,000	K278	K279	Balk (80)
Ankerstaaf138	CS3 - Cirkel (44,200)	S 235	3000,000	K280	K281	Balk (80)
Ankerstaaf139	CS3 - Cirkel (44,200)	S 235	3000,000	K282	K283	Balk (80)
Ankerstaaf140	CS3 - Cirkel (44,200)	S 235	3000,000	K284	K285	Balk (80)
Ankerstaaf141	CS3 - Cirkel (44,200)	S 235	3000,000	K286	K287	Balk (80)
Ankerstaaf142	CS3 - Cirkel (44,200)	S 235	3000,000	K288	K289	Balk (80)
Ankerstaaf143	CS3 - Cirkel (44,200)	S 235	3000,000	K290	K291	Balk (80)
Ankerstaaf144	CS3 - Cirkel (44,200)	S 235	3000,000	K292	K293	Balk (80)
Ankerstaaf145	CS3 - Cirkel (44,200)	S 235	3000,000	K294	K295	Balk (80)
Ankerstaaf146	CS3 - Cirkel (44,200)	S 235	3000,000	K296	K297	Balk (80)
Ankerstaaf147	CS3 - Cirkel (44,200)	S 235	3000,000	K298	K299	Balk (80)
Ankerstaaf148	CS3 - Cirkel (44,200)	S 235	3000,000	K300	K301	Balk (80)
Ankerstaaf149	CS3 - Cirkel (44,200)	S 235	3000,000	K302	K303	Balk (80)
Ankerstaaf150	CS3 - Cirkel (44,200)	S 235	3000,000	K304	K305	Balk (80)
Ankerstaaf151	CS3 - Cirkel (44,200)	S 235	3000,000	K306	K307	Balk (80)
Ankerstaaf152	CS3 - Cirkel (44,200)	S 235	3000,000	K308	K309	Balk (80)
Ankerstaaf153	CS3 - Cirkel (44,200)	S 235	3000,000	K310	K311	Balk (80)
Ankerstaaf154	CS3 - Cirkel (44,200)	S 235	3000,000	K312	K313	Balk (80)
Ankerstaaf155	CS3 - Cirkel (44,200)	S 235	3000,000	K314	K315	Balk (80)
Ankerstaaf156	CS3 - Cirkel (44,200)	S 235	3000,000	K316	K317	Balk (80)
Ankerstaaf157	CS3 - Cirkel (44,200)	S 235	3000,000	K318	K319	Balk (80)
Ankerstaaf158	CS3 - Cirkel (44,200)	S 235	3000,000	K321	K322	Balk (80)
Ankerstaaf159	CS3 - Cirkel (44,200)	S 235	3000,000	K323	K324	Balk (80)
Ankerstaaf160	CS3 - Cirkel (44,200)	S 235	3000,000	K325	K326	Balk (80)

Naam	Doorsnede	Materiaal	Lengte [mm]	Beginknoop	Eindknoop	Type
Ankerstaaf161	CS3 - Cirkel (44,200)	S 235	3000,000	K327	K328	Balk (80)
Ankerstaaf162	CS3 - Cirkel (44,200)	S 235	3000,000	K329	K330	Balk (80)
Ankerstaaf163	CS3 - Cirkel (44,200)	S 235	3000,000	K331	K332	Balk (80)
Ankerstaaf164	CS3 - Cirkel (44,200)	S 235	3000,000	K333	K334	Balk (80)
Ankerstaaf165	CS3 - Cirkel (44,200)	S 235	3000,000	K335	K336	Balk (80)
Ankerstaaf166	CS3 - Cirkel (44,200)	S 235	3000,000	K365	K366	Balk (80)
Ankerstaaf167	CS3 - Cirkel (44,200)	S 235	3000,000	K367	K368	Balk (80)

2.7. Knooppunt nummering

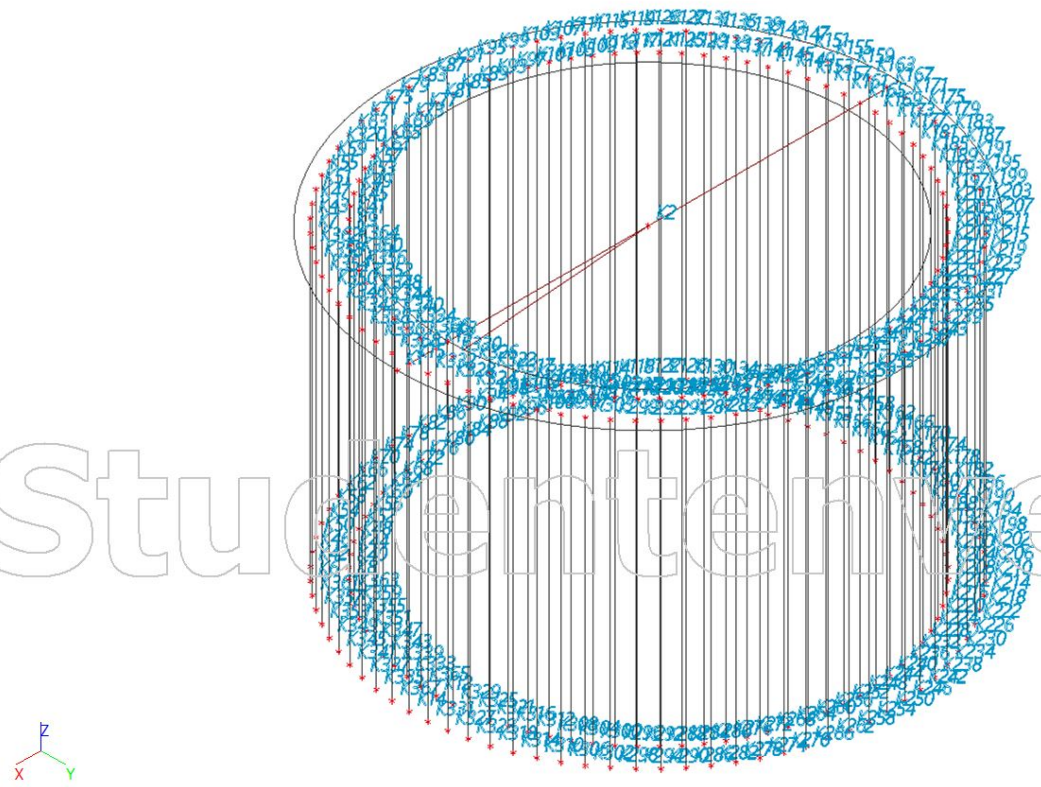

2.8. Knoopondersteuningen

Naam	Knoop	Systeem	Type	X	Y	Z	Rx	Ry	Rz
ankersteunpunt	K6	GCS	Standaard	Vast	Vast	Vast	Vrij	Vrij	Vrij
ankersteunpunt1	K8	GCS	Standaard	Vast	Vast	Vast	Vrij	Vrij	Vrij
ankersteunpunt2	K12	GCS	Standaard	Vast	Vast	Vast	Vrij	Vrij	Vrij
ankersteunpunt3	K14	GCS	Standaard	Vast	Vast	Vast	Vrij	Vrij	Vrij
ankersteunpunt4	K40	GCS	Standaard	Vast	Vast	Vast	Vrij	Vrij	Vrij
ankersteunpunt5	K42	GCS	Standaard	Vast	Vast	Vast	Vrij	Vrij	Vrij
ankersteunpunt6	K44	GCS	Standaard	Vast	Vast	Vast	Vrij	Vrij	Vrij
ankersteunpunt7	K46	GCS	Standaard	Vast	Vast	Vast	Vrij	Vrij	Vrij
ankersteunpunt8	K48	GCS	Standaard	Vast	Vast	Vast	Vrij	Vrij	Vrij
ankersteunpunt9	K50	GCS	Standaard	Vast	Vast	Vast	Vrij	Vrij	Vrij
ankersteunpunt10	K52	GCS	Standaard	Vast	Vast	Vast	Vrij	Vrij	Vrij
ankersteunpunt11	K54	GCS	Standaard	Vast	Vast	Vast	Vrij	Vrij	Vrij
ankersteunpunt12	K56	GCS	Standaard	Vast	Vast	Vast	Vrij	Vrij	Vrij
ankersteunpunt13	K58	GCS	Standaard	Vast	Vast	Vast	Vrij	Vrij	Vrij
ankersteunpunt14	K60	GCS	Standaard	Vast	Vast	Vast	Vrij	Vrij	Vrij
ankersteunpunt15	K62	GCS	Standaard	Vast	Vast	Vast	Vrij	Vrij	Vrij
ankersteunpunt16	K64	GCS	Standaard	Vast	Vast	Vast	Vrij	Vrij	Vrij
ankersteunpunt17	K66	GCS	Standaard	Vast	Vast	Vast	Vrij	Vrij	Vrij
ankersteunpunt18	K68	GCS	Standaard	Vast	Vast	Vast	Vrij	Vrij	Vrij
ankersteunpunt19	K70	GCS	Standaard	Vast	Vast	Vast	Vrij	Vrij	Vrij

Naam	Knoop	Systeem	Type	X	Y	Z	Rx	Ry	Rz
ankersteunpunt20	K72	GCS	Standaard	Vast	Vast	Vast	Vrij	Vrij	Vrij
ankersteunpunt21	K74	GCS	Standaard	Vast	Vast	Vast	Vrij	Vrij	Vrij
ankersteunpunt22	K76	GCS	Standaard	Vast	Vast	Vast	Vrij	Vrij	Vrij
ankersteunpunt23	K78	GCS	Standaard	Vast	Vast	Vast	Vrij	Vrij	Vrij
ankersteunpunt24	K80	GCS	Standaard	Vast	Vast	Vast	Vrij	Vrij	Vrij
ankersteunpunt25	K82	GCS	Standaard	Vast	Vast	Vast	Vrij	Vrij	Vrij
ankersteunpunt26	K84	GCS	Standaard	Vast	Vast	Vast	Vrij	Vrij	Vrij
ankersteunpunt27	K86	GCS	Standaard	Vast	Vast	Vast	Vrij	Vrij	Vrij
ankersteunpunt28	K88	GCS	Standaard	Vast	Vast	Vast	Vrij	Vrij	Vrij
ankersteunpunt29	K90	GCS	Standaard	Vast	Vast	Vast	Vrij	Vrij	Vrij
ankersteunpunt30	K92	GCS	Standaard	Vast	Vast	Vast	Vrij	Vrij	Vrij
ankersteunpunt31	K94	GCS	Standaard	Vast	Vast	Vast	Vrij	Vrij	Vrij
ankersteunpunt32	K96	GCS	Standaard	Vast	Vast	Vast	Vrij	Vrij	Vrij
ankersteunpunt33	K98	GCS	Standaard	Vast	Vast	Vast	Vrij	Vrij	Vrij
ankersteunpunt34	K100	GCS	Standaard	Vast	Vast	Vast	Vrij	Vrij	Vrij
ankersteunpunt35	K102	GCS	Standaard	Vast	Vast	Vast	Vrij	Vrij	Vrij
ankersteunpunt36	K104	GCS	Standaard	Vast	Vast	Vast	Vrij	Vrij	Vrij
ankersteunpunt37	K106	GCS	Standaard	Vast	Vast	Vast	Vrij	Vrij	Vrij
ankersteunpunt38	K108	GCS	Standaard	Vast	Vast	Vast	Vrij	Vrij	Vrij
ankersteunpunt39	K110	GCS	Standaard	Vast	Vast	Vast	Vrij	Vrij	Vrij
ankersteunpunt40	K112	GCS	Standaard	Vast	Vast	Vast	Vrij	Vrij	Vrij
ankersteunpunt41	K114	GCS	Standaard	Vast	Vast	Vast	Vrij	Vrij	Vrij
ankersteunpunt42	K116	GCS	Standaard	Vast	Vast	Vast	Vrij	Vrij	Vrij
ankersteunpunt43	K118	GCS	Standaard	Vast	Vast	Vast	Vrij	Vrij	Vrij
ankersteunpunt44	K120	GCS	Standaard	Vast	Vast	Vast	Vrij	Vrij	Vrij
ankersteunpunt45	K122	GCS	Standaard	Vast	Vast	Vast	Vrij	Vrij	Vrij
ankersteunpunt46	K124	GCS	Standaard	Vast	Vast	Vast	Vrij	Vrij	Vrij
ankersteunpunt47	K126	GCS	Standaard	Vast	Vast	Vast	Vrij	Vrij	Vrij
ankersteunpunt48	K128	GCS	Standaard	Vast	Vast	Vast	Vrij	Vrij	Vrij
ankersteunpunt49	K130	GCS	Standaard	Vast	Vast	Vast	Vrij	Vrij	Vrij
ankersteunpunt50	K132	GCS	Standaard	Vast	Vast	Vast	Vrij	Vrij	Vrij
ankersteunpunt51	K134	GCS	Standaard	Vast	Vast	Vast	Vrij	Vrij	Vrij
ankersteunpunt52	K136	GCS	Standaard	Vast	Vast	Vast	Vrij	Vrij	Vrij
ankersteunpunt53	K138	GCS	Standaard	Vast	Vast	Vast	Vrij	Vrij	Vrij
ankersteunpunt54	K140	GCS	Standaard	Vast	Vast	Vast	Vrij	Vrij	Vrij
ankersteunpunt55	K142	GCS	Standaard	Vast	Vast	Vast	Vrij	Vrij	Vrij
ankersteunpunt56	K144	GCS	Standaard	Vast	Vast	Vast	Vrij	Vrij	Vrij
ankersteunpunt57	K146	GCS	Standaard	Vast	Vast	Vast	Vrij	Vrij	Vrij
ankersteunpunt58	K148	GCS	Standaard	Vast	Vast	Vast	Vrij	Vrij	Vrij
ankersteunpunt59	K150	GCS	Standaard	Vast	Vast	Vast	Vrij	Vrij	Vrij
ankersteunpunt60	K152	GCS	Standaard	Vast	Vast	Vast	Vrij	Vrij	Vrij
ankersteunpunt61	K154	GCS	Standaard	Vast	Vast	Vast	Vrij	Vrij	Vrij
ankersteunpunt62	K156	GCS	Standaard	Vast	Vast	Vast	Vrij	Vrij	Vrij
ankersteunpunt63	K158	GCS	Standaard	Vast	Vast	Vast	Vrij	Vrij	Vrij
ankersteunpunt64	K160	GCS	Standaard	Vast	Vast	Vast	Vrij	Vrij	Vrij
ankersteunpunt65	K162	GCS	Standaard	Vast	Vast	Vast	Vrij	Vrij	Vrij
ankersteunpunt66	K164	GCS	Standaard	Vast	Vast	Vast	Vrij	Vrij	Vrij
ankersteunpunt67	K166	GCS	Standaard	Vast	Vast	Vast	Vrij	Vrij	Vrij
ankersteunpunt68	K168	GCS	Standaard	Vast	Vast	Vast	Vrij	Vrij	Vrij
ankersteunpunt69	K170	GCS	Standaard	Vast	Vast	Vast	Vrij	Vrij	Vrij
ankersteunpunt70	K172	GCS	Standaard	Vast	Vast	Vast	Vrij	Vrij	Vrij
ankersteunpunt71	K174	GCS	Standaard	Vast	Vast	Vast	Vrij	Vrij	Vrij
ankersteunpunt72	K176	GCS	Standaard	Vast	Vast	Vast	Vrij	Vrij	Vrij
ankersteunpunt73	K178	GCS	Standaard	Vast	Vast	Vast	Vrij	Vrij	Vrij
ankersteunpunt74	K180	GCS	Standaard	Vast	Vast	Vast	Vrij	Vrij	Vrij
ankersteunpunt75	K182	GCS	Standaard	Vast	Vast	Vast	Vrij	Vrij	Vrij
ankersteunpunt76	K184	GCS	Standaard	Vast	Vast	Vast	Vrij	Vrij	Vrij
ankersteunpunt77	K186	GCS	Standaard	Vast	Vast	Vast	Vrij	Vrij	Vrij
ankersteunpunt78	K188	GCS	Standaard	Vast	Vast	Vast	Vrij	Vrij	Vrij
ankersteunpunt79	K190	GCS	Standaard	Vast	Vast	Vast	Vrij	Vrij	Vrij
ankersteunpunt80	K192	GCS	Standaard	Vast	Vast	Vast	Vrij	Vrij	Vrij
ankersteunpunt81	K194	GCS	Standaard	Vast	Vast	Vast	Vrij	Vrij	Vrij
ankersteunpunt82	K196	GCS	Standaard	Vast	Vast	Vast	Vrij	Vrij	Vrij
ankersteunpunt83	K198	GCS	Standaard	Vast	Vast	Vast	Vrij	Vrij	Vrij
ankersteunpunt84	K200	GCS	Standaard	Vast	Vast	Vast	Vrij	Vrij	Vrij
ankersteunpunt85	K202	GCS	Standaard	Vast	Vast	Vast	Vrij	Vrij	Vrij
ankersteunpunt86	K204	GCS	Standaard	Vast	Vast	Vast	Vrij	Vrij	Vrij

Naam	Knoop	Systeem	Type	X	Y	Z	Rx	Ry	Rz
ankersteunpunt87	K206	GCS	Standaard	Vast	Vast	Vast	Vrij	Vrij	Vrij
ankersteunpunt88	K208	GCS	Standaard	Vast	Vast	Vast	Vrij	Vrij	Vrij
ankersteunpunt89	K210	GCS	Standaard	Vast	Vast	Vast	Vrij	Vrij	Vrij
ankersteunpunt90	K212	GCS	Standaard	Vast	Vast	Vast	Vrij	Vrij	Vrij
ankersteunpunt91	K214	GCS	Standaard	Vast	Vast	Vast	Vrij	Vrij	Vrij
ankersteunpunt92	K216	GCS	Standaard	Vast	Vast	Vast	Vrij	Vrij	Vrij
ankersteunpunt93	K218	GCS	Standaard	Vast	Vast	Vast	Vrij	Vrij	Vrij
ankersteunpunt94	K220	GCS	Standaard	Vast	Vast	Vast	Vrij	Vrij	Vrij
ankersteunpunt95	K222	GCS	Standaard	Vast	Vast	Vast	Vrij	Vrij	Vrij
ankersteunpunt96	K224	GCS	Standaard	Vast	Vast	Vast	Vrij	Vrij	Vrij
ankersteunpunt97	K226	GCS	Standaard	Vast	Vast	Vast	Vrij	Vrij	Vrij
ankersteunpunt98	K228	GCS	Standaard	Vast	Vast	Vast	Vrij	Vrij	Vrij
ankersteunpunt99	K230	GCS	Standaard	Vast	Vast	Vast	Vrij	Vrij	Vrij
ankersteunpunt100	K232	GCS	Standaard	Vast	Vast	Vast	Vrij	Vrij	Vrij
ankersteunpunt101	K234	GCS	Standaard	Vast	Vast	Vast	Vrij	Vrij	Vrij
ankersteunpunt102	K236	GCS	Standaard	Vast	Vast	Vast	Vrij	Vrij	Vrij
ankersteunpunt103	K238	GCS	Standaard	Vast	Vast	Vast	Vrij	Vrij	Vrij
ankersteunpunt104	K240	GCS	Standaard	Vast	Vast	Vast	Vrij	Vrij	Vrij
ankersteunpunt105	K242	GCS	Standaard	Vast	Vast	Vast	Vrij	Vrij	Vrij
ankersteunpunt106	K244	GCS	Standaard	Vast	Vast	Vast	Vrij	Vrij	Vrij
ankersteunpunt107	K246	GCS	Standaard	Vast	Vast	Vast	Vrij	Vrij	Vrij
ankersteunpunt108	K248	GCS	Standaard	Vast	Vast	Vast	Vrij	Vrij	Vrij
ankersteunpunt109	K250	GCS	Standaard	Vast	Vast	Vast	Vrij	Vrij	Vrij
ankersteunpunt110	K252	GCS	Standaard	Vast	Vast	Vast	Vrij	Vrij	Vrij
ankersteunpunt111	K254	GCS	Standaard	Vast	Vast	Vast	Vrij	Vrij	Vrij
ankersteunpunt112	K256	GCS	Standaard	Vast	Vast	Vast	Vrij	Vrij	Vrij
ankersteunpunt113	K258	GCS	Standaard	Vast	Vast	Vast	Vrij	Vrij	Vrij
ankersteunpunt114	K260	GCS	Standaard	Vast	Vast	Vast	Vrij	Vrij	Vrij
ankersteunpunt115	K262	GCS	Standaard	Vast	Vast	Vast	Vrij	Vrij	Vrij
ankersteunpunt116	K264	GCS	Standaard	Vast	Vast	Vast	Vrij	Vrij	Vrij
ankersteunpunt117	K266	GCS	Standaard	Vast	Vast	Vast	Vrij	Vrij	Vrij
ankersteunpunt118	K268	GCS	Standaard	Vast	Vast	Vast	Vrij	Vrij	Vrij
ankersteunpunt119	K270	GCS	Standaard	Vast	Vast	Vast	Vrij	Vrij	Vrij
ankersteunpunt120	K272	GCS	Standaard	Vast	Vast	Vast	Vrij	Vrij	Vrij
ankersteunpunt121	K274	GCS	Standaard	Vast	Vast	Vast	Vrij	Vrij	Vrij
ankersteunpunt122	K276	GCS	Standaard	Vast	Vast	Vast	Vrij	Vrij	Vrij
ankersteunpunt123	K278	GCS	Standaard	Vast	Vast	Vast	Vrij	Vrij	Vrij
ankersteunpunt124	K280	GCS	Standaard	Vast	Vast	Vast	Vrij	Vrij	Vrij
ankersteunpunt125	K282	GCS	Standaard	Vast	Vast	Vast	Vrij	Vrij	Vrij
ankersteunpunt126	K284	GCS	Standaard	Vast	Vast	Vast	Vrij	Vrij	Vrij
ankersteunpunt127	K286	GCS	Standaard	Vast	Vast	Vast	Vrij	Vrij	Vrij
ankersteunpunt128	K288	GCS	Standaard	Vast	Vast	Vast	Vrij	Vrij	Vrij
ankersteunpunt129	K290	GCS	Standaard	Vast	Vast	Vast	Vrij	Vrij	Vrij
ankersteunpunt130	K292	GCS	Standaard	Vast	Vast	Vast	Vrij	Vrij	Vrij
ankersteunpunt131	K294	GCS	Standaard	Vast	Vast	Vast	Vrij	Vrij	Vrij
ankersteunpunt132	K296	GCS	Standaard	Vast	Vast	Vast	Vrij	Vrij	Vrij
ankersteunpunt133	K298	GCS	Standaard	Vast	Vast	Vast	Vrij	Vrij	Vrij
ankersteunpunt134	K300	GCS	Standaard	Vast	Vast	Vast	Vrij	Vrij	Vrij
ankersteunpunt135	K302	GCS	Standaard	Vast	Vast	Vast	Vrij	Vrij	Vrij
ankersteunpunt136	K304	GCS	Standaard	Vast	Vast	Vast	Vrij	Vrij	Vrij
ankersteunpunt137	K306	GCS	Standaard	Vast	Vast	Vast	Vrij	Vrij	Vrij
ankersteunpunt138	K308	GCS	Standaard	Vast	Vast	Vast	Vrij	Vrij	Vrij
ankersteunpunt139	K310	GCS	Standaard	Vast	Vast	Vast	Vrij	Vrij	Vrij
ankersteunpunt140	K312	GCS	Standaard	Vast	Vast	Vast	Vrij	Vrij	Vrij
ankersteunpunt141	K314	GCS	Standaard	Vast	Vast	Vast	Vrij	Vrij	Vrij
ankersteunpunt142	K316	GCS	Standaard	Vast	Vast	Vast	Vrij	Vrij	Vrij
ankersteunpunt143	K318	GCS	Standaard	Vast	Vast	Vast	Vrij	Vrij	Vrij
ankersteunpunt144	K321	GCS	Standaard	Vast	Vast	Vast	Vrij	Vrij	Vrij
ankersteunpunt145	K323	GCS	Standaard	Vast	Vast	Vast	Vrij	Vrij	Vrij
ankersteunpunt146	K325	GCS	Standaard	Vast	Vast	Vast	Vrij	Vrij	Vrij
ankersteunpunt147	K327	GCS	Standaard	Vast	Vast	Vast	Vrij	Vrij	Vrij
ankersteunpunt148	K329	GCS	Standaard	Vast	Vast	Vast	Vrij	Vrij	Vrij
ankersteunpunt149	K331	GCS	Standaard	Vast	Vast	Vast	Vrij	Vrij	Vrij
ankersteunpunt150	K333	GCS	Standaard	Vast	Vast	Vast	Vrij	Vrij	Vrij
ankersteunpunt151	K335	GCS	Standaard	Vast	Vast	Vast	Vrij	Vrij	Vrij
ankersteunpunt152	K337	GCS	Standaard	Vast	Vast	Vast	Vrij	Vrij	Vrij
ankersteunpunt153	K339	GCS	Standaard	Vast	Vast	Vast	Vrij	Vrij	Vrij

Naam	Knoop	Systeem	Type	X	Y	Z	Rx	Ry	Rz
ankersteunpunt154	K341	GCS	Standaard	Vast	Vast	Vast	Vrij	Vrij	Vrij
ankersteunpunt155	K343	GCS	Standaard	Vast	Vast	Vast	Vrij	Vrij	Vrij
ankersteunpunt156	K345	GCS	Standaard	Vast	Vast	Vast	Vrij	Vrij	Vrij
ankersteunpunt157	K347	GCS	Standaard	Vast	Vast	Vast	Vrij	Vrij	Vrij
ankersteunpunt158	K349	GCS	Standaard	Vast	Vast	Vast	Vrij	Vrij	Vrij
ankersteunpunt159	K351	GCS	Standaard	Vast	Vast	Vast	Vrij	Vrij	Vrij
ankersteunpunt160	K353	GCS	Standaard	Vast	Vast	Vast	Vrij	Vrij	Vrij
ankersteunpunt161	K355	GCS	Standaard	Vast	Vast	Vast	Vrij	Vrij	Vrij
ankersteunpunt162	K357	GCS	Standaard	Vast	Vast	Vast	Vrij	Vrij	Vrij
ankersteunpunt163	K359	GCS	Standaard	Vast	Vast	Vast	Vrij	Vrij	Vrij
ankersteunpunt164	K361	GCS	Standaard	Vast	Vast	Vast	Vrij	Vrij	Vrij
ankersteunpunt165	K363	GCS	Standaard	Vast	Vast	Vast	Vrij	Vrij	Vrij
ankersteunpunt166	K365	GCS	Standaard	Vast	Vast	Vast	Vrij	Vrij	Vrij
ankersteunpunt167	K367	GCS	Standaard	Vast	Vast	Vast	Vrij	Vrij	Vrij

3. Belastingen

3.1. Belastingsgevallen

Naam	Omschrijving	Actie type	Lastgroep
	Spec	Belastingtype	
BG1	Voorspan ankers	Permanent	LG1
		Standaard	
BG2	Moment	Permanent	LG1
		Standaard	

3.2. BG1 / Voorspanning

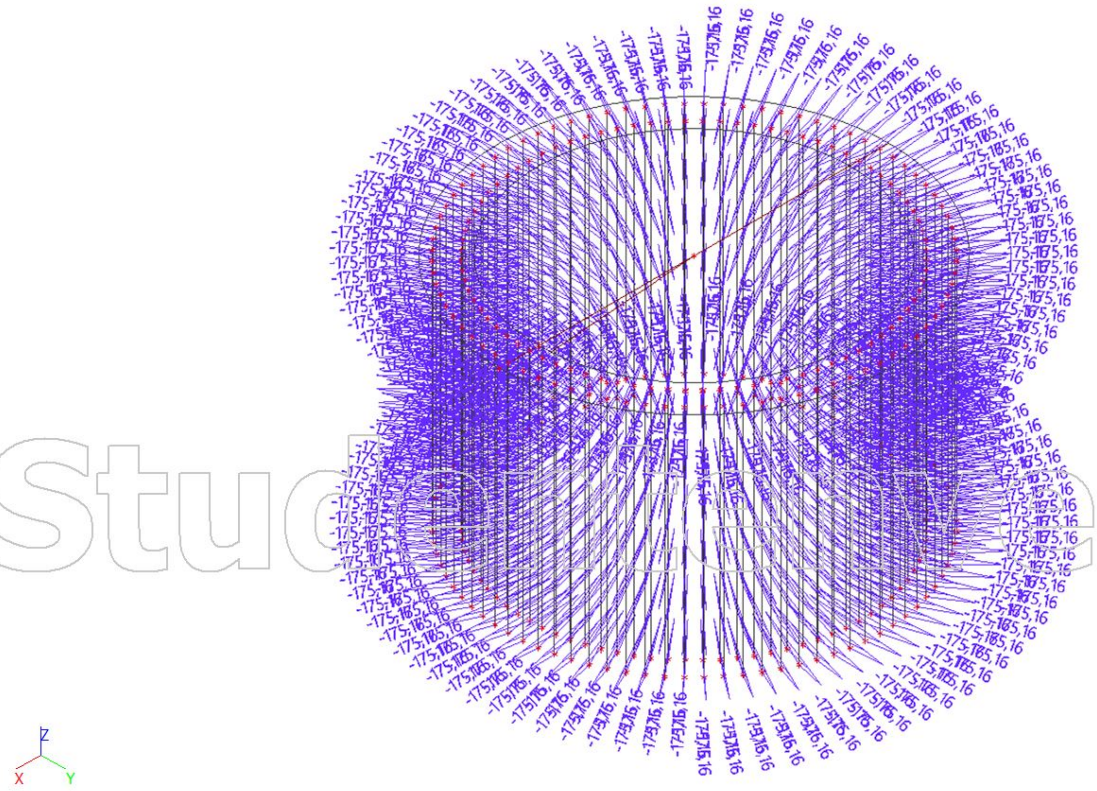

3.3. BG2 / Moment

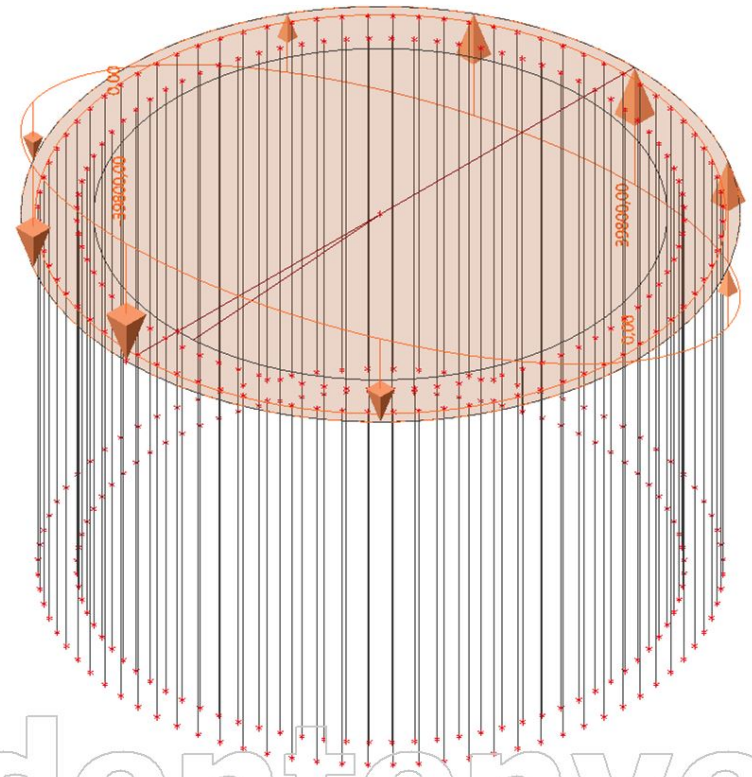

3.4. Combinaties

Naam	Omschrijving	Type	Belastingsgevallen	Coëff. [-]
Voorspanning		EN-UGT (STR/GEO) Set B	BG1 - Voorspan ankers	1,00
Moment		EN - BGT Karakteristiek	BG2 - Moment	1,00
Voor+Mom		EN-BGT Quasi-permanent	BG1 - Voorspan ankers	1,00
			BG2 - Moment	1,00

4. Voorspanning

4.1. 3D verplaatsing

Niet-lineaire berekening
Niet-lineaire combinatie: Voorspan
Selectie: Alle
Locatie: In knooppunten gem. bij macro. Systeem: LCS net element

Resultaten op 1D-element:
Extreme 1D: Globaal

Naam	dx [mm]	Vezel	Belasting	u_x [mm]	u_y [mm]	u_z [mm]	φ_x [rad]	φ_y [rad]	φ_z [rad]	U_{total} [mm]
Ankerstaaf	0,000	1	Voorspan	0,000	0,000	0,000	0,000	0,000	0,000	**0,000**
Ankerstaaf	3000,000	1	Voorspan	-0,580	0,000	0,000	0,000	0,000	0,000	**0,580**

Resultaten op 2D-element:
Extreme 2D: Globaal

Naam	Net	Positie [mm]	Belasting	ux+ [mm] ux- [mm]	uy+ [mm] uy- [mm]	uz+ [mm] uz- [mm]	φ_x [rad]	φ_y [rad]	φ_z [rad]	U totaal+ [mm] U totaal- [mm]
E1	Element: 80 Knoop: 898	-2482,671 293,843 0,000	Voorspan	**0,000** **0,000**	**0,000** **0,000**	**-0,580** **-0,580**	**0,000**	**0,000**	**0,000**	**0,580** **0,580**

4.2. 3D verplaatsing; u_z

Waardes: u_z
Niet-lineaire berekening
Niet-lineaire combinatie: Voorspan
Selectie: Alle
Locatie: In knooppunten gem. bij macro. Systeem: LCS net element

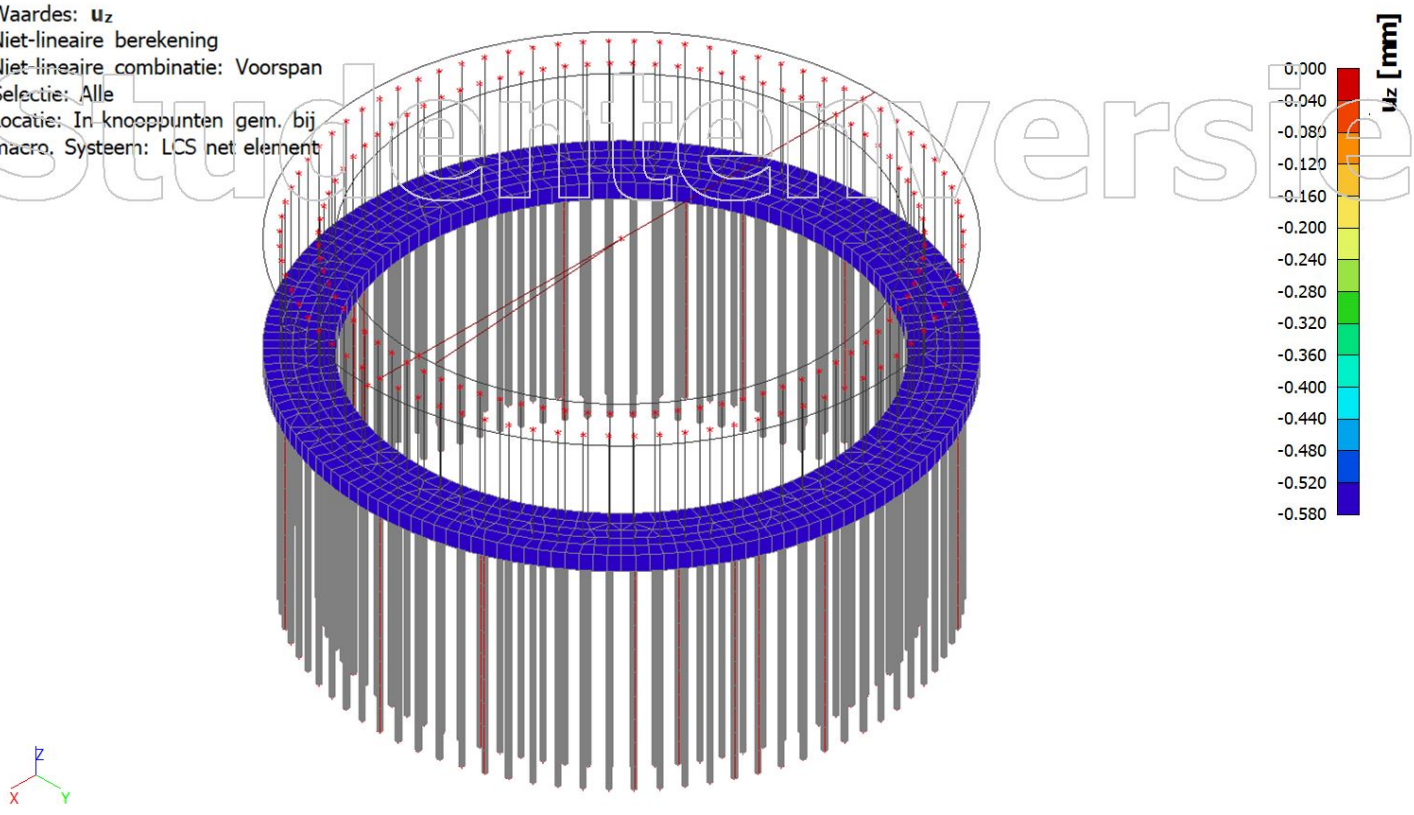

4.3. Contactspanningen; sigmaz Voorspanning

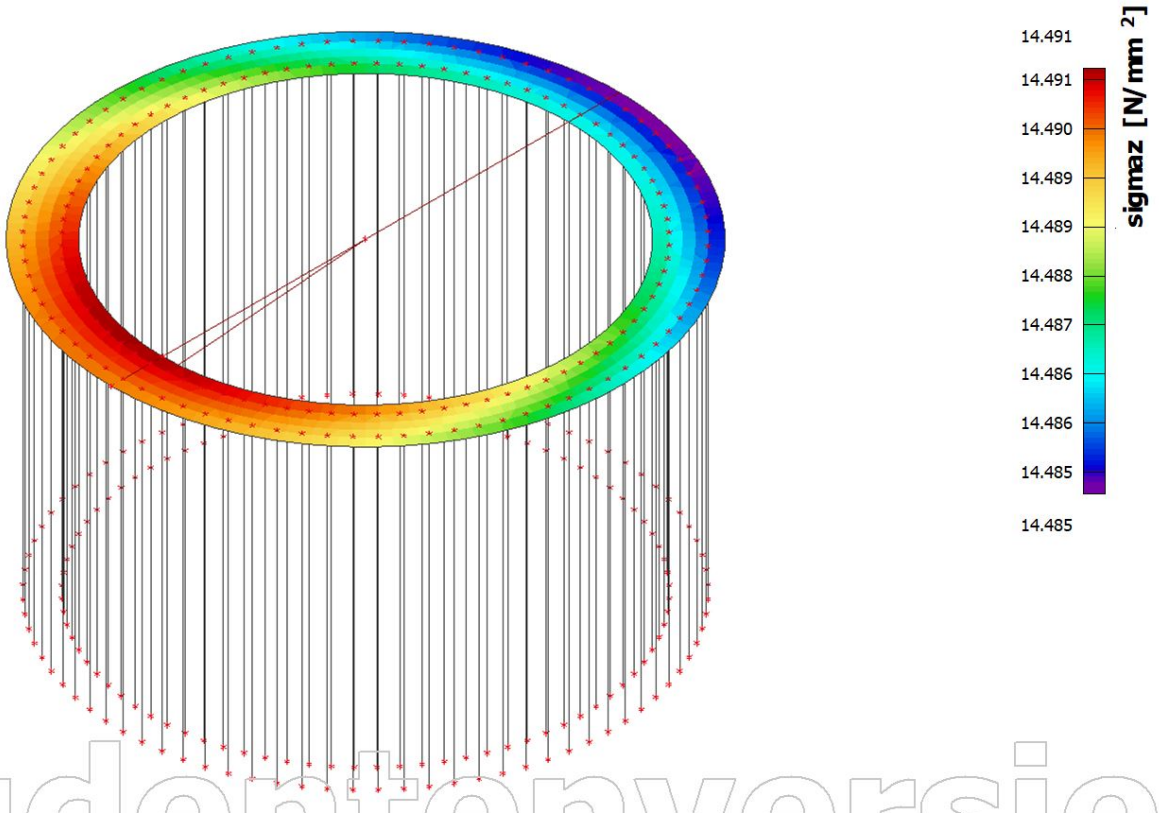

4.4. Reacties; Rz Voorspanning

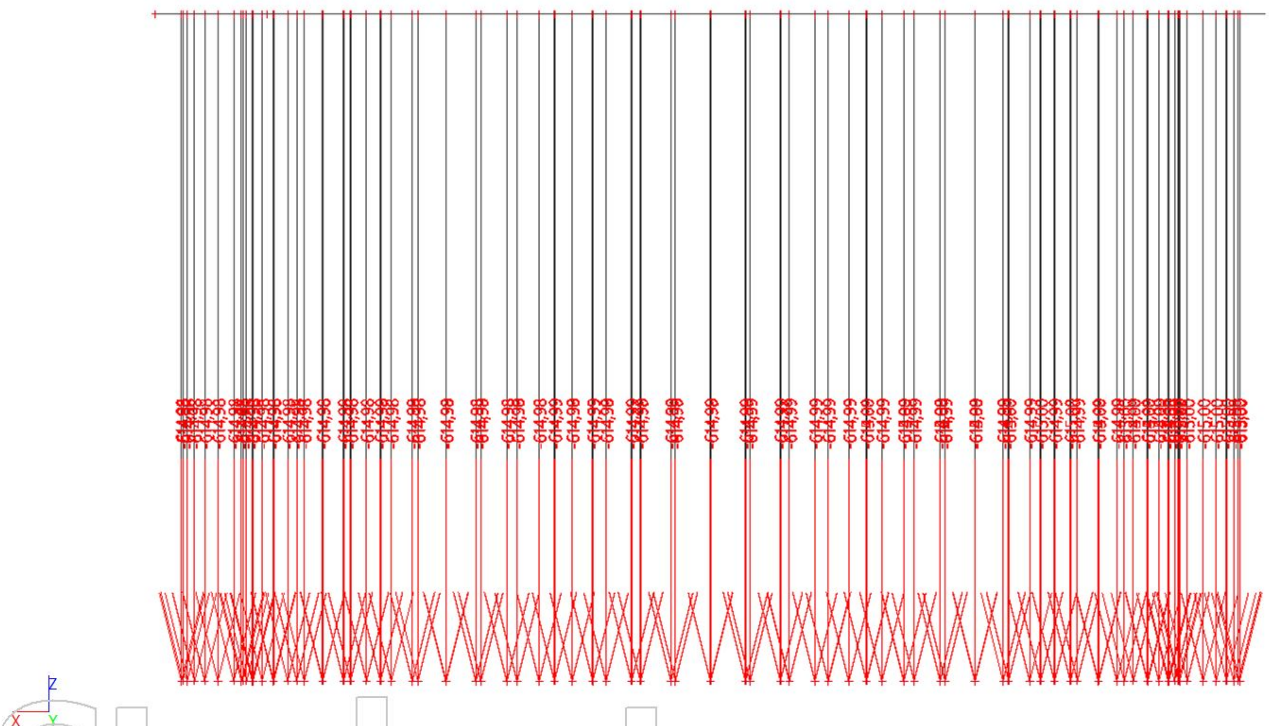

4.5. Resultante; Rx, Ry, Rz, Mx, My, Mz Voorspanning

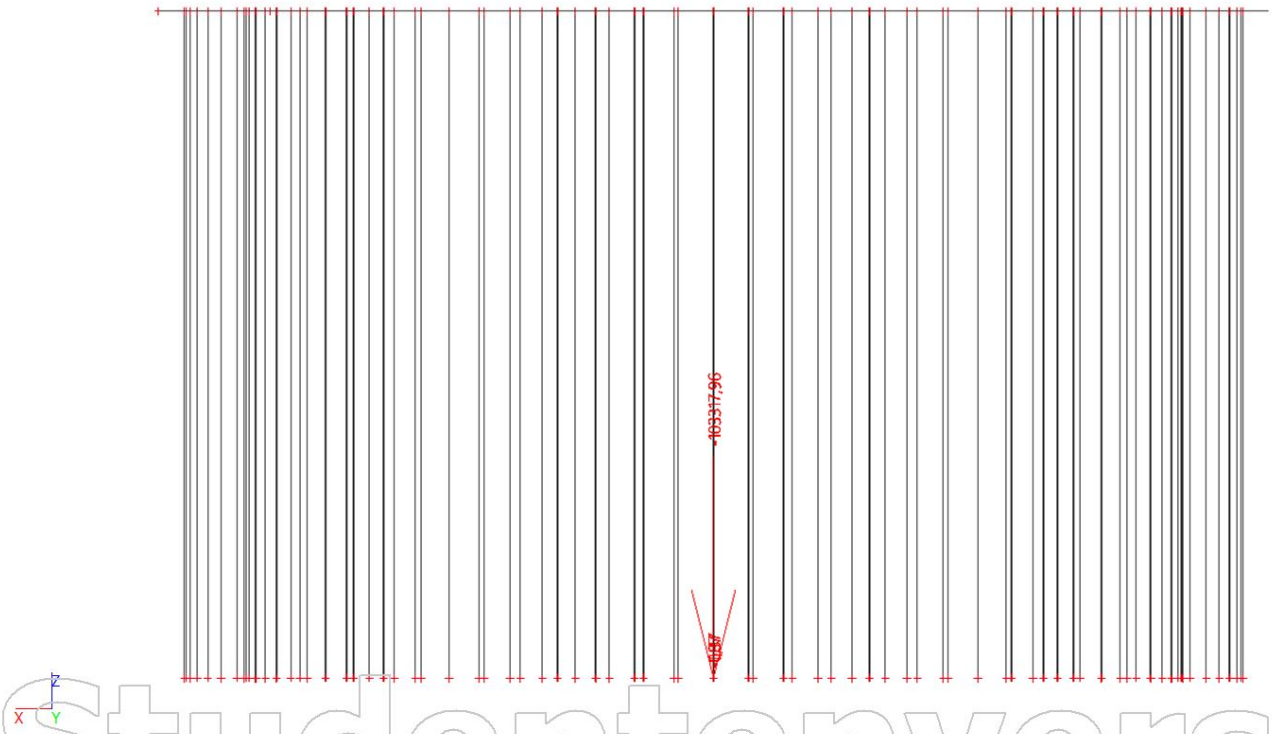

5. Voorspanning + Moment

5.1. 3D verplaatsing

Niet-lineaire berekening
Niet-lineaire combinatie: Voor+Mom
Selectie: Alle
Locatie: In knooppunten gem. bij macro. Systeem: LCS net element

Resultaten op 1D-element:
Extreme 1D: Globaal

Naam	dx [mm]	Vezel	Belasting	u_x [mm]	u_y [mm]	u_z [mm]	φ_x [rad]	φ_y [rad]	φ_z [rad]	U_{total} [mm]
Ankerstaaf28	0,000	1	Voor+Mom	0,000	0,000	0,000	0,000	0,000	0,000	**0,000**
Ankerstaaf81	3000,000	1	Voor+Mom	3,637	0,000	0,000	0,000	0,000	0,000	**3,637**

Resultaten op 2D-element:
Extreme 2D: Globaal

Naam	Net	Positie [mm]	Belasting	ux+ [mm] ux- [mm]	uy+ [mm] uy- [mm]	uz+ [mm] uz- [mm]	φ_x [rad]	φ_y [rad]	φ_z [rad]	U totaal+ [mm] U totaal- [mm]
E1	Element: 29 Knoop: 467	1134,976 2227,516 0,000	Voor+Mom	0,091 -0,091	0,001 -0,001	-0,968 -0,968	**0,000**	0,001	0,000	0,973 0,973
E1	Element: 1 Knoop: 1	2500,000 0,000 0,000	Voor+Mom	0,091 -0,091	0,000 0,000	**-2,728** **-2,728**	0,000	**0,001**	**0,000**	2,730 2,730
E1	Element: 199 Knoop: 380	389,205 -1956,667 0,000	Voor+Mom	0,091 -0,091	0,000 0,000	0,003 0,003	**0,000**	0,001	0,000	**0,091** **0,091**
E1	Element: 83 Knoop: 3	-2500,000 0,000 0,000	Voor+Mom	**0,092** **-0,092**	**0,000** **0,000**	**3,791** **3,791**	0,000	**0,001**	**0,000**	**3,792** **3,792**

5.2. 3D verplaatsing; u_z

Waardes: u_z
Niet-lineaire berekening
Niet-lineaire combinatie: Voor+Mom
Selectie: Alle
Locatie: In knooppunten gem. bij macro. Systeem: LCS net element

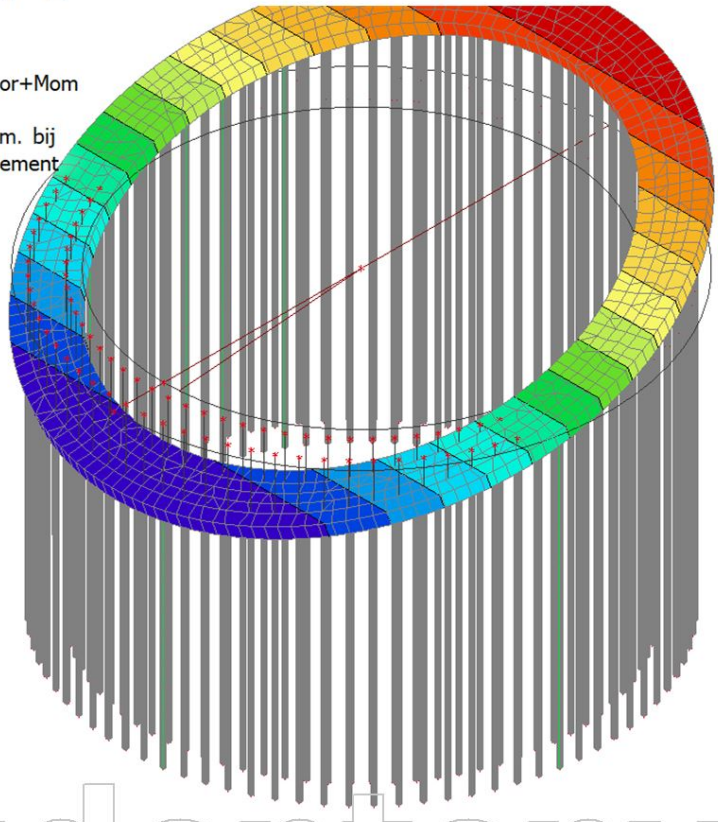

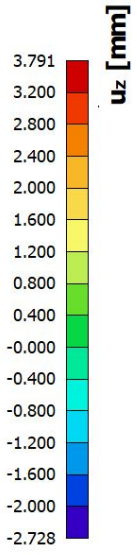

5.3. Contactspanningen; sigmaz Voorspanning + Moment

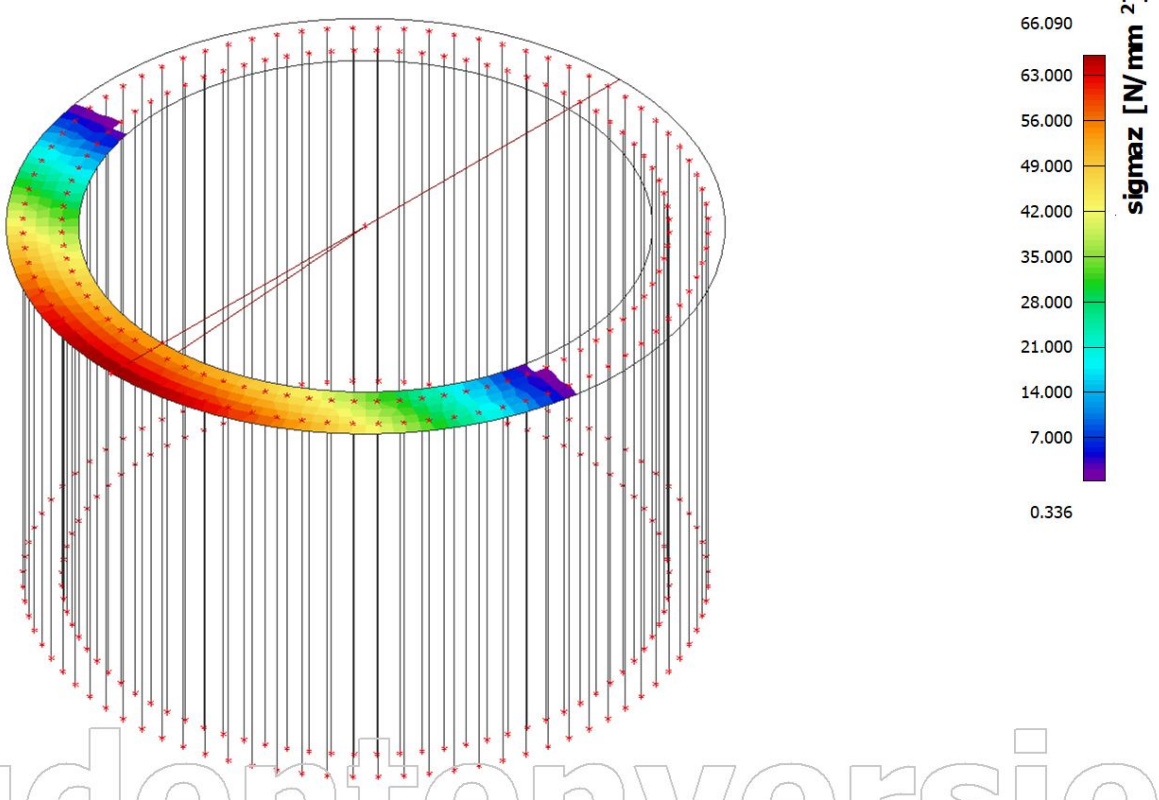

5.4. Reacties; Rz Voorspanning + Moment

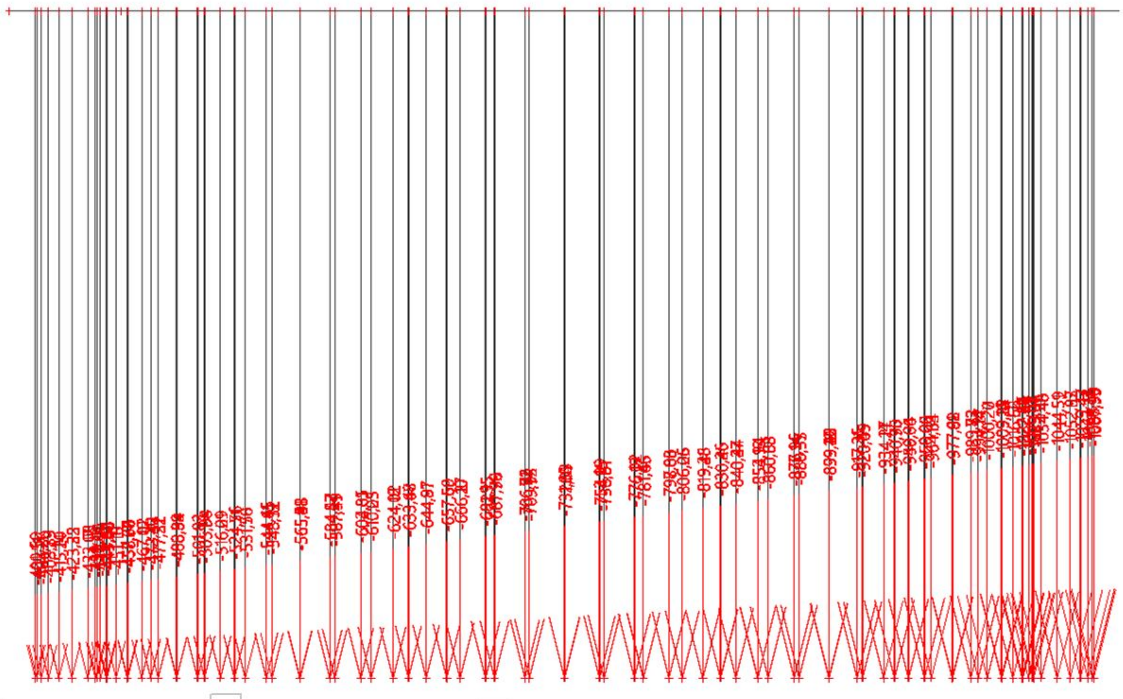

5.5. Resultante; Rx, Ry, Rz, Mx, My, Mz Voorspanning + Moment

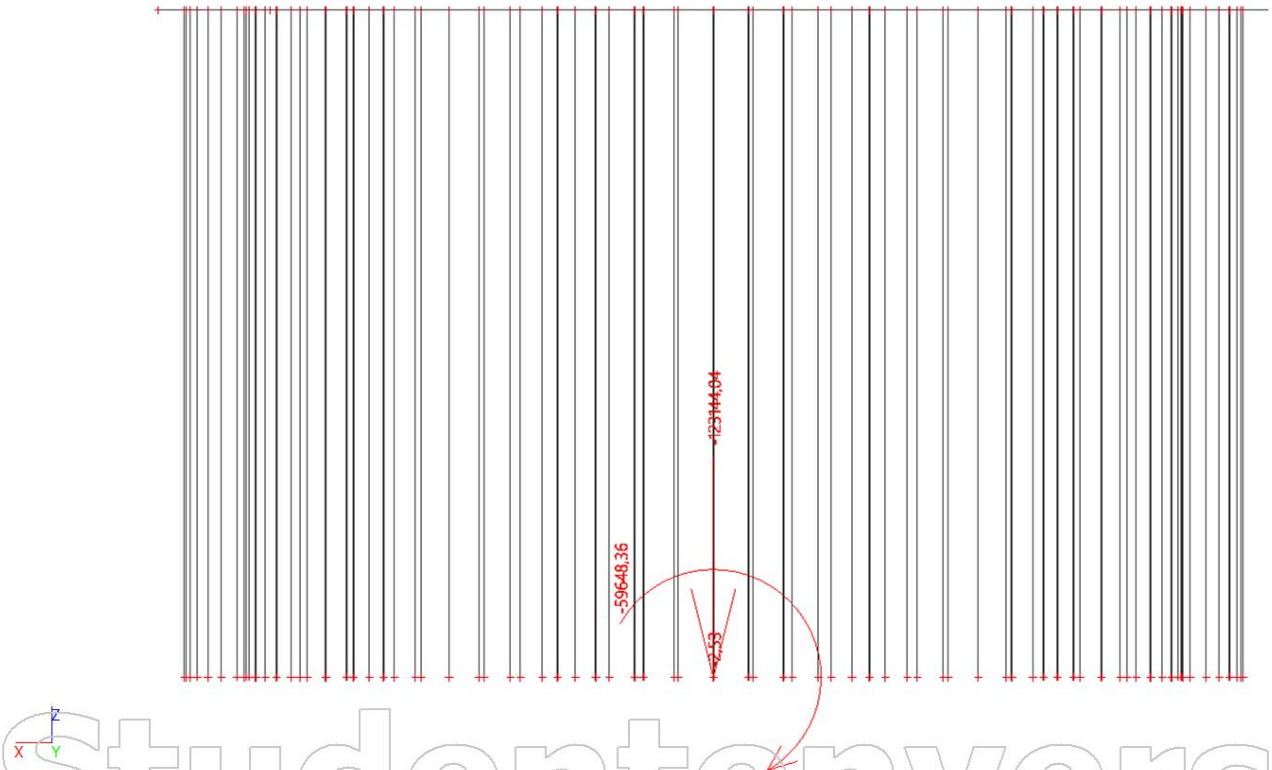

3. DATABASE ACTIVELY CONFINED CONCRETE

APPENDIX

Table 1. Test database of actively confined concrete specimens

Paper	Number of specimen per data entry	Geometries		Concrete Properties			Peak Conditions				Residual Conditions		
		D (mm)	H (mm)	f'_{co} (MPa)	ε_{co} (%)	ε_{lo} (%)	f^*_l (MPa)	f^*_{cc} (MPa)	ε^*_{cc} (%)	ε^*_l (%)	$f_{c,res}$ (MPa)	$\varepsilon_{c,res}$ (%)	$\varepsilon_{l,res}$ (%)
		101	202	47.23	0.202		8.29	79.79	1.350				
Ansari and Li (1998)	2	101	202	47.23	0.202		16.59	109.74	1.568				
Ansari and Li (1998)	2	101	202	47.23	0.202		24.88	130.80	2.049				
Ansari and Li (1998)	6	101	202	47.23	0.202		33.17	144.30	2.420				
Ansari and Li (1998)	2	101	202	47.23	0.202		41.47	167.04	2.950				
Ansari and Li (1998)	4	101	202	71.08	0.203		13.16	129.13	0.798				
Ansari and Li (1998)	3	101	202	71.08	0.203		26.32	156.15	1.258				
Ansari and Li (1998)	2	101	202	71.08	0.203		39.48	185.38	2.042				
Ansari and Li (1998)	2	101	202	71.08	0.203		52.65	209.37	3.019				
Ansari and Li (1998)	2	101	202	71.08	0.203		65.80	224.77	3.868				
Ansari and Li (1998)	2	101	202	107.28	0.194		20.90	192.50	0.890				
Ansari and Li (1998)	3	101	202	107.28	0.194		41.80	232.97	1.065				
Ansari and Li (1998)	2	101	202	107.28	0.194		62.70	285.91	1.930				
Ansari and Li (1998)	2	101	202	107.28	0.194		83.59	314.95	2.096				
Attard and Setunge (1996)	1	100	200	120	0.3		0.5	125	0.26				
Attard and Setunge (1996)	1	100	200	120	0.3		1	128	0.29		33.7	0.70	
Attard and Setunge (1996)	1	100	200	120	0.3		5	165	0.38		110.3	0.69	
Attard and Setunge (1996)	1	100	200	120	0.3		10	192	0.53		99.3	1.23	
Attard and Setunge (1996)	1	100	200	120	0.3		15	220	0.60		136.3	1.33	
Attard and Setunge (1996)	1	100	200	120	0.3		20	234	0.80		130.9	1.90	
Attard and Setunge (1996)	1	100	200	120	0.28		5	168	0.42		83.2	0.89	
Attard and Setunge (1996)	1	100	200	120	0.28		10	187	0.48		101.2	1.21	
Attard and Setunge (1996)	1	100	200	120	0.28		15	211	0.57		199.6	0.70	
Attard and Setunge (1996)	1	100	200	110	0.28		5	150	0.35		63.0	1.25	
Attard and Setunge (1996)	1	100	200	110	0.28		10	175	0.44		104.7	1.21	
Attard and Setunge (1996)	1	100	200	110	0.28		15	192	0.60		126.9	1.41	
Attard and Setunge (1996)	1	100	200	100	0.27		1	106	0.31				
Attard and Setunge (1996)	1	100	200	100	0.27		5	121	0.36				
Attard and Setunge (1996)	1	100	200	100	0.27		10	144	0.47				
Attard and Setunge (1996)	1	100	200	100	0.27		15	165	0.58				
Attard and Setunge (1996)	1	100	200	132	0.34		5	180	0.50		82.5	1.11	
Attard and Setunge (1996)	1	100	200	132	0.34		10	200	0.58		101.4	1.36	
Attard and Setunge (1996)	1	100	200	132	0.34		15	222	0.78		123.0	1.67	
Attard and Setunge (1996)	1	100	200	126	0.34		5	162	0.50				
Attard and Setunge (1996)	1	100	200	126	0.34		10	186	0.71				
Attard and Setunge (1996)	1	100	200	126	0.34		15	211	0.89				
Attard and Setunge (1996)	1	100	200	118	0.28		5	154	0.38		79.4	1.08	
Attard and Setunge (1996)	1	100	200	118	0.28		10	173	0.49		76.2	0.87	
Attard and Setunge (1996)	1	100	200	118	0.28		15	201	0.62		107.5	1.97	
Attard and Setunge (1996)	1	100	200	110	0.28		5	153	0.41		80.3	1.07	
Attard and Setunge (1996)	1	100	200	110	0.28		10	164	0.55		104.9	1.09	
Attard and Setunge (1996)	1	100	200	110	0.28		15	185	0.59		123.1	1.85	
Attard and Setunge (1996)	1	100	200	100	0.26		5	127	0.39		76.4	1.01	
Attard and Setunge (1996)	1	100	200	100	0.26		10	153	0.52		102.9	1.39	
Attard and Setunge (1996)	1	100	200	100	0.26		15	169	0.75		127.4	1.78	
Attard and Setunge (1996)	1	100	200	96	0.28		5	119	0.37				
Attard and Setunge (1996)	1	100	200	96	0.28		10	147	0.52				
Attard and Setunge (1996)	1	100	200	96	0.28		15	157	0.53				
Attard and Setunge (1996)	1	100	200	60	0.21		1	67	0.27				
Attard and Setunge (1996)	1	100	200	60	0.21		5	98	0.48				
Attard and Setunge (1996)	1	100	200	60	0.21		10	122	0.76				
Attard and Setunge (1996)	1	100	200	60	0.21		15	145	0.99				
Balmer (1949)	9	152	305	24.6	0.36		172.37	535.21	4.140*				
Balmer (1949)	9	152	305	24.6	0.36		137.90	469.95	4.772*				
Balmer (1949)	9	152	305	24.6	0.36		103.42	369.05	4.651*				
Balmer (1949)	9	152	305	24.6	0.36		68.95	273.74	4.758*				
Balmer (1949)	9	152	305	24.6	0.36		34.47	168.06	3.051*				
Bellotti and Rossi (1991)	1	160	320	53.5	0.31	0.17	4.9	84.3	1.01	0.30			
Bellotti and Rossi (1991)	1	160	320	53.5	0.31	0.17	9.8	104.6	1.35	0.90			
Bellotti and Rossi (1991)	1	160	320	53.5	0.31	0.17	14.7	125.0	1.80	0.58			
Bellotti and Rossi (1991)	1	160	320	53.5	0.31	0.17	19.6	147.1	2.37	0.92			
Bellotti and Rossi (1991)	1	160	320	53.5	0.31	0.17	24.5	163.8	2.29	1.13			
Bellotti and Rossi (1991)	1	160	320	53.5	0.31	0.17	29.4	184.1	2.62	1.14			
Bellotti and Rossi (1991)	1	160	320	53.5	0.31	0.17	34.3	198.2	3.38	1.20			
Bellotti and Rossi (1991)	1	160	320	53.5	0.31	0.17	39.2	210.8	3.52	1.14			
Candappa et al. (2001)	1	98	200	41.9	0.24	0.13	4	66.6	0.87	0.63	63.6	1.14	1.26
Candappa et al. (2001)	1	98	200	41.9	0.24	0.13	8	85.1	1.25	0.82	82.7	1.44	1.33
Candappa et al. (2001)	1	98	200	41.9	0.24	0.13	8	85.4	1.05	0.49	83.1	1.64	1.33
Candappa et al. (2001)	1	98	200	41.9	0.24	0.13	12	102.4	1.72	0.9	99.2	2.19	1.59
Candappa et al. (2001)	1	98	200	41.9	0.24	0.13	12	105.1	1.67	0.72	101.7	2.38	1.59
Candappa et al. (2001)	1	98	200	60.6	0.24	0.1	4	78.2	0.40	0.12	62.4	0.80	0.86
Candappa et al. (2001)	1	98	200	60.6	0.24	0.1	5	81.8	0.53	0.45	69.9	0.77	1.33
Candappa et al. (2001)	1	98	200	60.6	0.24	0.1	8	97.8	0.98	0.46	89.2	1.54	1.30
Candappa et al. (2001)	1	98	200	60.6	0.24	0.1	12	115.5	1.24	0.42	113.8	1.68	0.85
Candappa et al. (2001)	1	98	200	73.1	0.24	0.21	4	102.6	0.45	0.16	79.0	0.79	0.96
Candappa et al. (2001)	1	98	200	73.1	0.24	0.21	8	121.5	0.63	0.30	92.1	1.31	1.30
Candappa et al. (2001)	1	98	200	73.1	0.24	0.21	8	122.3	0.69	0.29	100.3	1.43	1.66
Candappa et al. (2001)	1	98	200	73.1	0.24	0.21	12	138.1	0.94	0.46	131.1	0.65	0.21
Candappa et al. (2001)	1	98	200	103.3	0.3	0.12	4	133.1	0.43	0.17	126.7	0.48	0.39

Paper	n	D (mm)	H (mm)	f'_{co} (MPa)	ε_{co} (%)	ε_{lo} (%)	f^*_l (MPa)	f^*_{cc} (MPa)	ε^*_{cc} (%)	ε^*_l (%)	$f_{c,res}$ (MPa)	$\varepsilon_{c,res}$ (%)	$\varepsilon_{l,res}$ (%)
Candappa et al. (2001)	1	98	200	103.3	0.3	0.12	8	151.0	0.68	0.29	116.7	1.05	1.19
Candappa et al. (2001)	1	98	200	103.3	0.3	0.12	8	158.0	0.67	0.23	146.1	0.73	0.64
Candappa et al. (2001)	1	98	200	103.3	0.3	0.12	12	171.5	0.80	0.35	147.3	0.99	1.01
Candappa et al. (2001)	1	98	200	103.3	0.3	0.12	12	169.3	0.78	0.30	154.1	1.00	0.95
Gabet et al. (2008)	1	70	140	30			50	171.70	2.708*	0.842	168.44	3.229*	1.372
Gabet et al. (2008)	1	70	140	30			100	280.85	8.039*	3.192	278.14	8.039*	3.192
Gabet et al. (2008)	1	70	140	30			200	487.68	10.196*	3.192	487.68	10.196*	3.192
Gabet et al. (2008)	1	70	140	30			500	708.28	6.552*	1.594	708.16	6.552*	1.594
Gabet et al. (2008)	1	70	140	30			650	1002.99	9.476*	4.058	1000.57	9.476*	4.058
Gardner (1969)	3	76.2	152.4	28.96	0.4		8.62	72.39	0.70*				
Gardner (1969)	4	76.2	152.4	28.96	0.4		17.24	117.90	2.15*				
Gardner (1969)	5	76.2	152.4	28.96	0.4		25.86	144.79	2.60*				
Hammons and Neeley (1993)	1	53.6	88.9	96			50	257	1.5				
Hammons and Neeley (1993)	1	51	88.5	96			100	408	10.0*				
Hammons and Neeley (1993)	1	53.6	88.5	96			150	540	10.0*				
Hammons and Neeley (1993)	1	53.6	88.9	96			200	631	10.0*				
Hurlbut (1985)	1	54	108	19	0.18		0.69	26.2	0.33				
Hurlbut (1985)	1	54	108	19	0.18		3.45	33.3	0.94				
Hurlbut (1985)	1	54	108	19	0.18		6.89	51.8	1.47				
Hurlbut (1985)	1	54	108	19	0.18		13.76	78.3	1.57*				
Imran (1994)	1	54	115	43	0.24	0.09	14	106.6	3.29*	1.41			
Imran (1994)	1	54	115	43	0.24	0.09	43	182.3	4.60	0.91			
Imram and Pantazopoulou (1996)	1	54	115	73.35	0.325	0.31	3.2	96.1	0.495	0.445			
Imram and Pantazopoulou (1996)	1	54	115	73.35	0.325	0.31	6.4	108.7	0.650	0.660			
Imram and Pantazopoulou (1996)	1	54	115	73.35	0.325	0.31	12.8	125.6	1.045	1.100			
Imram and Pantazopoulou (1996)	1	54	115	73.35	0.325	0.31	25.6	168.6	2.025	2.465*			
Imram and Pantazopoulou (1996)	1	54	115	73.35	0.325	0.31	38.4	204.0	3.105	4.525*			
Imram and Pantazopoulou (1996)	1	54	115	73.35	0.325	0.31	51.2	240.5	4.090	3.920*			
Imram and Pantazopoulou (1996)	1	54	115	64.69	0.297	0.277	3.2	80.9	0.455	0.510	76.48	0.611	0.468
Imram and Pantazopoulou (1996)	1	54	115	64.69	0.297	0.277	6.4	96.8	0.61	0.800	91.59	0.864	0.493
Imram and Pantazopoulou (1996)	1	54	115	64.69	0.297	0.277	12.8	113.5	1.125	1.335	97.88	2.441	2.709
Imram and Pantazopoulou (1996)	1	54	115	64.69	0.297	0.277	25.6	153.9	2.235	2.585*	145.11	4.186	4.538
Imram and Pantazopoulou (1996)	1	54	115	64.69	0.297	0.277	38.4	190.6	3.495	3.110*	188.72	4.258	3.483
Imram and Pantazopoulou (1996)	1	54	115	64.69	0.297	0.277	51.2	230.5	5.03	5.390*	231.82	6.246	
Imram and Pantazopoulou (1996)	1	54	115	47.4	0.28	0.273	2.15	57.7	0.43	0.395			
Imram and Pantazopoulou (1996)	1	54	115	47.4	0.28	0.273	4.3	67.3	0.69	0.585			
Imram and Pantazopoulou (1996)	1	54	115	47.4	0.28	0.273	8.6	83.6	1.46	1.305			
Imram and Pantazopoulou (1996)	1	54	115	47.4	0.28	0.273	17.2	118.1	2.53	2.470			
Imram and Pantazopoulou (1996)	1	54	115	47.4	0.28	0.273	30.1	161.1	3.6	2.015			
Imram and Pantazopoulou (1996)	1	54	115	47.4	0.28	0.273	43	204.7	4.73	5.950*			
Imram and Pantazopoulou (1996)	1	54	115	43.11	0.25	0.295	2.15	46.0	0.43	0.405	41.33	0.836	0.692
Imram and Pantazopoulou (1996)	1	54	115	43.11	0.25	0.295	4.3	53.5	0.65	0.63	53.92	0.836	0.526
Imram and Pantazopoulou (1996)	1	54	115	43.11	0.25	0.295	8.6	73.0	1.66	1.86	67.85	2.982	2.695
Imram and Pantazopoulou (1996)	1	54	115	43.11	0.25	0.295	17.2	107.0	2.81	3.580*	102.96	4.544	
Imram and Pantazopoulou (1996)	1	54	115	43.11	0.25	0.295	30.1	149.3	4.23	5.410*	149.29	4.856	
Imram and Pantazopoulou (1996)	1	54	115	43.11	0.25	0.295	43	184.2	5.02	8.500*	184.59		
Imram and Pantazopoulou (1996)	1	54	115	28.62	0.26	0.24	1.05	33.6	0.47	0.315			
Imram and Pantazopoulou (1996)	1	54	115	28.62	0.26	0.24	2.1	36.4	0.675	0.405			
Imram and Pantazopoulou (1996)	1	54	115	28.62	0.26	0.24	4.2	48.1	1.385	0.810			
Imram and Pantazopoulou (1996)	1	54	115	28.62	0.26	0.24	8.4	65.2	2.375	2.340			
Imram and Pantazopoulou (1996)	1	54	115	28.62	0.26	0.24	14.7	92.3	3.425	3.570*			
Imram and Pantazopoulou (1996)	1	54	115	28.62	0.26	0.24	21	114.5	4.46	3.800*			
Imram and Pantazopoulou (1996)	1	54	115	21.17	0.22	0.26	1.05	25.9	0.36	0.430	21.51	1.178	1.706
Imram and Pantazopoulou (1996)	1	54	115	21.17	0.22	0.26	2.1	28.5	0.66	0.510	24.49	2.094	3.480
Imram and Pantazopoulou (1996)	1	54	115	21.17	0.22	0.26	4.2	38.0	1.62	1.200	37.43	2.184	1.974
Imram and Pantazopoulou (1996)	1	54	115	21.17	0.22	0.26	8.4	55.2	2.96	2.320	54.89	3.455	2.969
Imram and Pantazopoulou (1996)	1	54	115	21.17	0.22	0.26	14.7	79.4	3.96	3.930*	78.083		
Imram and Pantazopoulou (1996)	1	54	115	21.17	0.22	0.26	21	102.6	5.05	5.340*	102.32	5.51	
Jamet et al. (1984)	1	110	220	31.43	0.369		3	45.13	0.697				
Jamet et al. (1984)	1	110	220	31.43	0.369		10	62.71	1.639				
Jamet et al. (1984)	1	110	220	31.43	0.369		25	99.82	3.875				
Jamet et al. (1984)	1	110	220	31.43	0.369		50	142.96	10.177				
Kotsovos and Newman (1978)	1	100	250	31.7			19	99.15	2.286	1.125	98.09	2.757	2.177
Kotsovos and Newman (1978)	1	100	250	31.7			24	112.92	3.737	2.286	112.92	3.737	2.286
Kotsovos and Newman (1978)	1	100	250	31.7			44	175.64	4.934	1.524	163.98	7.039*	3.991
Kotsovos and Newman (1978)	1	100	250	46.9			18	121.72	1.846	0.869	120.13	2.389	1.593
Kotsovos and Newman (1978)	1	100	250	46.9			35	177.65	2.679	1.195	169.70	3.403	2.787
Kotsovos and Newman (1978)	1	100	250	46.9			51	227.54	3.910	1.195	220.55	5.140	3.077
Kotsovos and Newman (1978)	1	100	250	46.9			70	271.40	5.032	1.774	253.60	7.385	7.095*
Kotsovos and Newman (1979)	1	100	250	73.3	0.2		35	217.85	1.927	0.477	205.71	3.012	1.845
Kotsovos and Newman (1979)	1	100	250	73.3	0.2		69.8	322.68	3.001	0.722	315.86	3.900	1.996
Newman (1979)	1	100	250	91.19	0.147		3.5	110.34	0.591	0.216	104.45	0.452	0.657
Newman (1979)	1	100	250	91.19	0.147		6.8	126.75	0.861	0.394	119.45	1.091	0.544
Newman (1979)	1	100	250	91.19	0.147		13.7	147.49	1.352	0.55	140.33	1.722	1.148
Newman (1979)	1	100	250	91.19	0.147		22.6	179.80	2.154*	0.708	167.72	3.052*	1.688
Newman (1979)	1	100	250	91.19	0.147		34.9	208.54	3.369*	1.062	202.41	4.633*	1.656
Newman (1979)	1	100	250	91.19	0.147		69.2	287.49	6.106*	1.666	271.33	11.818*	6.924
Newman (1979)	1	100	250	91.19	0.147		138.2	461.03	12.76*	2.22	452.70	18.760*	5.942
Newman (1979)	1	100	250	91.19	0.147		138.2	480.41	11.152*	2.596	472.35	14.108*	4.536
Newman (1979)	1	100	250	73.3	0.2		3.5	97.40	0.38	0.14	92.01	0.44	0.260
Newman (1979)	1	100	250	73.3	0.2		6.8	115.04	0.64	0.18	90.51	1.04	1.320
Newman (1979)	1	100	250	73.3	0.2		13.7	147.19	0.95	0.34	133.43	1.35	0.900
Newman (1979)	1	100	250	73.3	0.2		22.6	187.82	1.34	0.4	165.79	2.38	1.340
Newman (1979)	1	100	250	73.3	0.2		34.9	220.89	2	0.64	206.92	2.94	1.660
Newman (1979)	1	100	250	73.3	0.2		69.2	312.92	3.42	0.76	306.09	4.16	1.780

Paper	n	D (mm)	H (mm)	f'_{co} (MPa)	ε_{co} (%)	ε_{lo} (%)	f^*_l (MPa)	f^*_{cc} (MPa)	ε^*_{cc} (%)	ε^*_l (%)	$f_{c,res}$ (MPa)	$\varepsilon_{c,res}$ (%)	$\varepsilon_{l,res}$ (%)
Newman (1979)	1	100	250	73.3	0.2		69.2	325.96	2.95	0.88	322.08	3.33	1.380
Newman (1979)	1	100	250	73.3	0.2		138.2	483.65	4.82*	0.46	478.71	5.08*	0.520
Newman (1979)	1	100	250	73.3	0.2		138.2	491.62	4.9*	0.48	480.92	6.25*	2.520
Newman (1979)	1	100	250	23.23	0.173		3.5	38.56	1.441	0.864	36.67	1.635	1.050
Newman (1979)	1	100	250	23.23	0.173		6.8	52.17	2.082	1.194	50.48	2.528	2.236
Newman (1979)	1	100	250	23.23	0.173		13.7	77.09	3.754	1.948	73.77	6.124*	4.330
Newman (1979)	1	100	250	23.23	0.173		22.6	114.31	5.635	2.132	109.49	6.465*	3.672
Newman (1979)	1	100	250	23.23	0.173		34.9	152.91	6.372	2.314	149.82	7.224*	3.910
Newman (1979)	1	100	250	23.23	0.173		69.2	261.16	8.977*	5.176	257.13	9.347*	5.716
Newman (1979)	1	100	250	23.23	0.173		138.2	462.20	11.705*	5.652	453.58	14.089*	7.502
Lahlou et al. (1992)	2	52	104	46	0.27	0.1	7.6	84	0.94	0.44	80.3	1.48	0.99
Lahlou et al. (1992)	2	52	104	46	0.27	0.1	22	133	2.3	0.73	132.4	2.34*	0.73
Lahlou et al. (1992)	2	52	104	78	0.32	0.23	7.6	119	0.7	0.29	110.7*	1.03	0.99
Lahlou et al. (1992)	2	52	104	78	0.32	0.23	22	169	1.54	0.65	168.5	1.3*	0.55
Lahlou et al. (1992)	2	52	104	113	0.31	0.26	7.6	156	0.57	0.29	147.1*	0.73	0.74
Lahlou et al. (1992)	2	52	104	113	0.31	0.26	22	211	0.99	0.41	199.4	1.29*	0.83
Lu and Hsu (2007)	1	100	200	67	0.251	0.1	3.5	84.9	0.466	0.217	78.71	0.613	0.474
Lu and Hsu (2007)	1	100	200	67	0.251	0.1	7	99.0	0.776	0.361	78.53	1.864	1.516
Lu and Hsu (2007)	1	100	200	67	0.251	0.1	14	130.7	1.237	0.521	120.86	2.226	1.306
Lu and Hsu (2007)	1	100	200	67	0.251	0.1	14	132.7	1.250	0.531			
Lu and Hsu (2007)	1	100	200	67	0.251	0.1	14	134.9	1.350	0.531			
Lu and Hsu (2007)	1	100	200	67	0.251	0.1	14	135.5	1.370	0.531			
Lu and Hsu (2007)	1	100	200	67	0.251	0.1	21	154.0	1.661	0.574			
Lu and Hsu (2007)	1	100	200	67	0.251	0.1	21	157.1	1.830	0.717			
Lu and Hsu (2007)	1	100	200	67	0.251	0.1	21	161.2	1.940	0.717			
Lu and Hsu (2007)	1	100	200	67	0.251	0.1	28	180.2	2.501	0.868	165.76	4.490	2.230
Lu and Hsu (2007)	1	100	200	67	0.251	0.1	28	179.9	2.409	0.887			
Lu and Hsu (2007)	1	100	200	67	0.251	0.1	42	229.1	3.213	1.108	221.65	4.648	2.234
Lu and Hsu (2007)	1	100	200	67	0.251	0.1	56	276.0	4.058	1.238	267.95	5.775	2.366
Richart et al. (1928)	1	101.6	203.2	17.8			2.1	30.7	1.71*	1.02			
Richart et al. (1928)	1	101.6	203.2	17.8			1.2	24.8	2.96*	1.07			
Richart et al. (1928)	1	101.6	203.2	17.8			1.2	22.3	0.95	0.79			
Richart et al. (1928)	1	101.6	203.2	17.8			1.2	19.6					
Richart et al. (1928)	1	101.6	203.2	17.8			3.8	34.3	2.61*	0.80			
Richart et al. (1928)	1	101.6	203.2	17.8			3.8	38.7	1.94*	2.08*			
Richart et al. (1928)	1	101.6	203.2	17.8			3.8	35.8	2.35*	1.56			
Richart et al. (1928)	1	101.6	203.2	17.8			3.8	33.9	4.40*	2.05			
Richart et al. (1928)	1	101.6	203.2	17.8			6.1	46.8	1.7	0.82			
Richart et al. (1928)	1	101.6	203.2	17.8			5.4	48.9	3.64*	1.64			
Richart et al. (1928)	1	101.6	203.2	17.8			5.4	42.4	3.17*	1.14			
Richart et al. (1928)	1	101.6	203.2	17.8			5.4	41.9	4.38*	1.61			
Richart et al. (1928)	1	101.6	203.2	17.8			7.5	52.8	2.2	0.59			
Richart et al. (1928)	1	101.6	203.2	17.8			7.5	52.7	3.48*	1.62			
Richart et al. (1928)	1	101.6	203.2	17.8			7.5	50.7	6.10*	2.46			
Richart et al. (1928)	1	101.6	203.2	17.8			7.5	49.4	5.38*	2.33			
Richart et al. (1928)	1	101.6	203.2	17.8			10.4	63.5	4.37*	1.25			
Richart et al. (1928)	1	101.6	203.2	17.8			10.4	61.4	5.12*	1.82			
Richart et al. (1928)	1	101.6	203.2	17.8			10.4	39.4*					
Richart et al. (1928)	1	101.6	203.2	17.8			10.4	61.2	6.5*	2.05			
Richart et al. (1928)	1	101.6	203.2	17.8			13.9	79.3	4.97*	2.00			
Richart et al. (1928)	1	101.6	203.2	17.8			13.9	71.0	3.06	1.10			
Richart et al. (1928)	1	101.6	203.2	17.8			13.9	73.4	5.32*	1.90			
Richart et al. (1928)	1	101.6	203.2	17.8			13.9	72.7	6.11*	1.85			
Richart et al. (1928)	1	101.6	203.2	17.8			20.8	87.6					
Richart et al. (1928)	1	101.6	203.2	17.8			20.8	100.7	5.22	1.60			
Richart et al. (1928)	1	101.6	203.2	17.8			20.8	97.2	5.26	2.02			
Richart et al. (1928)	1	101.6	203.2	17.8			20.8	97.1	5.22	1.90			
Richart et al. (1928)	1	101.6	203.2	17.8			25.9	119.3	4.46	1.54			
Richart et al. (1928)	1	101.6	203.2	17.8			28.2	122.4	5.28	1.69			
Richart et al. (1928)	1	101.6	203.2	17.8			28.2	121.7					
Richart et al. (1928)	1	101.6	203.2	17.8			28.2	121.3	7.12	2.02			
Richart et al. (1928)	1	101.6	203.2	25.2			3.8	46.9	3.15*	1.92			
Richart et al. (1928)	1	101.6	203.2	25.2			3.8	47.0	3.16*	1.69			
Richart et al. (1928)	1	101.6	203.2	25.2			3.8	47.1	2.78*	1.59			
Richart et al. (1928)	1	101.6	203.2	25.2			3.8	45.7	3.16*	1.37			
Richart et al. (1928)	1	101.6	203.2	25.2			7.5	58.4	1.98	1.05			
Richart et al. (1928)	1	101.6	203.2	25.2			7.5	57.2	2.77*	0.68			
Richart et al. (1928)	1	101.6	203.2	25.2			7.5	60.2	2.97*	1.23			
Richart et al. (1928)	1	101.6	203.2	25.2			7.5	62.0	5.97*	1.95			
Richart et al. (1928)	1	101.6	203.2	25.2			13.9	83.7	2.96	1.02			
Richart et al. (1928)	1	101.6	203.2	25.2			13.9	87.9	3.18	1.46			
Richart et al. (1928)	1	101.6	203.2	25.2			13.9	81.5	5.68*	1.85			
Richart et al. (1928)	1	101.6	203.2	25.2			13.9	82.0	4.75*	1.80			
Richart et al. (1928)	1	101.6	203.2	25.2			28.2	133.1					
Richart et al. (1928)	1	101.6	203.2	25.2			28.2	135.1	4.39	1.59			
Richart et al. (1928)	1	101.6	203.2	25.2			28.2	131.0	6.68	1.95			
Richart et al. (1928)	1	101.6	203.2	25.2			28.2	129.3	6.14	1.72			
Richart et al. (1928)	1	101.6	203.2	7.2			3.8	20.0					
Richart et al. (1928)	1	101.6	203.2	7.2			3.8	29.2	5.56*	2.30			
Richart et al. (1928)	1	101.6	203.2	7.2			3.8	27.4					
Richart et al. (1928)	1	101.6	203.2	7.2			3.8	26.5	6.20*	2.25			
Richart et al. (1928)	1	101.6	203.2	7.2			7.5	43.4	6.52*	1.41			
Richart et al. (1928)	1	101.6	203.2	7.2			7.5	43.6	3.56	1.64			
Richart et al. (1928)	1	101.6	203.2	7.2			7.5	43.4	6.58*	1.72			
Richart et al. (1928)	1	101.6	203.2	7.2			7.5	42.2	5.58*	1.23			

Paper	n	D (mm)	H (mm)	f'_{co} (MPa)	ε_{co} (%)	ε_{lo} (%)	f^*_l (MPa)	f^*_{cc} (MPa)	ε^*_{cc} (%)	ε^*_l (%)	$f_{c,res}$ (MPa)	$\varepsilon_{c,res}$ (%)	$\varepsilon_{l,res}$ (%)
Richart et al. (1928)	1	101.6	203.2	7.2			13.9	70.2	5.34*	1.98			
Richart et al. (1928)	1	101.6	203.2	7.2			13.9	69.3	5.94*	1.95			
Richart et al. (1928)	1	101.6	203.2	7.2			13.9	51.7					
Richart et al. (1928)	1	101.6	203.2	7.2			13.9	71.0					
Richart et al. (1928)	1	101.6	203.2	7.2			28.2	118.9					
Richart et al. (1928)	1	101.6	203.2	7.2			28.2	118.2	5.36*	2.02			
Richart et al. (1928)	1	101.6	203.2	7.2			28.2	123.1	6.96*	1.95			
Richart et al. (1928)	1	101.6	203.2	7.2			28.2	120.7					
Richart et al. (1928)	1	101.6	203.2	7.2			45.2	169.6	7.80*	2.00			
Rutland and Wang (1997)	1	50	100	39.4			1.7	56.6					
Rutland and Wang (1997)	1	50	100	39.4			1.7	61.9					
Rutland and Wang (1997)	1	50	100	39.4			3.5	56.6					
Rutland and Wang (1997)	1	50	100	39.4			3.5	60.2					
Rutland and Wang (1997)	1	50	100	39.4			3.5	78.3					
Rutland and Wang (1997)	1	50	100	39.4			3.5	81.0					
Rutland and Wang (1997)	1	50	100	39.4			3.5	83.6					
Rutland and Wang (1997)	1	50	100	39.4			7	73.9					
Rutland and Wang (1997)	1	50	100	39.4			7	95.6					
Rutland and Wang (1997)	1	50	100	39.4			7	98.2					
Rutland and Wang (1997)	1	50	100	39.4			14	119.0					
Rutland and Wang (1997)	1	50	100	39.4			14	120.8					
Rutland and Wang (1997)	1	50	100	39.4			14	131.0					
Rutland and Wang (1997)	1	50	100	39.4			28	141.6					
Rutland and Wang (1997)	1	50	100	39.4			28	161.5					
Rutland and Wang (1997)	1	50	100	39.4			28	167.3					
Rutland and Wang (1997)	1	50	100	39.4			28	188.1					
Rutland and Wang (1997)	1	50	100	39.4			42	206.6					
Rutland and Wang (1997)	1	50	100	39.4			42	211.1					
Rutland and Wang (1997)	1	50	100	39.4			42	213.7					
Rutland and Wang (1997)	1	50	100	39.4			42	219.5					
Rutland and Wang (1997)	1	50	100	39.4			56	248.7					
Rutland and Wang (1997)	1	50	100	39.4			56	267.7					
Rutland and Wang (1997)	1	50	100	39.4			1.7	59.7					
Rutland and Wang (1997)	1	50	100	39.4			3.5	74.3					
Rutland and Wang (1997)	1	50	100	39.4			3.5	77.0					
Rutland and Wang (1997)	1	50	100	39.4			3.5	61.9					
Rutland and Wang (1997)	1	50	100	39.4			3.5	70.8					
Rutland and Wang (1997)	1	50	100	39.4			7	79.6					
Rutland and Wang (1997)	1	50	100	39.4			7	96.9					
Rutland and Wang (1997)	1	50	100	39.4			14	61.1*					
Rutland and Wang (1997)	1	50	100	39.4			14	106.2					
Rutland and Wang (1997)	1	50	100	39.4			14	110.6					
Rutland and Wang (1997)	1	50	100	39.4			14	115.0					
Rutland and Wang (1997)	1	50	100	39.4			14	101.8					
Rutland and Wang (1997)	1	50	100	39.4			28	131.0					
Rutland and Wang (1997)	1	50	100	39.4			28	158.0					
Rutland and Wang (1997)	1	50	100	39.4			42	203.5					
Rutland and Wang (1997)	1	50	100	39.4			56	259.3					
Rutland and Wang (1997)	1	50	100	39.4			1.7	61.1					
Rutland and Wang (1997)	1	50	100	39.4			1.7	65.5					
Rutland and Wang (1997)	1	50	100	39.4			3.5	71.7					
Rutland and Wang (1997)	1	50	100	39.4			3.5	77.9					
Rutland and Wang (1997)	1	50	100	39.4			7	86.3					
Rutland and Wang (1997)	1	50	100	39.4			7	82.7					
Rutland and Wang (1997)	1	50	100	39.4			14	109.3					
Rutland and Wang (1997)	1	50	100	39.4			42	167.3					
Rutland and Wang (1997)	1	50	100	39.4			42	150.0					
Setunge et al. (1993)	1	100	200	108			5	144					
Setunge et al. (1993)	1	100	200	108			10	172					
Setunge et al. (1993)	1	100	200	108			15	194					
Setunge et al. (1993)	1	100	200	102			5	145					
Setunge et al. (1993)	1	100	200	102			10	158					
Setunge et al. (1993)	1	100	200	102			15	175					
Setunge et al. (1993)	1	100	200	96			5	125					
Setunge et al. (1993)	1	100	200	96			10	147					
Setunge et al. (1993)	1	100	200	96			15	163					
Setunge et al. (1993)	1	100	200	96			5	117					
Setunge et al. (1993)	1	100	200	96			10	144					
Setunge et al. (1993)	1	100	200	96			15	151					
Sfer et al. (2002)	1	150	300	35.8	0.2		1.5	45.5	0.26	0.11	33.7	0.50	0.44
Sfer et al. (2002)	1	150	300	35.8	0.2		1.5	47.8	0.34	0.09	30.1	1.18	2.44
Sfer et al. (2002)	1	150	300	35.8	0.2		4.5	55.3	0.41	0.19	38.8	1.44	2.02
Sfer et al. (2002)	1	150	300	35.8	0.2		4.5	58.2	0.52	0.14	41.9	1.94	2.02
Sfer et al. (2002)	1	150	300	35.8	0.2		9	65.7	0.83	0.23	57.8	2.27	1.21
Sfer et al. (2002)	1	150	300	35.8	0.2		9	66.5	0.63	0.25	57.2	2.34	2.56
Sfer et al. (2002)	1	150	300	35.8	0.2		30	124.5	7.00*	3.23	120.8	8.17*	3.98
Sfer et al. (2002)	1	150	300	35.8	0.2		30	129.3	10.90*		127.5	9.85*	
Sfer et al. (2002)	1	150	300	35.8	0.2		60	192.9	8.50	3.23	192.6	7.33	
Sfer et al. (2002)	1	150	300	35.8	0.2		60	205.1	8.30		202.9	8.75	
Smith et al. (1989)	1	54	108	22.1	0.339		0.69	28.08	0.531	0.182	13.68	3.953*	4.074
Smith et al. (1989)	1	54	108	22.1	0.339		3.45	36.11	2.085*	0.842	32.70	2.783	1.306
Smith et al. (1989)	1	54	108	22.1	0.339		13.79	85.44	2.864*	0.318	85.41	2.864*	0.318
Smith et al. (1989)	1	54	108	34.5	0.351		0.69	41.73	0.397	0.164	16.38	2.375*	3.064
Smith et al. (1989)	1	54	108	34.5	0.351		3.45	57.81	0.838	0.532	39.70	2.651	3.576
Smith et al. (1989)	1	54	108	34.5	0.351		6.89	78.21	1.158	0.788	56.05	2.698	3.578

Paper	n	D (mm)	H (mm)	f'_{co} (MPa)	ε_{co} (%)	ε_{lo} (%)	f^*_l (MPa)	f^*_{cc} (MPa)	ε^*_{cc} (%)	ε^*_l (%)	$f_{c,res}$ (MPa)	$\varepsilon_{c,res}$ (%)	$\varepsilon_{l,res}$ (%)
Smith et al. (1989)	1	54	108	34.5	0.351		13.79	107.58	2.234	1.110	90.51	3.548	3.256
Smith et al. (1989)	1	54	108	34.5	0.351		20.70	130.15	2.952	1.620	123.75	3.431*	2.582
Smith et al. (1989)	1	54	108	34.5	0.351		27.58	159.52	3.306	1.778	152.32	3.306*	1.778
Smith et al. (1989)	1	54	108	34.5	0.351		34.47	170.03	3.128*	0.870	166.30	3.128*	0.870
Smith et al. (1989)	1	54	108	44.1	0.354		0.69	57.39	0.338	0.436	24.20	1.284*	2.394
Smith et al. (1989)	1	54	108	44.1	0.354		3.45	88.04	0.616	0.714	54.59	1.634	2.756
Smith et al. (1989)	1	54	108	44.1	0.354		6.89	113.93	0.811	0.968	96.13	1.365*	2.542
Smith et al. (1989)	1	54	108	44.1	0.354		13.79	131.45	1.153	0.774	126.11	1.171*	0.804
Smith et al. (1989)	1	54	108	44.1	0.354		27.58	167.87	1.078*	0.400	165.94	1.078*	0.400
Smith et al. (1989)	1	54	108	44.1	0.354		34.47	167.87	1.078*	0.400	165.94	1.078*	0.400
Tan and Sun (2004)	1	100	300	51.8	0.24		1.9	64.8	0.33				
Tan and Sun (2004)	1	100	300	51.8	0.24		1.9	66.0	0.39				
Tan and Sun (2004)	1	100	300	51.8	0.24		7.5	86.6	0.46				
Tan and Sun (2004)	1	100	300	51.8	0.28		7.5	84.2	0.49*				
Tan and Sun (2004)	1	100	300	51.8	0.24		12.5	99.3	0.49*				
Tan and Sun (2004)	1	100	300	51.8	0.24		12.5	103.3	0.66*				
Vu et al. (2009)	1	70	140	41.15			50	174.90	2.544*	0.466	154.354	7.568*	3.366
Vu et al. (2009)	1	70	140	41.15			100	248.97	5.419*	0.908	246.927	5.675*	1.126
Vu et al. (2009)	1	70	140	41.15			200	446.50	8.498*	1.386	428.704	8.498*	1.384
Vu et al. (2009)	1	70	140	41.15			400	779.84	11.890*		779.835	11.890*	
Vu et al. (2009)	1	70	140	41.15			650	868.31	7.592*	2.486	868.171	7.592*	2.486
Xie et al. (1995)	1	55.5	110	60.2	0.37		0.84	58.39*	0.70		29.08	3.00*	
Xie et al. (1995)	1	55.5	110	60.2	0.37		2.29	80.61	0.53		42.32	2.54*	
Xie et al. (1995)	1	55.5	110	60.2	0.37		5.30	97.58	0.75		58.82	2.96*	
Xie et al. (1995)	1	55.5	110	60.2	0.37		8.31	107.64	0.98		78.20	2.94	
Xie et al. (1995)	1	55.5	110	60.2	0.37		11.32	121.60	1.08		95.42	3.43	
Xie et al. (1995)	1	55.5	110	60.2	0.37		14.33	136.83	1.38		111.91	3.13	
Xie et al. (1995)	1	55.5	110	60.2	0.37		20.29	156.88	2.12		141.11	3.24	
Xie et al. (1995)	1	55.5	110	60.2	0.37		23.30	172.05	2.08		153.51	3.18*	
Xie et al. (1995)	1	55.5	110	60.2	0.37		29.32	193.24	2.37		177.59	3.22*	
Xie et al. (1995)	1	55.5	110	92.21	0.37		3.78	129.36	0.62		60.58	3.45*	
Xie et al. (1995)	1	55.5	110	92.21	0.37		8.30	155.63	0.80		85.93	3.90*	
Xie et al. (1995)	1	55.5	110	92.21	0.37		12.82	181.17	1.06		111.10	3.80*	
Xie et al. (1995)	1	55.5	110	92.21	0.37		16.5	199.80	1.17		137.01	3.77	
Xie et al. (1995)	1	55.5	110	92.21	0.37		17.33	194.27	1.16		150.01	3.71	
Xie et al. (1995)	1	55.5	110	92.21	0.37		21.85	208.74	1.31		167.99	3.95	
Xie et al. (1995)	1	55.5	110	92.21	0.37		26.28	234.65	1.55		187.81	4.19	
Xie et al. (1995)	1	55.5	110	92.21	0.37		35.5	261.11	2.42		225.89	4.03	
Xie et al. (1995)	1	55.5	110	92.21	0.37		44.44	293.47	2.49		262.77	4.10	
Xie et al. (1995)	1	55.5	110	119	0.37		6.07	172.31	0.67		74.97	3.93*	
Xie et al. (1995)	1	55.5	110	119	0.37		12.02	212.18	0.79		113.76	4.02*	
Xie et al. (1995)	1	55.5	110	119	0.37		17.97	225.86	1.02		143.16	3.98*	
Xie et al. (1995)	1	55.5	110	119	0.37		24.04	250.97	1.13		173.26	4.28*	
Xie et al. (1995)	1	55.5	110	119	0.37		29.99	261.80	1.32		195.76	4.29	
Xie et al. (1995)	1	55.5	110	119	0.37		36.06	280.96	1.43		228.84	4.59	
Xie et al. (1995)	1	55.5	110	119	0.37		47.96	316.30	1.61		285.84	3.93	
Xie et al. (1995)	1	55.5	110	119	0.37		59.98	367.35	2.44		330.82	4.58	

* denotes inconsistent data when compared with overall trend in the database (data excluded from the calibration of the proposed model)